UNIVERSIDADE FEDERAL DE MINAS GERAIS

Curso de Pós-Graduação em Engenharia Metalúrgica e de Minas

Tese de Doutorado

POLIURETANAS BIODEGRADÁVEIS E NANOCOMPÓSITOS DE ARGILOMINERAIS COM EFEITO MEMÓRIA DE FORMA

BIODEGRADABLE POLYURETHANE AND MONTMORILLONITE NANOCOMPOSITES WITH SHAPE MEMORY

Autora: Iaci Miranda Pereira

Orientador: Prof. Rodrigo Lambert Oréfice

Agosto de 2009

UNIVERSIDADE FEDERAL DE MINAS GERAIS
Curso de Pós-Graduação em Engenharia Metalúrgica e de Minas

Iaci Miranda Pereira

POLIURETANAS BIODEGRADÁVEIS E NANOCOMPÓSITOS DE ARGILOMINERAIS COM EFEITO MEMÓRIA DE FORMA

BIODEGRADABLE POLYURETHANE AND MONTMORILLONITE NANOCOMPOSITES WITH SHAPE MEMORY

Tese de doutorado apresentada ao Curso de Pós-Graduação em Engenharia Metalúrgica e de Minas da Universidade Federal de Minas Gerais.

Área de concentração: Ciência e Engenharia de Materiais
Orientador: Prof. Rodrigo Lambert Oréfice

Belo Horizonte
Escola de Engenharia da UFMG
Agosto de 2009

Agradecimentos

Sem dúvida alguma, não houve parte mais complexa do que esta, neste trabalho. Fazer uma lista de agradecimentos foi muito difícil, porque foram muitos amigos, deste e de outros “mundos”, que garantiram que eu completasse esta tese, que tornaram a essa tarefa um prazer e uma alegria. Seria um “crime” esquecer o nome de algum deles. Pensei várias vezes em omitir este capítulo; entretanto, há nomes que não podem ser omitidos.

Meu muitíssimo obrigado:

Ao professor Rodrigo Lambert Oréfice.

Aos meus colegas do Laboratório de Polímeros e Compósitos: Agda, Eliane, Lívio, Magda, Patrícia, Sandhra, Tibúrcio, Viviane e a todos os outros.

Aos professores da Engenharia Metalúrgica da UFMG.

Aos funcionários: Andréia, Cláudia, Cida, Nelson, Patrícia (sem vírgula) e todos os outros.

A Deus.

E sem dúvida alguma a Maria da Graça e a sua equipe.

Espero poder retribuir algum dia.

Sumário

Lista de Figuras X
Lista de Tabelas XV
Resumo XVII
Abstract XVIII

Capítulo I

I – Introdução e objetivos do trabalho 1
I.1 – Polímeros com Memória de Forma 2
A – Variação do Módulo de Elasticidade 3
B – Variação da Entropia Configuracional 5
I.2 – Poliuretanas com Memória de Forma 6
I.3 – Variáveis que Influenciam as Propriedades das Poliuretanas segmentadas 8
A – Separação de Fase 9
B – Segmento Rígido 9
C – Segmento Macio 10
I.4 – Objetivos e Organização da Tese 10
I.5 – Referências Bibliográficas 13

Capítulo II

II – Study of the morphology exhibited by linear segmented polyurethanes 17
II.1 – Introduction 18
II.2 – Materials and Methods 18
A – Polymer synthesis 18
B – Infrared spectroscopy 19
C – Modulated differential scanning calorimetry (MDSC) 19
D – Synchrotron small angle X-ray scattering (SAXS) 20
II.3 – Results and discussion 21
II.4 – Conclusions 30
II.5 – Acknowledgments 30
II.6 – References 31

Capítulo III

III – Proliferation of human mesenchymal stem cells derived from adipose tissue on polyurethanes with tunable biodegradability 32
III.1 – Introduction 33
III.2 – Materials and Methods 34
A – Prepolymer synthesis 34
B – Hydrolytic degradation tests 35
C – Infrared spectroscopy (FTIR) 36
D – Wide angle X-ray scattering (WAXS) 36
E – Scanning electron microscopy (SEM) 36
F – Cell origin, isolation, and culturing of adipose tissue-derived stem cell 37
G – Cellular Viability 37
H – Alkaline phosphatase activity 38
I – Collagen secretion measurement 38
III.3 – Results and Discussion 38
A – Hydrolytic and alkaline degradation tests 38
B – Infrared spectroscopy (FTIR) 39
C – Wide angle X-ray scattering (WAXS) 43
D – Scanning electron microscopy (SEM) 46
E – Cellular Viability 47
III.4 – Conclusion 48
III.5 – Acknowledgements 48
III.6 – References 48

Capítulo IV

IV – Effect of degree of clay delamination on the phase morphology, surface chemical aspects and properties of hydrolysable polyurethane for periodontal regeneration 52
IV.1 – Introduction 53
IV.2 – Materials and Methods 55
A – Polymer synthesis 55
B – Nanocomposites 55

C – Characterization 56
D – Cell culture and viability assays 58
IV.3 – Results and Discussion 59
A – Infrared Spectroscopy 59
B – Wide angle X-ray scattering (WAXS) 63
C – Small angle X-ray scattering (SAXS) 65
D – Mechanical Properties 66
E – Polymer Swelling 68
F – Alkaline degradation tests 69
G – Cellular Viability 70
IV.4 – Conclusion 70
IV.5 – Acknowledgements 71
IV.6 – References 71

Capítulo V

V – Study of the morphology exhibited by linear segmented polyurethane during shape memory cycles 74
V.1 – Introduction 75
V.2 – Materials and Methods 75
A – Polymer synthesis 75
B – Infrared spectroscopy 76
C – Synchrotron small angle X-ray scattering (SAXS) 76
D – Mechanical Properties and Shape memory properties (SM) 77
E – In situ recovery 79
V.3 – Results and discussion 79
V.4 – Conclusions 84
V.5 – Acknowledgments 84
V.6 – References 85

Capítulo VI

VI – The morphology and phase mixing studies on poly(ester urethane) during a low temperature shape memory cycle 86

VI.1 – Introduction 87
VI.2 – Materials and Methods 88
A – Prepolymer synthesis 88
B – Modulated differential scanning calorimetry (MDSC) 88
C – Dynamic Mechanical Analysis – DMA 89
D – Synchrotron small angle X-ray scattering (SAXS) 89
E – Mechanical Properties 89
F – Shape memory properties (SM) 90
VI.3 – Results and discussion 91
VI.4 – Conclusions 97
VI.5 – Acknowledgments 98
VI.6 – References 98

Capítulo VII

VII – The morphology and phase mixing studies on poly(ester urethane) during shape memory cycle 100
VII.1 – Introduction 101
VII.2 – Materials and Methods 102
A – Materials 102
B – Prepolymer synthesis 102
C – Neutralization of the prepolymer 102
D – Dispersion and chain extension 102
E – Film formation 103
F – Infrared spectroscopy 103
G – Wide angle X-ray scattering (WAXS) 103
H – Thermal Analysis 104
I – Mechanical Properties 104
J – Shape memory properties (SM) 104
K – Synchrotron small angle X-ray scattering (SAXS) 106
VII.3 – Results and discussion 107
A – Thermal Analysis 107
B – Infrared spectroscopy 109

C – Wide angle X-ray scattering (WAXS) 112
D – Synchrotron small angle X-ray scattering (SAXS) 113
E – Mechanical Properties 122
VII.4 – Conclusions 124
VII.5 – Acknowledgments 124
VII.6 – References 124

Capítulo VIII

VIII – Study of the morphology exhibited by exfoliated polyurethane / montmorillonite nanocomposites during shape memory cycle 129
VIII.1 – Introduction 129
VIII.2 – Materials and Methods 130
A – Polymer synthesis 130
B – Modulated differential scanning calorimetry (MDSC) 130
C – Synchrotron small angle X-ray scattering (SAXS) 131
D – Shape memory properties (SM) 131
VIII.3 – Results and discussion 133
VIII.4 – Conclusions 140
VIII.5 – Acknowledgments 140
VIII.6 – References 140

Capítulo IX

IX – Shape-memory anchoring system for bladder sensors 143
IX.1 – Introduction 143
IX.2 – Materials and Methods 144
A – Sensor Design 144
B – Polymer synthesis 145
C – Laser machine 146
D – Infrared spectroscopy 146
E – Mechanical Tests 146
F – Shape memory properties (SM) 147
G – Shape Recovery Body Simulation 149

H – Hydrolytic degradation tests 149
IX.3 – Results and Discussion 150
IX.4 – Conclusion 154
IX.5 – Acknowledgements 155
IX.6 – References 155

Capítulo X

X – Conclusões Finais 156

Lista de Figuras

Figure I.1 Variação do módulo de elasticidade com a temperatura [3]..... 3

Figure I.2 Representação do efeito de memória de forma para polímeros..... 4

Figure I.3 Exemplo de um poliuretano segmento, sintetizado de poliglicol. 7

Figure I.4 Representação das ligações cruzadas do segmento rígido: (a) interações de hidrogênio, (b) dipolo-dipolo, (c) dipolo-dipolo induzido..... 10

Figura I.5 Representação das áreas abrangidas durante o trabalho de tese. 11

Figure II.1 FTIR spectra of PU530, PU1250, PU2000, PU10000&530 and PU10000 samples..... 21

Figure II.2 Illustration of the deconvolution procedure of PU2000: (a) primary amine stretching, (b) carbonyl group stretching and (c) ether stretching. 23

Figure II.3 (a) Influence of hard segment content on degree of phase mixture and (b) number of hydrogen bonded NH groups. 25

Figure II.4 (a) Influence of hard segment content on degree of phase mixture and (b) influence of the hard segment on glass transition..... 25

Figure II.5 SAXS pattern of: (a)PU530, (b)PU1250, (c)PU2000, (d)PU10000&530 and (e)PU10000. 26

Figure II.6 (a) SAXS curves of obtained PUs and (b) Deconvoluted Lorentz SAXS pattern of samples. 27

Figure II.7 Deconvoluted Lorentz SAXS patterns: (a) PU1250, (b) PU2000, (c) PU10000&530 and (d) PU10000..... 28

Figure II.8 Correlation between SAXS and FTIR results..... 29

Figure II.9 Influence of hard segment content and $HBI_{(C=O)}^{(\%)}$ on the multiphase structure of polyurethane. 30

Figure III.1 Mass changes of polyurethanes upon degradation in: (a) PBS solution and (b) NaOH solution..... 39

Figure III.2 FTIR spectra of PU–A, PU–B and PU–C. 40

Figure III.3 FTIR spectra of PU-B after hydrolysis performed at 37ºC in PBS for 62 and 97 days. 41

Figure III.4 Band area development of PU-B during hydrolysis performed at 37ºC in PBS (a) PU-B, (b) after 62 days degradation and (c) after 97 days..... 42

Figure III.5 HBI(%) of obtained PUs and degraded samples. 43

Figure III.6 WAXS pattern of PU-A, PU-B and PU-C. 43

Figure III.7 WAXS spectra of obtained PUs after 62 days hydrolysis performed at 37ºC in PBS. 44

Figure III.8 Peak deconvolution of the WAXS profiles: (a) PU-A, (b) PU-B and PU-C; after 62 days hydrolysis performed at 37ºC. 45

Figure III.9 WAXS curves of PU-B and PU-C after 97 days hydrolysis performed at 37ºC in PBS. 46

Figure III.10 SEM images of PU-B sample degraded in PBS solution at 37ºC: (a) surface morphology after 62 days, (b) fracture surface after 62 days, (c) surface morphology after 97 days and (d) fracture surface after 97 days. 47

Figure III.11 (a) Cellular viability evaluated by MTT assay, collagen secretion by SIRCOL assay and alkaline phosphatase production evaluated by NBT-BCIP assay. Results evaluated after 3 days of incubation. Results represent Mean ± SD of triplicates from 3 separate experiments ($P < 0.05$). (*) indicates that there is a significant difference. (b) Photomicrographs of hMSCs (150X) in contact with PU´s 48

Figure IV.1 FTIR spectra of PU/MMT-1 to PU/MMT-5 samples. 59

Figure IV.2 Influence of filler content on band area of PU/MMT-1 to PU/MMT-5: (a) bands 4 and 6 to 8, (b) bands 1 and 3. 61

Figure IV.3 Hydrogen bonding interaction between PU and MMT layer. 61

Figure IV.4 Deconvoluted FTIR spectrum: (a) N–H stretching region, (b) carbonyl stretching region. 62

Figure IV.5 Influence of filler content on: (a) ratio of hydrogen bonding NH groups and HBI(%) and (b) phase mixture. 63

Figure IV.6 WAXS pattern of PU/MMT-1 to PU/MMT-5. 64

Figure IV.7 SAXS pattern of: (a) PU/MMT-1, (b) PU/MMT-2 and (c) PU/MMT-3. 65

Figure IV.8 (a) SAXS profiles of PU/MMT-1, PU/MMT-2 and PU/MMT-3 and (b) Lorentz correction. 66

Figure IV.9 Stress–strain curve of PU/MMT-1 to PU/MMT-5. 67

Figure IV.10 Influence of MMT content on σm and work hardening 67

Figure IV.11 Influence of MMT content on resilience. 68

Figure IV.12 Water uptake of PU/MMT-1 to PU/MMT-5. 69

Figure IV.13 Alkaline degradation of PU/MMT-1 to PU/MMT-5. 70

Figure IV.14 Results from the MTT assay for PU/MMT-1 to PU/MMT-5. The percentage of cell viability of all samples was calculated versus the control medium. 70

Figure V.1 Shape memory cycle steps 78

Figure V.2 (a) FTIR curve and (b) Stress X strain curve. 79

Figure V.3 SAXS pattern of: (a) undeformed specimen, (b) deformed specimen, (c-m) *in situ* recovery: 7.2 min to 18.4 min, (n) Cycle-A, (o) Cycle-B, (p) Cycle-C, (q) Cycle-E. 81

Figure V.4 (a) SAXS curves of obtained and (b) Deconvoluted Lorentz SAXS pattern 82

Figure V.5 Deconvoluted Lorentz SAXS pattern: (a) deformed specimen, (b) in situ recovery, (c) Cycle-A, (d) Cycle-B, (e) Cycle-C, (f) Cycle-E. 82

Figure V.6 (a) PU multi-phase evolution during in situ tests; (b) PU multi-phase during SM cycle. 84

Figure VI.1 Shape memory cycle steps. 90

Figure VI.2 DSC curves of the obtained PUs: (a) first heating (b) first cooling and (c) influence of W(HS) (%) on glass transition temperature. 92

Figure VI.3 (a) Storage modulus and (b) tanδ of PUs..... 93

Figure VI.4 SAXS pattern of: (a) permanent shape, (b) Step-3, (c) Step-4. 94

Figure VI.5 Deconvoluted Lorentz SAXS pattern of PU-A and PU-B: (a) permanent shape, (b) Step-3, and (c) Step-4..... 95

Figure VII.1 DSC curves for obtained PUs: (a) cooling and (b) heating 107

Figure VII.2 FTIR spectra of PU-I, PU-II and PU-III. 110

Figure VII.3 Deconvoluted FTIR spectrum, N–H stretching region, of samples: (a) PU-I, (b) PU-II and (c) PU-III. 110

Figure VII.4 WAXS pattern of obtained poly(ester-urethane) and PCL10000. 112

Figure VII.5 Experimental WAXS curves and its separation in amorphous and crystalline parts: (a) PCL10000, (b) PU-II and (c) PU-III..... 113

Figure VII.6 Small angle X-ray scattering patterns of PU-I, PU-II and PU-III during three stages: (a) Permanent Shape, (b) Step 3 and (c) Step 4. 114

Figure VII.7 SAXS curves for poly(ester-urethane) samples during different stages of shape memory cycle (a) Permanent Shape, (b) Step 3 and (c) Step 4. . 115

Figure VII.8 Deconvoluted Lorentz SAXS pattern of samples: (a) PU-II, and (b) PU-III. 116

Figure VII.9 PU-II and PU-III obtained three-phase structure during shape memory cycle. 117

Figure VII.10 Inter-domain repeat distance and lamellar crystalline repeat distance of PU-II and PU-III during shape memory cycle. 118

Figure VII.11 SAXS experimental data and tangents of PU-I experimental curve..... 121

Figure VII.12 Stress–strain curve of PU-I, PU-II and PU-III. 122

Figure VIII.1 Shape memory cycle steps 132

Figure VIII.2 DSC curves of the obtained PUs: (a) first heating (b) first cooling and (c) second heating..... 133

Figure VIII.3 SAXS pattern during different stages of shape-memory cycle of: (a) PU-C, (b) MMT-1, (c) MMT-2 and (d) MMT-3..... 135

Figure VIII.4 SAXS curves of obtained PUs: (a) PU-C, (b) MMT-1, (c) MMT-2 and (d) MMT-3..... 136

Figure VIII.5 Deconvoluted Lorentz SAXS pattern of permanent shape , Step-3, and Step-4: (a) PU-C, (b) MMT-1, and (c) MMT-2..... 137

Figure VIII.6 Step-3 disperse phase influence on shape memory properties 139

Figure IX.1 Sensor production scheme 144

Figure IX.2 Anchor system draft (thickness = 0.4mm)..... 146

Figure IX.3 (a) Tensile specimen (sample thickness 0.4 mm) and (b) Peel specimen 147

Figure IX.4 Shape memory thermomechanical cycle 148

Figure IX.5 Shape memory recovery in vivo simulation. 149

Figure IX.6 FTIR spectra of obtained PU 150

Figure IX.7 Pictures from the sensor manufacturing process: (a) PU film, (b) ensemble, (c) the pill after encapsulation by injection molding and (d) the simulated sensor..... 151

Figure IX.8 Mechanical test and peel test of obtained specimens. 152

Figure IX.9 Shape recovery body simulation pictures. 153

Figure IX.10 (a) Stress-strain curve of untreated specimen and degraded samples; (b) mechanical properties comparasion. 153

Figure IX.11 Mass changes of polyurethanes upon degradation. 154

Lista de Tabelas

Table II.1 Composition (wt.%) of waterborne PUs 19

Table II.2 FTIR results of as-molded poly(ester–urethanes) 24

Table II.3 DSC results of obtained poly(ester urethane). 26

Table II.4 Deconvoluted SAXS results of crystalline phase, hard domains and matrix. 29

Table III.1 Composition (wt.%) of waterborne PUs 35

Table III.2 Crystallinity index after hydrolysis performed at 37ºC in PBS. 46

Table IV.1 Relationship between FTIR absorption bands and functional group of observed in Figure 1. 60

Table IV.2 Mechanical properties of PU/MMT-1 to PU/MMT-5: 67

Table V.1 Thermo-cycle 77

Table VI.1 Composition (wt. %) of waterborne PUs 88

Table VI.2 DSC results of obtained poly(ester urethane). 92

Table VI.3 Deconvoluted SAXS results 95

Table VI.4 Mechanical and shape memory properties of PU-A, PU-B and PU-C... 95

Table VII.1 Composition (wt. %) of waterborne PUs. 103

Table VII.2 DSC results of obtained poly(ester urethane). 107

Table VII.3 Origin, the group frequency, and the functional group of spectral bands observed in Figure VII.2. 109

Table VII.4 – Deconvoluted SAXS results of crystalline phase, hard domains and the amorphous matrix as fraction of the total Qinv. 117

Table VII.5 SAXS experimental data: Qinv, LCrystal, Ldomain, and r. 122

Table VII.6 Mechanical and shape memory properties of PU-I, PU-II and PU-III. 123

Table VIII.1 Test set-ups 132

Table VIII.2 DSC results of obtained poly(ester urethane). 133

Table VIII.3 Deconvoluted SAXS results. 138

Table VIII.4 Shape memory properties of PU-C, MMT-1, MMT-2 and MMT-3 139

Resumo

Nos últimos anos, houve um aumento no interesse pelo uso de poliuretanas (PU) para aplicações biomédicas; especialmente para a classe das PUs com memória de forma. Durante esta tese, seis séries de PUs segmentadas com diferentes concentrações de segmento rígido foram preparadas pelo método pré-polimero em um ambiente aquoso. Nanocompósitos poliuretana/montmorilonita com diferentes concentrações de argilas também foram produzidos. PUs e os nanocompósitos tiveram sua estrutura química, morfologia, propriedades mecânicas e memória de forma investigadas. Também foram estudadas a degradação hidrolítica e alcalina além da viabilidade e proliferação celular. As técnicas aplicadas demonstraram que a concentração de segmento rígido e as interações de hidrogênio foram os dois fatores determinantes para estabelecer a morfologia das PUs segmentadas obtidas. Resultados mostraram que o grau de delaminação da argila interfere na morfologia das fases. Os polímeros e os nanocompósitos obtidos apresentaram memória de forma. As mudanças morfológicas durante ciclos de memória de forma foram investigadas. O processo de recuperação da forma permanente foi dividido em três fases. O ciclo de deformação conduziu à formação de uma nanoestrutura orientada derivada do alinhamento das cadeias. A elevação da incompatibilidade no *bulk* e a recuperação entrópica foram as duas características principais para determinar a morfologia final das PUs. A recuperação da forma também foi ativada pelas interações de hidrogênio entre os domínios rígidos. Uma relação entre a habilidade do PU de recuperar a forma original e a nanoestrutura original foi determinada. Tendo em vista que a incorporação de partículas perturba a formação de interações de hidrogênio entre os grupos amina e carbonila interferindo com a mobilidade das cadeias polímericas e com a formação, durante a deformação, da estrutura semi-estável, a recuperação de forma foi reduzida pela presença de nanopartículas. As PUs obtidas foram projetadas para: (i) trabalhar como membranas de regeneração para doenças peridontais e (ii) para a restauração da cartilagem articular através da engenharia de tecido. Além disso, foi proposto o uso do polímero de memória forma como sistema de ancoramento para o sensor da bexiga.

Abstract

In recent years, there has been increased interest in biodegradable polyurethane (PU) for use in biomedical; particularly the class of PUs with shape memory. In this thesis, six series of segmented PU with different hard segment content were prepared by the prepolymer mixing method in an aqueous environment. To improved PU properties further polyurethane/montmorillonite nanocomposites with different clay content were produced. PUs and their nanocomposites had their chemical structure, morphology, mechanical properties and shape memory properties investigated. The hydrolytic and alkaline degradation were also studied. The cellular viability and proliferation of cementoblasts and human mesenchymal stem cells were also investigated. The techniques applied were able to show that the hard-segment content and the hard-segment interactions were the two controlling factors for determining the structure of segmented PUs. Results showed that the degree of clay delamination within the polymer was able to tailor the phase morphology of the polymer. The polymer and the nanocomposites presented shape memory properties. The morphological changes during shape-memory cycles were examined. Recovery process was separated into three stages. The deformation cycle led to the formation of an oriented nanostructure derived from chain alignment. Bulk incompatibility and entropic recovery were the two controlling features for determining the final PU morphology. The recovery was observed to be also triggered by the strong interactions among hard domains. A relationship between the ability of the studied PU to recover their original shape and their original nanostructure was determined. Because the filler incorporation disturbs the formation of hydrogen bonds between amine and carbonyl group, interfering with the mobility of polymeric chains and the metastable structure formed during deformation, shape recovery was reduced by the presence of nanoparticles. Obtained PUs were designed: (i) to work as guided tissue regeneration membranes to treat periodontal diseases and (ii) for the repair of articular cartilage defects through tissue engineering. Furthermore, we propose the use of shape-memory polymer as anchoring system for a bladder sensor.

I – Introdução e objetivos do trabalho

Os polímeros convencionais já são empregados em praticamente tudo o que usamos hoje em dia: tecidos, medicamentos, embalagens, meios de transporte, comunicações, armazenamento de informações, etc. Por causa desse vasto mercado e da singularidade das propriedades da classe de polímeros com memória de forma, é pertinente prever também aplicações em quase todas as áreas de nossa vida diária para esse tipo de polímero. Porém, é na área médica onde os cientistas prevêem as aplicações mais nobres para esses materiais.

Previamente conformados em uma forma definida e temporária, polímeros biodegradáveis com memória de forma poderiam ser introduzidos no corpo do paciente através de uma pequena incisão. Após serem implantados na posição correta, e com a elevação da temperatura corporal, eles retornariam à forma apropriada (estado permanente). Durante o restabelecimento do paciente e o decorrer do tempo, o implante começaria a ser degradado pelo corpo, podendo ser absorvido pelo organismo, tornando, portanto, desnecessária uma nova cirurgia para remover o implante.

Para ser reconhecido como um polímero com memória de forma, o material polimérico deve ser capaz de conservar a forma temporária mesmo na ausência de tensões de deformação e deve ser apto a recuperar a forma permanente se induzido apropriadamente. Para isso, os polímeros são arquitetados possuindo duas fases com propriedades termomecânicas e morfológicas distintas: a fase reversível e a fase permanente. A fase permanente age como borracha para restaurar a forma original, e a fase reversível estabiliza a forma temporária.

Para a maioria dos polímeros com memória de forma, a recuperação da forma original é estimulada pela mudança na temperatura, sendo, por isso, classificada como mudança termicamente induzida. Entretanto, esse efeito também pode ser impelido por outras fontes, como o campo elétrico, a luz, ou mesmo o vapor.

Entre os polímeros com memória de forma conhecidos, as poliuretanas com memória de forma são os mais amplamente estudadas desde a sua descoberta em 1988 por Mitsubish Heavy Industries Ltda. O sucesso dessa família de polímeros deve-se principalmente à versatilidade de sua síntese e às propriedades macroscópicas que podem ser concebidas, de acordo com a necessidade de aplicação, tornando-os adequados tanto para aplicações convencionais quanto para aplicações de maior valor agregado.

I.1 – Polímeros com Memória de Forma

Desde a sua descoberta, em 1984, por cientistas japoneses, os polímeros com memória de forma ganharam espaço na comunidade científica do mundo inteiro [1, 2]. Tipicamente, esses materiais apresentam duas fases. Uma que fixa a forma temporária e outra que memoriza a forma permanente; ou seja, uma fase reversível e uma fase permanente. A fase permanente normalmente se apresenta sob a forma cristalina; a porção reversível, porém, pode possuir tanto a forma amorfa como a cristalina, sendo que neste último caso, a fase é constituída por cristais macios [3] facilmente deformáveis. Como a fase reversível pode ser facilmente conformada em uma forma arbitrária [4-7], ela também é conhecida como fase macia. A porção permanente, entretanto, não se deforma tão facilmente e por isso ela é conhecida como fase rígida.

Na maioria das vezes, a recuperação da forma original é estimulada pela mudança na temperatura, sendo classificada como mudança termicamente induzida. Entretanto, esse efeito pode ser controlado também por outras fontes, como o campo elétrico, a luz ou mesmo o vapor [8]. Na mudança termicamente induzida, para armazenar a forma temporária e recuperar a permanente, os polímeros com memória de forma utilizam-se de dois mecanismos. O primeiro baseia-se na variação do módulo de elasticidade com o aumento da temperatura. O segundo baseia-se na utilização da energia armazenada durante a deformação com força motriz para movimentação dessas cadeias [7, 9; 10].

A – Variação do Módulo de Elasticidade

Já é notório que os polímeros podem exibir um estado borrachoso a temperaturas superiores à temperatura de transição vítrea e um estado vítreo nas temperaturas abaixo

desta. Assim, devido ao baixo módulo de elasticidade do estado borrachoso, esses materiais podem ser submetidos a elevados valores de deformação elástica nas temperaturas elevadas. Como o módulo de elasticidade no estado vítreo é pelo menos duas vezes maior que no estado borrachoso, a energia previamente armazenada durante a deformação a quente não é alta o suficiente para permitir que as cadeias retornem à posição inicial quando no estado vítreo a tensão de deformação for suprimida. Como conseqüência, a deformação pode ser congelada se o material sob tensão for rapidamente resfriado a temperaturas inferiores. Entretanto, quando reaquecidos para o estado borrachoso, os polímeros utilizados usualmente não conseguem restaurar a deformação residual inelástica. Em contraste, os polímeros com memória de forma podem recuperar quase completamente toda deformação residual [3]. A Figura I.1 [3] mostra esquematicamente como o módulo de elasticidade varia com a alteração da temperatura para essa classe de materiais. Aqui T_d representa a temperatura de deformação; T_{des}, a temperatura de descarregamento; T_f, a temperatura de fusão do polímero; e T_{trans} é a temperatura de transformação do estado vítreo para o estado borrachoso. O módulo de elasticidade do estado vítreo é representado pelo índice v, e do estado borrachoso por *b*.

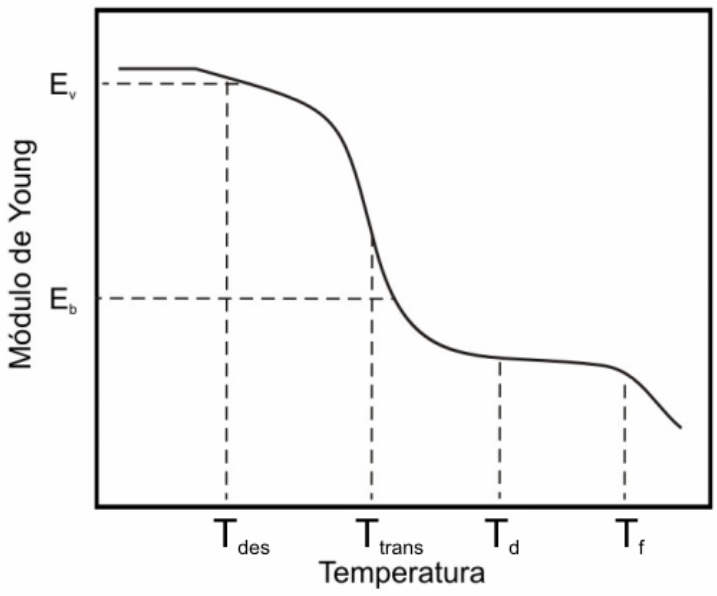

Figura I.1 – Variação do módulo de elasticidade com a temperatura [3].

Assim, a caracterização da resposta termomecânica dos polímeros com memória de forma pode ser definida por quatro temperaturas críticas [9]:

- A primeira é a temperatura de transformação, T_{trans}, é o ponto de referência para deformação e recuperação da forma permanente. Pode ser tanto caracterizada pela temperatura de fusão da fase reversível no caso de fase macia cristalina como pela temperatura de transição vítrea no caso de fase macia amorfa.

- A segunda é a temperatura de deformação, T_d, na qual o polímero é conformado em uma forma temporária. Dependendo do efeito de memória de forma desejado, T_d pode ser maior ou igual a T_{trans} [7].

- A terceira é a temperatura de armazenamento, T_A, temperatura na qual o polímero é mantido para fixar a forma temporária, podendo ser igual ou menor a T_d e/ou igual a T_{des}. Nessa temperatura, a forma temporária deve ser estável durante um longo período de tempo.

- A última é a temperatura de recuperação, T_r, sendo essa a temperatura em que o material recupera a forma original, com o reaquecimento. A recuperação da forma pode ocorrer isotermicamente a uma temperatura T_r fixa ou em uma faixa de temperatura maior ou igual a T_r.

Esquematicamente, pode-se classificar o efeito de memória de forma em quatro etapas, representadas conforme Figura I.2:

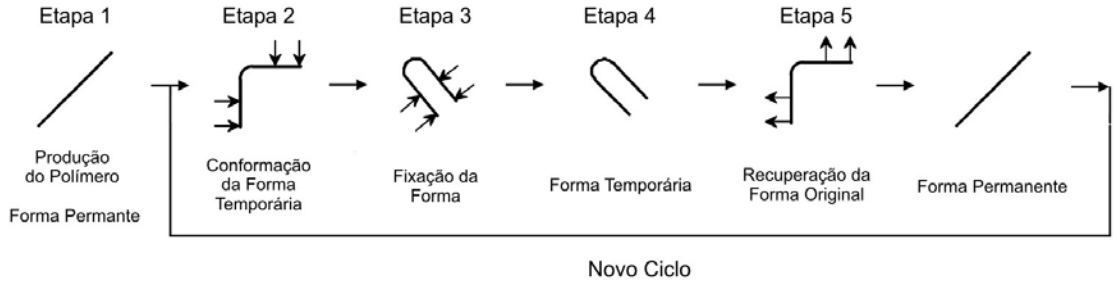

Figura I.2 - Representação do efeito de memória de forma para polímeros.

Etapa 1 – Conformação da forma temporária: primeiramente, o polímero é conformado na forma inicial desejada (moldado e curado). Na sua condição original, ele é conformado em um formato desejado na T_d.

Etapa 2 – Fixação da forma temporária: nesta etapa o material, ainda sob a ação da tensão de deformação, é mantido na temperatura T_A.

Etapa 3 – Forma temporária: a força externa é removida. Usualmente, o polímero consegue reter a forma temporária até que a recuperação da forma original seja necessária.

Etapa 4 – Recuperação da forma original: para recuperar a forma original, o polímero é novamente aquecido até T_r.

Segundo Kim *et al*. [3], um polímero com alto módulo de elasticidade no estado vítreo, E_v, fornecerá materiais com alta fixação da forma temporária durante a Etapa 2. Se, entretanto, esses materiais possuírem alto módulo de elasticidade no estado borrachoso, E_b, pode-se esperar alto grau de recuperação da forma permanente durante a Etapa 4. Ademais, quanto mais pronunciada for a transição do estado vítreo para o estado borrachoso, maior será a sensibilidade do material à variação de temperatura. Os autores [3] também salientam que quando o polímero obedece à relação $E_v / E_b \geq 2$, ele pode ser facilmente conformado na Etapa 1 e possuirá grande resistência mecânica na Etapa 3.

B – Variação da Energia Armazenada

Durante as Etapas 1 e 2 do ciclo de programação, um estado instável de menor entropia pode ser armazenado nas cadeias poliméricas. Assim, na Etapa 4, com o reaquecimento acima de T_{trans}, a forma permanente pode ser recuperada através do aumento no volume livre da rede, da reorganização das cadeias e da conseqüente recuperação do estado mais estável de alta entropia.

A recuperação da energia configuracional estável será possível somente se o polímero possuir uma densidade ótima de pontos de rede capazes de formar uma rede polimérica "memoriável". Esses pontos ocorrerão como ligações cruzadas de natureza química; ou ligações cruzadas de natureza física no caso de regiões cristalinas [3].

I.2 – Poliuretanas com Memória de Forma

O termo poliuretana é usado para designar uma família de polímeros que geralmente contém grupos uretanos em sua cadeia principal e que são freqüentemente obtidos por meio de reações de dióis com diisocianatos. Entre as propriedades mais típicas das poliuretanas, podemos citar: (1) alta resistência a solventes orgânicos e a soluções aquosas, (2) grande estabilidade contra exposição à luz solar, e (3) possível biocompatibilidade.

Desde a sua descoberta, em 1937, por Otto Bayer, até hoje, os poliuretanos talvez sejam a família de polímeros mais vastamente empregada e a mais amplamente estudada [11-13], devendo muito dessa popularidade a sua facilidade de síntese e a sua diversidade de formas. Dependendo da estrutura química e da funcionalidade dos reagentes empregados na formulação, bem como das condições de síntese, as poliuretanas podem se apresentar tanto na forma de um termoplástico como na forma de termofixo, elastômero ou fibra, na forma expandida ou não [14].

Poliuretanas segmentadas são basicamente copolímeros em bloco que apresentam segmentos alternados com propriedades diferentes [3]. Esses segmentos produzidos por macro-meros diferentes são caracterizados por ligações cruzadas químicas irreversíveis entre os segmentos e ligações cruzadas secundárias e reversíveis entre as cadeias poliméricas. Estas são interações fracas que podem incluir interações de hidrogênio e ligações iônicas. Uma variedade especial das poliuretanas segmentadas é a classe das poliuretanas elastômeros-termoplásticas que combinam as propriedades da borracha vulcanizada com as vantagens do processamento dos polímeros termoplásticos, isto é, podem ser repetidamente fundidos e processados devido à ausência da rede química que normalmente existe nas borrachas, podendo ser, portanto, usados em muitas aplicações

e reciclados [15, 16]. Além de poderem ser reciclados, essa classe conta com outras vantagens [16]: (1) custo moderado, (2) alta elasticidade, (3) boa flexibilidade, (4) alta resistência ao rasgamento, (5) resistência à oxidação, e (6) resistência à umidade.

As poliuretanas elastômero-termoplástica são normalmente copolímeros lineares contendo segmentos macios e segmentos rígidos [17]. Na sua grande maioria, os segmentos rígidos são diisocianatos e um extensor de cadeia diol e/ou a diamina de baixa massa molar. Os segmentos macios são, por sua vez, formados por poliéter ou poliéster glicol, ambos os quais podem ser estendidos por diisocianatos [3, 17]. Os segmentos macios típicos são amorfos e possuem massa molar entre 1000 g/mol e 2000 g/mol, enquanto que os segmentos rígidos, devido a suas ligações cruzadas fortes, podem ser cristalinos [3]. A Figura I.3 mostra um exemplo de um poliuretano segmento, sintetizado a partir de polietilenoglicol.

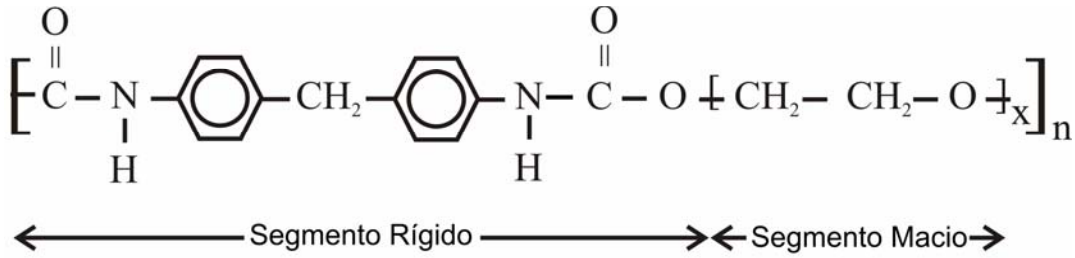

Figura I.3 – Exemplo de um poliuretano segmento, sintetizado de poliglicol.

Essa estrutura de multi-fases, responsável pelas propriedades especiais das poliuretanas elastômeros-termoplásticas, foi proposta primeiramente por Cooper e Tobolsky [13], sendo conseqüência [4, 17]:

- da diferença de estrutura,
- das interações repulsivas, e
- da incompatibilidade termodinâmica entre os segmentos macios e rígidos.

Entretanto, a separação das fases é incompleta, e as regiões podem conter intercalada certa quantidade do outro segmento [13, 17, 18].

Como cada uma das micro-fases pode ser manipulada para uma aplicação específica, elas podem possuir temperaturas de transição térmica diferentes e manipuláveis. Quando os segmentos são manipulados para possuírem temperaturas de transição diferentes, as poliuretanas segmentadas podem satisfazer as demandas para o efeito memória de forma termicamente ativado, sendo por isso conhecidos como poliuretanas com memória de forma.

Desde a sua descoberta pela Mitsubishi Heavy Industries Ltda, em 1988, as poliuretanas com memória de forma são um dos materiais com memória de forma mais amplamente estudados [8, 10].

Nas poliuretanas com memória de forma, o segmento rígido é o segmento responsável pela fixação da forma permanente, e o segmento macio, pela fixação da forma temporária. Além das ligações cruzadas, o emaranhamento de cadeia e a formação de cristais podem ser utilizados na memorização da forma original [6, 10, 19, 20]. A forma temporária, entretanto, depende da temperatura de transição vítrea ou da temperatura de fusão do segmento macio que forma a fase reversível [6, 10, 19, 20].

Devido ao movimento aleatório das cadeias e à restrição da movimentação das cadeias do segmento macio pela fase cristalina do segmento rígido, é observada elasticidade da borracha na faixa de temperatura entre a temperatura de recuperação de forma e a temperatura de fusão dos segmentos rígidos [19]. Por isso, quando o material na forma temporária é aquecido a temperaturas superiores à temperatura de recuperação, o efeito memória de forma é observado, isto é, a forma original é restaurada pela energia armazenada durante a deformação [19].

I.3 – Variáveis que Influenciam as Propriedades das Poliuretanas Segmentadas

As propriedades finais das poliuretanas com memória de forma não são determinadas somente pela composição química e morfologia das cadeias dos segmentos rígidos e macios, mas também pela separação relativa das fases, pela morfologia geral do

polímero e pelas variáveis de processamento, como as condições de síntese, a história mecânica e a história térmica. Assim, a relação entre processo-estrutura-propriedade é muito complexa e todos os parâmetros que incluem a formulação, condição de síntese, condição de processamento e condições térmicas devem ser cuidadosamente especificados, para evitar interpretações ambíguas e discussão de resultados.

A – Separação de Fase

O grau de separação das micro-fases é um dos parâmetros-chave para se controlar as propriedades físicas das poliuretanas segmentadas, sendo que, quanto mais forte for a interação dos segmentos rígidos, maior será a separação de fases e a formação de domínios [8].

Como resultado da reação aleatória de poliadição que une os segmentos rígidos aos macios via extensores de cadeia e da grande dispersão de massa molar dos componentes utilizados na reação, o nível de separação de fases é, na maioria das vezes, baixo [21]. Busca-se, entretanto, um ponto ótimo de separação de fases, já que a mistura das fases pode tanto favorecer uma série de propriedades como prejudicar tantas outras.

Sabe-se, por exemplo, que a maior separação de fases favorece a resistência mecânica do polímero porque favorece a formação do domínio rígido [22]. Contudo, como o segmento macio tende a segregar na superfície do polímero [23], o aumento pronunciado da separação de fases será acompanhado pela diminuição da resistência à abrasão. Além disso, o aumento da separação das fases poderá favorecer a cristalização do segmento macio [3].

O grau de separação de fases [1] também afeta as propriedades de memória de forma porque modifica as fases responsáveis pela retenção da forma temporária (fases macia) e recuperação da forma original (fase rígida).

B – Segmento Rígido

Várias das propriedades das poliuretanas com memória de forma são afetadas pela morfologia, pela estrutura e pela proporção do segmento rígido. Algumas das interações entre as cadeias poliméricas responsáveis pela formação do segmento rígido são [8, 17]:

- interações de hidrogênio entre os grupos carbonila – Figura I.4(a),
- interação do tipo dipolo-dipolo entre os segmentos rígidos – Figura I.4(b), e
- interação do tipo dipolo induzido entre os grupos aromáticos – Figura I.4(c).

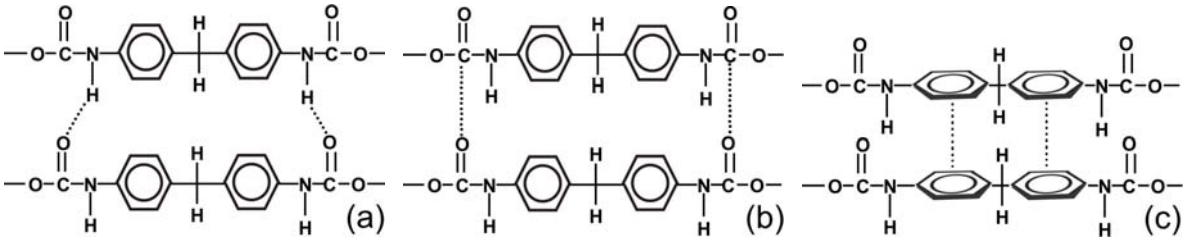

Figura I.4 - Representação das ligações cruzadas do segmento rígido: (a) interações de hidrogênio, (b) dipolo-dipolo, (c) dipolo-dipolo induzido.

Devido ao seu papel fundamental na retenção da forma temporária e na determinação das propriedades mecânicas, muito esforço tem sido empregado no sentido de entender como o trio morfologia, proporção e estrutura do segmento rígido pode modificar as propriedades finais dos poliuretanas com memória de forma.

C – Segmento Macio

O efeito memória de forma é resultado da movimentação molecular que ocorre no segmento macio. Por isso, sua cristalinidade determina a temperatura de recuperação [24] de tal modo que o efeito memória de forma pode ser controlado pela massa molar e pela proporção desse segmento e também pelo processo de polimerização [25, 26].

I.4 – Objetivos e Organização desta Tese

Este trabalho tem por objetivos:

- Preparar uma série de poliuretanas biodegradáveis com nanopartículas de argilominerais que apresente memória de forma;

- Caracterizar as propriedades morfológicas e termomecânicas, assim como a memória de forma dos materiais produzidos;

- Definir o potencial como biomaterial;

- Contribuir para o entendimento das mudanças morfológicas durante o ciclo de memória de forma.

O trabalho busca, assim, promover uma nova direção no planejamento de sistemas com memória de forma nos quais as propriedades poderão ser ajustadas conforme a morfologia das fases.

Visando atingir os objetivos gerais propostos, o desenvolvimento deste trabalho foi dividido em diversas etapas representadas pelos capítulos da tese. Essas etapas podem ser divididas em quatro grandes áreas, Figura I.5.

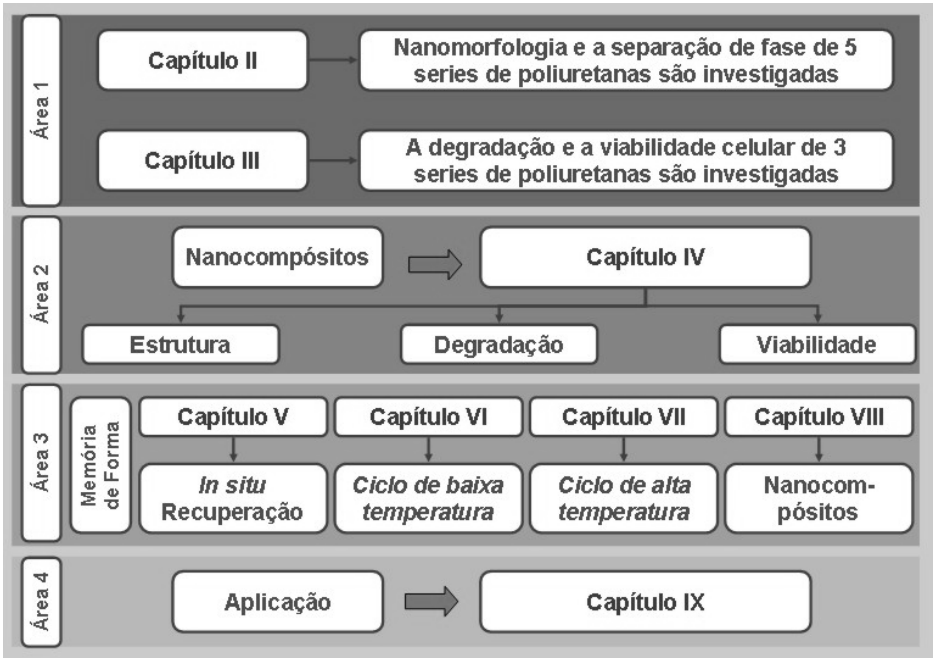

Figura I.5 - Representação das áreas abrangidas durante o trabalho de tese.

A primeira área reúne o desenvolvimento da rota de síntese, a caracterização das propriedades dos polímeros obtidos além da determinação da viabilidade celular do material. Nessa grande área, primeiramente, cinco séries de poliuretanas segmentadas com diferentes concentrações de segmento rígido foram produzidas pelo processo pré-polímero. A nanomorfologia e a separação de fase dos materiais obtidos foram investigadas por espectroscopia de absorção de infravermelho, calorimetria diferencial exploratória modulada e espalhamento de raios X de pequeno ângulo. Neste estudo, as técnicas aplicadas mostraram que a concentração do segmento rígido e as interações de hidrogênio são dois fatores determinantes para as propriedades dos materiais obtidos. Essa etapa corresponde ao Capítulo II dessa tese, o qual corresponde a artigo aceito no 10º Congresso Brasileiro de Polímeros. Em seguida, com o objetivo de estabelecer o potencial como biomaterial dos polímeros obtidos, três séries de poliuretanas segmentadas com diferentes concentrações de segmento rígido foram projetadas para engenharia de tecido cartilaginoso. Durante as investigações, estudaram-se as propriedades morfológicas, bem como a degradação dos materiais obtidos. A viabilidade celular, a adesão e a proliferação de células-tronco derivadas de tecido adiposo também foram investigadas – Capítulo III (que corresponde a artigo submetido à publicação no Journal of Material Science - Materials in Medicine).

A segunda grande área compreende o desenvolvimento e a caracterização dos nanocompósitos. Nessa área, o efeito da adição de nanopartículas de argilominerais nas propriedades morfológicas e mecânicas, o efeito na degradabilidade, assim como a viabilidade celular foram investigados por meio de cinco séries de nanocompósitos. Esses nanocompósitos foram projetados com o propósito de serem utilizados como membranas biodegradáveis para o tratamento de doenças periodontais – Capítulo IV (que se trata de artigo publicado no Journal of Applied Polymer Science).

Tendo sido investigadas as propriedades morfológicas e as aplicações biomédicas das poliuretanas obtidas e de seus nanocompósitos, estuda-se na terceira grande área o efeito memória de forma dos polímeros e dos nanocompósitos. Para isso, a técnica espalhamento de raios X de pequeno ângulo foi utilizada para investigar o papel da nanomorfologia durante o ciclo de memória de forma. Primeiramente, no experimento in situ, Capítulo V (que corresponde a artigo aceito no 10º Congresso Brasileiro de

Polímeros), uma amostra deformada foi aquecida, e a recuperação da forma foi monitorada por 20 minutos. Ainda nesse capítulo, a composição das fases foi investigada quando amostras deformadas foram submetidas a diferentes ciclos térmicos. Em seguida, no Capítulo VI (que se trata de artigo aceito no 10º Congresso Brasileiro de Polímero), a influência do grau de separação de fase e das interações de hidrogênio no efeito memória de forma foi estudada durante um ciclo de memória de forma de baixa temperatura, isto é, temperatura de deformação abaixo de T_{trans}. Para tanto, três séries de poliuretanas com diferentes concentrações de segmento rígido foram produzidas. A morfologia das espécies não deformada, deformada e recuperada foram investigadas por espectroscopia de absorção de infravermelho, calorimetria diferencial exploratória modulada e espalhamento de raios X de pequeno ângulo. Logo após, a influência do grau de separação de fase e das interações de hidrogênio no efeito memória de forma foi estudada, durante um ciclo de memória de forma de alta temperatura, isto é, temperatura de deformação acima de T_{trans} – Capítulo VII. Finalmente, As propriedades de memória de forma dos nanocompósitos foram investigadas durante o ciclo de memória de forma de alta temperatura e também durante o ciclo de baixa temperatura – Capítulo VIII (que corresponde a artigo aceito no 10º Congresso Brasileiro de Polímeros).

Por último, na última grande área, desenvolve-se uma aplicação para o material obtido utilizando o efeito memória de forma em um sistema de ancoragem de sensores de pressão para bexiga – Capítulo IX (submetida a registro de patente).

I.5 – Referências Bibliográficas

1 – Tobushi H; Hara H, Yamada E, Hayashi S. Thermomechanical properties in a thin film of shape memory polymer of polyurethane series. Smart Mater Struct 1996;5(4):483-91.

2 – Wei ZG, Sandstrom R, Miyazaki S. Shape-memory materials and hybrid composites for smart systems. Part I shape-memory materials. J Mater Sci 1998;15(1):3743-62.

3 – Kim BK, Lee SY, Xu M. Polyurethanes having shape memory effects. Polymer, 1996;37(26):5781-93.

4 – Chen LW, Lin JR. Study on shape-memory behavior of polyether-based polyurethanes. II. Influence of soft-segment molecular weight. J Appl Polym Sci 1998;69(8):1575-86.

5 – Chen LW, Lin JR. Shape-memorized crosslinked ester-type polyurethane and its mechanical viscoelastic model. J Appl Polym Sci 1999;73(7):1305-19.

6 – Lendlein A, Kelch S. Shape-memory polymers. Angew Chem Int Ed 2002;41(12): 2035-57.

7 – Gall K, Dunn ML, Liu Y, Stefanic G, Balzar D. Internal stress storage in shape memory polymer nanocompositos. Appl Phys Lett 2004;85(2):290-292.

8 – Cho JW, Sahoo NG, Jung YC, Goo NS. Conducting shape memory polyurethane-polypyrrole composites for an electroactive actuator. Macromolecular Materials and Engineering 2005;290(11):1049-55.

9 – Gall K, Dunn M.L, Liu Y, Finch D, Lake M, Munshi N.A. Shape memory polymer nanocompósitos. Acta Materialia 2002;50(20):5115-26.

10 – Xu J, Shi W, Pang W. Synthesis and shape memory effects of Si–O–Si cross-linked hybrid polyurethanes. Polymer 2006;47(1):457-65.

11– Coleman PC, Skrovanek DJ, Painter MM. Hydrogen bonding in polymers. Macromolecules 1986;19:699.

12 – Coleman PC, Painter MM, Lee KH, Skrovanek DJ. Hydrogen bonding in polymers. 4. Infrared temperature studies of a simple polyurethane. Macromolecules 1986;19:2149.

13 – Cooper SL, Tobolsky AV. Properties of linear elastomeric polyurethanes. J Appl Polym Sci 1966;10(12):1837-44.

14– Canevarolo Jr, SV. Ciência dos polímeros. 2.ed. São Paulo: Artliber Editora 2002. 183p.

15– Beck RA, Truss RW. Effect of chemical structure on the wear behaviour of polyurethane-urea elastomers. Wear 1998;218:145–52.

16 – Elleuch R, Elleuch K, Salah B, Zahouani H. Tribological behavior of thermoplastic polyurethane elastomers. Materials & Design In Press Corrected Proof Available online 6 January 2006.

17– Pompe G, Pohlers A, Pötschke P, Pionteck J. Influence of processing conditions on the multiphase structure of segmented polyurethane. Polymer 1998;39(21):5147-53.

18 – Harris R.F, Joseph M.D, Davidson C, De Porter C.D. Dais V.A. Effects of hard segment concentration on polyurethane elastomers based on molecular weight advanced poly(ethylene ether carbonate) diols. J Appl Polym Sci 1990;41(3-4):509-525

19 – Kim BK, Shin YJ, Cho SM, Jeong HM. Shape-memory behavior of segmented polyurethanes with an amorphous reversible phase: the effect of block length and content. J Appl Polym Sci Part B 2000;38(20):2652-7.

20 – Kim B.K, Jeong H.M, Song J.H, Lee S.Y. Miscibility and shape memory property of poly(vinyl chloride)/thermoplastic polyurethane blends. J Mater Sci 2001,36(22);5457-63.

21 – Polizos G, Kyritsis A, Pissis P, Shilov V, Shevchenko VV. Structure and molecular mobility studies in novel polyurethane ionomers based on poly(ethylene oxide). Solid State Ionics 2000;137(2):1139-46.

22 – Nakamae K, Nishino T, Asaoka S, Sudaryanto. Microphase separation and surface properties of segmented polyurethane - Effect of hard segment content. Int J of Adhesion and Adhesives 1996;16(4):233-239.

23 – Nakamae K, Nishino T, Asaoka S, Sudaryanto. Relationships between interfacial properties and structure of segmented polyurethane having functional groups. Int J Adhesion and Adhesives 1999;5:345-351.

24 – Wang M, Luo X, Ma D. Dynamic mechanical behavior in the ethylene terephthalate-ethylene oxide copolymer with long soft segment as a shape memory material. Eur Polym J 1998;34:1-5.

25 – Xiu Y, Wang D, Hu C, Ying S, Li J. Morphology-property relationship of segmented polyurethaneurea: Influences of soft-segment structure and molecular weight. J Appl Polym Sci 1993;48(5):867-9.

26– Wilkes GL, Abouzahr S. Structure-property studies of polyester- and polyether based MDI_BD segmented polyurethanes: effect of one- vs. two stage polymerization conditions. J Appl Polym Sci 1984;29(9):2695-11.

Chapter II (Capítulo II)

Study of the morphology exhibited by linear segmented polyurethanes

I. M. Pereira[1,2]; R. L. Oréfice[2*]

[1]Coordenação de Metalurgia – Centro Federal de Educação Tecnológica de Minas Gerais – CEFET/MG Campus VII – Timóteo-MG
[2]Departamento de Engenharia Metalúrgica e de Materiais – Universidade Federal de Minas Gerais – UFMG, Belo Horizonte-MG

Abstract:

Five series of segmented polyurethanes with different hard segment content were prepared by the prepolymer mixing method. The nano-morphology of the obtained polyurethanes and their microphase separation were investigated by infrared spectroscopy (FTIR), modulated differential scanning calorimetry (MDSC) and small-angle X-ray scattering (SAXS). Although highly hydrogen bonded hard segments were formed, high hard segment contents led to the presence of hard segment dissolved within soft domain and reduced the chain mobility, decreasing the hard domain precipitation and the soft segment crystallization. The applied techniques were able to show that the hard-segment content and the hard-segment interactions were the two controlling factors for determining the structure of segmented polyurethanes.

Keywords: Segmented polyurethanes, SAXS, microphase separation, and nano-morphology

II.1 – Introduction

Segmented polyurethanes (PUs) are multiblock copolymers which consist of the so-called hard and soft segments. The multi-phase structure of PUs results from the repulsive interaction between dissimilar segments and thermodynamic immiscibility of hard and soft segments at low temperature. The microphase separation structure of PUs depends on many factors, including structure and molecular weight of the soft segment, nature of chain extender, hard segment content and interactions, thermal and solvent history during sample preparation [1-4].

In the present work, PUs were synthesized in an aqueous environment by combining hard segments derived from aliphatic isophorone diisocyanate with soft segments based on poly(caprolactone diol). Five series of PUs having different hard segment contents were synthesized. The infrared spectroscopy (FTIR), modulated differential scanning calorimetry (MDSC) and small-angle X-ray scattering (SAXS) were used to provide information about the nano-morphology of the obtained PUs and on their microphase separation.

FTIR provides information about the vibration of the atomic and the molecular species and can reveal the structure of the polymer and presence of interactions between polymer molecules. MDSC measures, applying identical thermal cycles, the difference in the amount of heat required to increase the temperature of a sample and a reference as a function of temperature. SAXS involves measuring the scattering intensity as a function of the angle measured with respect to the direction of the incident X-ray beam. The patterns and intensity distribution of SAXS are due to local heterogeneities in the electron density of the material [5, 6].

II.2 – Materials and Methods

A – Polymer synthesis

Poly(caprolactone diol) (PCL – Mn = 530, 1250, 2000, 10000 g mol^{-1}), isophorone diisocyanate (IPDI), 2,2-bis(hydroxymethyl), propionic acid (DMPA) and dibutyl tin dilaurate (DBDLT) were obtained from Aldrich (St. Louis, MO). Triethylamine (TEA, 98%) and hydrazine (HZ, 25%) were purchased from Vetec (RJ, Brazil). All these chemicals were employed throughout this work without any previous treatment. PUs were prepared by the prepolymer mixing method, according to a procedure that will be described in Chapter IV [7]. The feed ratios are shown in Table II.1, where $W(HS)$ is weight fraction of hard segment content, obtained according to Equation. II.1.

$$W(HS) = \frac{Weight_{IPDI} + Weight_{HZ}}{Weight_{PU}} \times 100 \quad \text{(II.1)}$$

Table II.1 – Composition (wt.%) of waterborne PUs

	PCL				DMPA	IPDI	HZ	TEA	$W(HS)$
	530	1250	2000	10000					
PU530	34.3	–	–	–	6.6	50.5	3.6	4.9	57.0
PU1250	–	55.4	–	–	4.5	34.6	2.1	3.4	38.0
PU2000	–	–	66.1	–	3.3	25.8	1.9	3.0	28.5
PU10000&530	7.1	–	–	72.0	2.1	16.1	1.2	1.6	17.5
PU10000	–	–	–	90.8	0.9	7.1	0.5	0.7	7.6

B – Infrared spectroscopy

Infrared spectra were collected in a Fourier transform infrared spectrophotometer (FTIR; Perkin–Elmer, model Spectrum 1000). Measurements were carried out using the attenuated total reflectance (ATR) technique. Each spectrum was a result of 64 scans with a resolution of 4 cm^{-1}.

C – Modulated differential scanning calorimetry (MDSC)

MDSC measurements were performed using a TA Instruments 2920. The following protocol was applied to each sample: (1) heating from room temperature to 110°C at 15°C min^{-1}, (2) holding for 3.00 min at 110°C, (3) cooling to –110°C at 3.00°C/min, modulating +/– 1.00°C every 60 s. The glass transition temperatures (T_g) were obtained by the analysis software of the calorimeter.

D – Synchrotron small angle X-ray scattering (SAXS)

SAXS measurements of synchrotron small angle X-ray scattering were performed using the beam line of the National Synchrotron Light Laboratory (LNLS, Campinas, Brazil). After passing through a thin beryllium window, the beam is monochromatized ($\lambda = 1.488$ Å) and horizontally focused by a cylindrically bent and asymmetrically cut silicon single crystal. The X-ray scattering intensity, $I_{(q)}$, was experimentally determined as a function of the scattering vector, q, whose modulus is given by Equation II.2:

$$q = \frac{4\pi}{\lambda}\sin\theta \qquad \text{(II.2)}$$

where λ is the X-ray wavelength and θ represents half the scattering angle.

Each SAXS pattern corresponds to a data collection time of 900 s. From the experimental scattering intensity produced by all the studied samples, the parasitic scattering intensity produced by the collimating slits was subtracted. All SAXS patterns were corrected for the non-constant sensitivity of the position sensitive X-ray detector, for the time varying intensity of the direct synchrotron beam and for differences in sample thickness. Because of the normalization procedure, the SAXS intensity was determined for all samples in the same arbitrary units so that they could be directly compared. The sample-detector distance of 551.6 mm was used during the measurements.

II.3 – Results and discussion

Typical infrared spectra of obtained PUs are shown in Figure II.1. As shown, the position of the absorption bands of each specific functional group was similar for all obtained PUs.

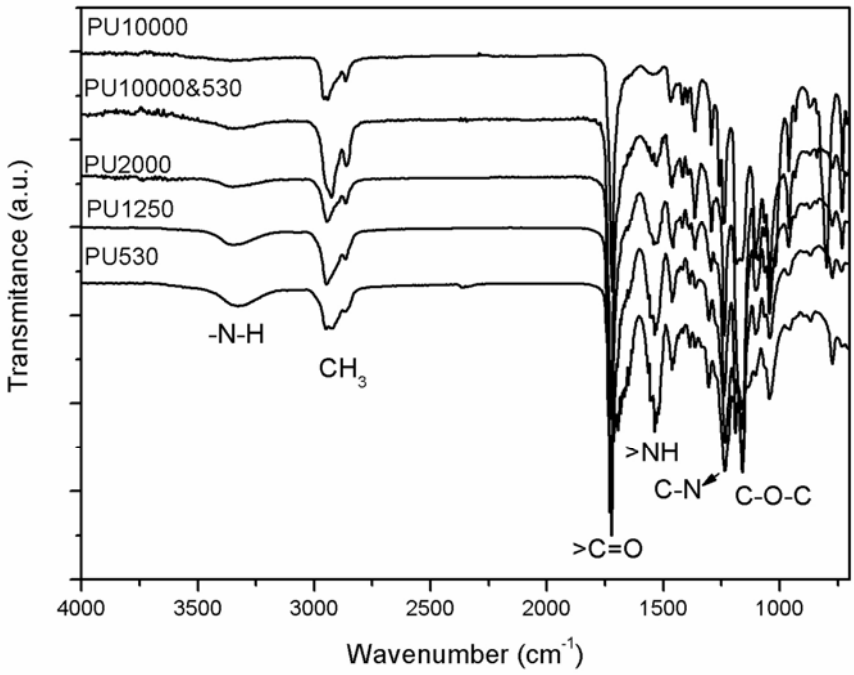

Figure II.1 – FTIR spectra of PU530, PU1250, PU2000, PU10000&530 and PU10000 samples

The primary amine stretching modes appear at 3600–3150 cm^{-1}. The absorption band at about ~3300 cm^{-1} corresponds to hydrogen bonded –N–H group and absorption at ~3500 cm^{-1} to nonbonded –N–H. The carbonyl group stretching vibrations, C=O, appear at 1760–1600 cm^{-1}. A series of specific absorption bands are present within the 1760–1600 cm^{-1} broad band, such as the absorption band due to the ester bond from PCL soft segments and others associated with multiple interactions between urea and urethane bonds and –N–H groups. IR bands at ~1720 cm^{-1}, ~1700 cm^{-1}, ~1660 cm^{-1}, ~1630 cm^{-1} are assigned, respectively, to free urethane stretching band, hydrogen bonded urethane stretching band, free urea stretching band and hydrogen bonded urea stretching band. The secondary amide absorption, >N–H, appears at 1640–1540 cm^{-1}. The band at 1150 cm^{-1} is assigned to the stretching of the –C–O–C– group [7].

Hydrogen bonding is known as an important driving force for the phase separation of a hard segment from a soft-segment matrix. Thus, the carbonyl region has generally been investigated for the quantitative study of microphase separation or mixing in PU [8]. However, two main spectral regions are of interest in studying the hydrogen bonding of segmented PUs: N–H and C=O, respectively, primary amine stretching and carbonyl group stretching. Since band overlapping is observed, a deconvolution mathematical procedure (using the PickFiT® software) was performed on spectra of Figure II.1 to enhance resolution of each individual band.

The extent of the –NH groups participating in hydrogen bonding can be expressed by a (–NH) hydrogen-bonding index $HBI_{(-NH)}^{(\%)}$, Equation II.3.

$$HBI_{(-NH)}^{(\%)} = \frac{NH_{Bonded}}{NH_{Bonded} + NH_{Free}} \times 100 \qquad \text{(II.3)}$$

where NH_{Bonded} and NH_{Free} are respectively the band peak area of bonded and free –NH groups.

The extent of the carbonyl absorption groups participating in hydrogen bonding can be expressed by a hydrogen-bonding index $HBI_{(C=O)}^{(\%)}$, which is the fraction of hydrogen bonded in the carbonyl groups stretching vibrations Equation II.4 [9-11].

$$HBI_{(C=O)}^{(\%)} = \frac{A_{1700} + A_{1640}}{A_{1700} + A_{1640} + A_{1724} + A_{1660}} \qquad \text{(II.4)}$$

where A_{1724}, A_{1700}, A_{1660}, and A_{1640} are respectively the band peak area of free urethane, bonded urethane, free urea, bonded urea and ester.

The degree of phase mixture, $DPM(\%)$, can be calculated from the fraction of hard segment dissolved in soft domain, Equation II.5 [9].

$$DPM(\%) = \frac{\left(1 - HBI_{(C=O)}^{(\%)}\right) \times W(HS)}{\left(1 - HBI_{(C=O)}^{(\%)}\right) \times W(HS) + \left(1 - W(HS)\right)} \quad \text{(II.5)}$$

The IR bands at 1160 cm^{-1} and 1190 cm^{-1} in Figure II.1 are associated, respectively, with C–O amorphous and crystalline bands. As band overlapping also occurs, deconvolution procedures were performed. The separated curves are shown in Figure II.2. The FTIR crystallinity index, α_{FTIR}, was defined according to Equation II.6:

$$\alpha_{FTIR} = \frac{A_{1190}}{A_{1190} + A_{1160}} \times 100 \quad \text{(II.6)}$$

where A_{1190} and A_{1160} are respectively the band peak area of C–O amorphous and crystalline band.

Figure II.2 illustrates the deconvolution procedure used to determine the overlapped band of FTIR spectrum of obtained PUs. Results are summarized in Table II.2.

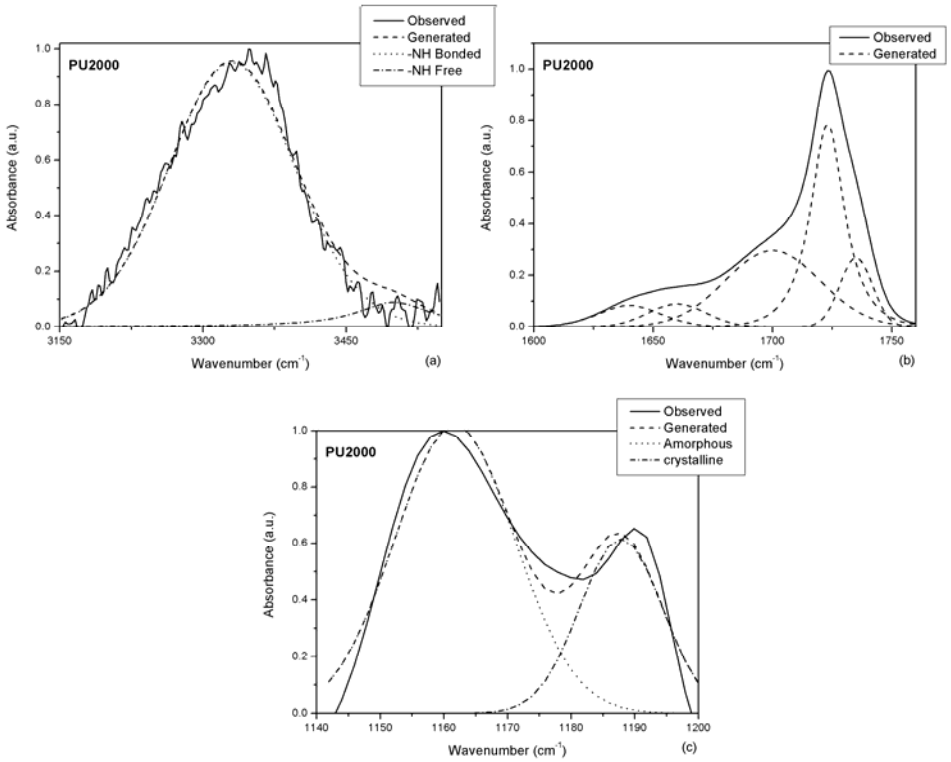

Figure II.2 – Illustration of the deconvolution procedure of PU2000: (a) primary amine stretching, (b) carbonyl group stretching and (c) ether stretching.

Table II.2 – FTIR results of as-molded poly(ester–urethanes)

	$HBI^{(\%)}_{(-NH)}$	$HBI^{(\%)}_{(C=O)}$	α_{FTIR}	DPM (%)
PU530	96.2	54.2	0.000	37.7
PU1250	98.9	46.3	6.8	24.8
PU2000	94.4	54.7	29.1	15.3
PU10000&530	85.4	46.5	41.6	10.2
PU10000	63.6	31.8	54.8	5.3

The multi-phase structure of PUs is a result of the repulsive interaction between dissimilar segments and thermodynamic immiscibility of hard and soft segments at low temperature [2, 3, 12].

A linear relationship between hard segment content and $DPM(\%)$ is shown in Figure II.3(a). PUs having high hard segment, i.e. PU530, contents were produced by using low molar mass PCL oligomers that display higher levels of chain mobility. This enhanced mobility can be useful in allowing urethane and urea groups to align themselves to form hydrogen bonds. The highly hydrogen bonded hard segments act as physical cross-links, restricting segmental motion of the polymer chain. However, it does not result in a more significant phase separation between hard and soft segments because the weight fraction of hard segment is high enough to still led to some hard segment dissolution. On the other hand, the lower values of $HBI(\%)$ of PU10000 does not result in a more extensive phase mixing since the reduction in hydrogen bonding within hard segments was compensated by an increase in the amount of soft segments. The hard segment content also controls the total number of hydrogen bonded NH groups, Figure II.3(b), as another evidence of the relationship between hard segment content and phase mixture.

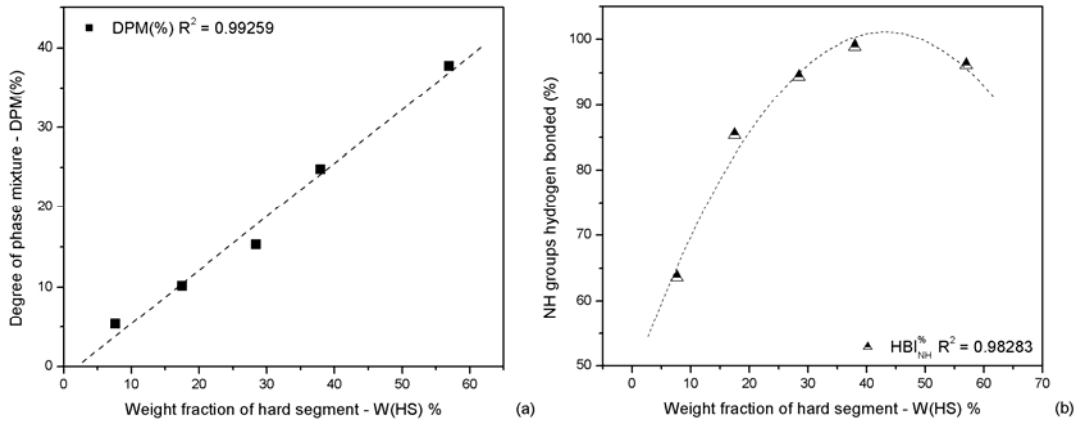

Figure II.3 – (a) Influence of hard segment content on degree of phase mixture and (b) number of hydrogen bonded NH groups.

The thermal behavior of the obtained PUs during cooling is shown in Figure II.4(a). Thermal properties are summarized in Table II.3. The glass transition temperature, T_g, is observed around –60°C. In DSC analysis, the width of the transition zone provides a qualitative measure of phase homogeneity, and the variation in the magnitude of T_g can indicate the degree of microphase separation [13]. Higher degrees of hard segment dissolved in the soft domains shift the phase transition moving T_g to higher values, Figure II.4(b).

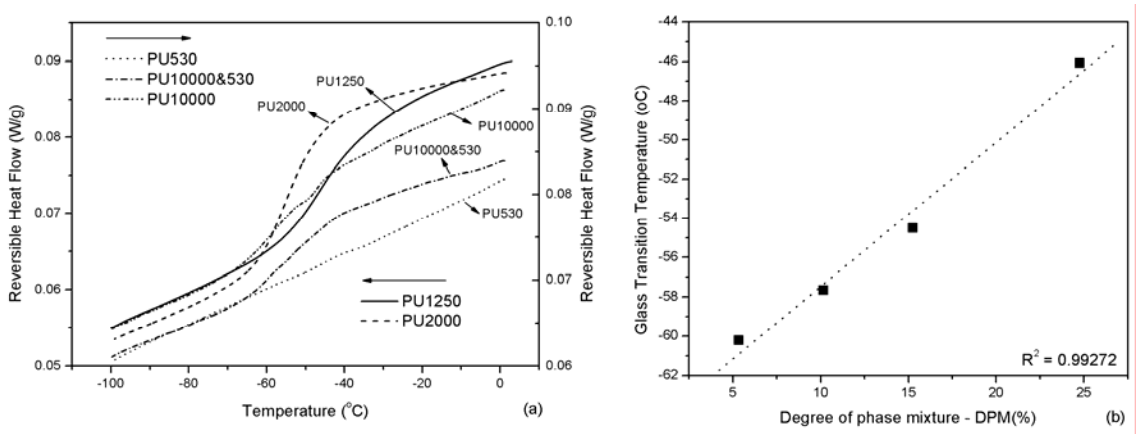

Figure II.4 – (a) DSC curves of obtained PUs (b) influence of the hard segment on glass transition

Table II.3 – DSC results of obtained poly(ester urethane).

	T_g (^oC)	T_{onset} (^oC)	T_{end} (^oC)	Zone width
PU1250	–46.1	–53.8	–33.6	20.2
PU2000	–54.5	–59.6	–46.4	13.2
PU10000&530	–57.7	–64.6	–45.5	19.1
PU10000	–60.2	–64.1	–53.1	11.0

Figure 5 illustrates SAXS 2D pattern of the obtained PUs. The patterns and intensity distribution of SAXS are dependent on the shape, the size and size distribution of scattering objects [6]. Different nano-morphologies are observable, varying from one phase system to multiphase polymers. Differences in electron density of phases that fluctuate from a low phase density to highly packed structures are responsible for the observed scattering pattern.

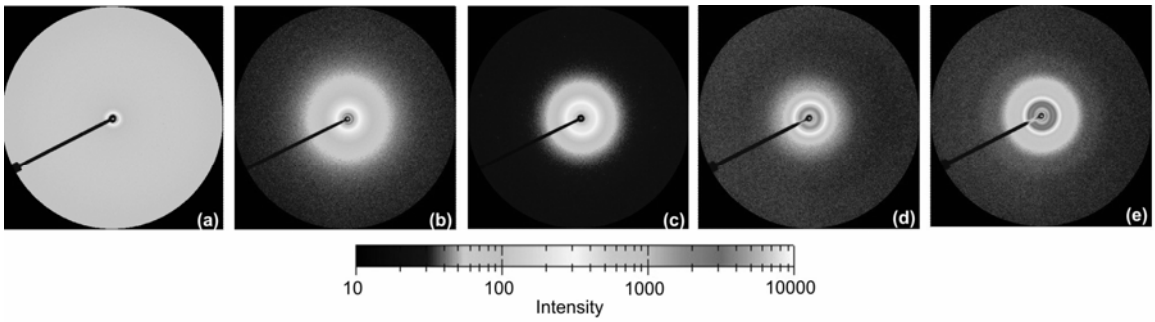

Figure II.5 – SAXS pattern of: (a) PU530, (b) PU1250, (c) PU2000, (d) PU10000&530 and (e) PU10000

Figure II.6(a) illustrates SAXS data of the obtained PUs in each the 2D pattern of each sample was integrated as a function of the angle of orientation of the sample in respect to the beam. The scattering peak observed in SAXS data of PU2000, PU10000&530 and PU10000 arises due to local heterogeneities in the electron density of the materials and it is usually interpreted as a consequence of the presence of distinct microphases with different electronic densities. However, in discussing the phase separation, it is

convenient to employ the Lorentz correction, Q_{inv}, which describes the electron density fluctuation of polymer and is a good approximation to estimate the overall degree of phase separation in segmented polymers, Figure II.6(b) [5, 6, 14]. The Lorentz correction, the invariant quantity, Q_{inv}, can be obtained by integrating $I_{(q)}q^2$ over the range of scattering angles, Equation II.7 [5, 6, 14].

$$Q_{inv} = \int_0^\infty I_{(q)} q^2 dq \tag{II.7}$$

where $I_{(q)}$ is X-ray scattering intensity and q the scattering vector.

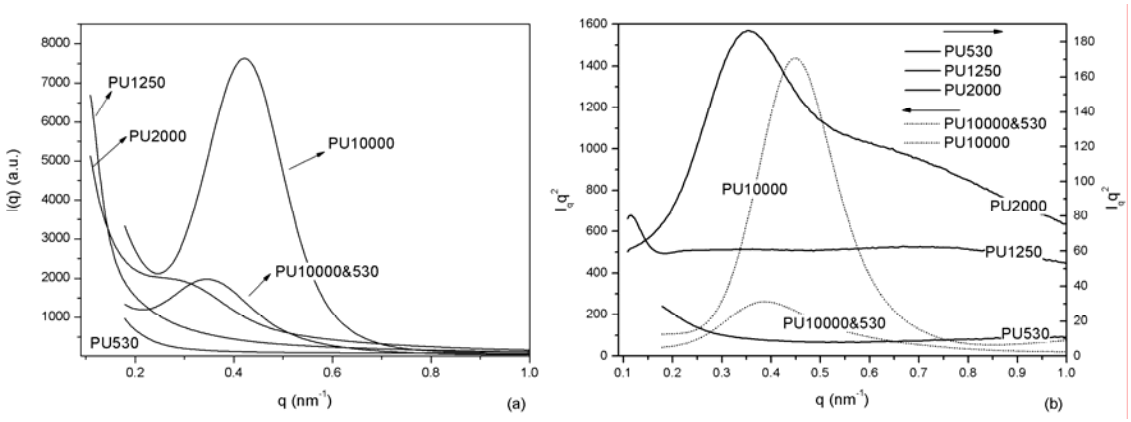

Figure II.6 – (a) SAXS curves of obtained PUs and (b) Deconvoluted Lorentz SAXS pattern of samples.

In Figure II.6(b) PU530 profile decreases monotonically with q, implying a high degree of phase mixture and no crystallinity. The system can be thought of as one phase structure. PU1250, PU2000, PU10000&530 and PU10000 present a multiphase structure including: amorphous matrix, hard domains and crystals. The contribution of each phase to the Lorentz corrected SAXS patterns were separated by a deconvolution procedure, Figure II.7.

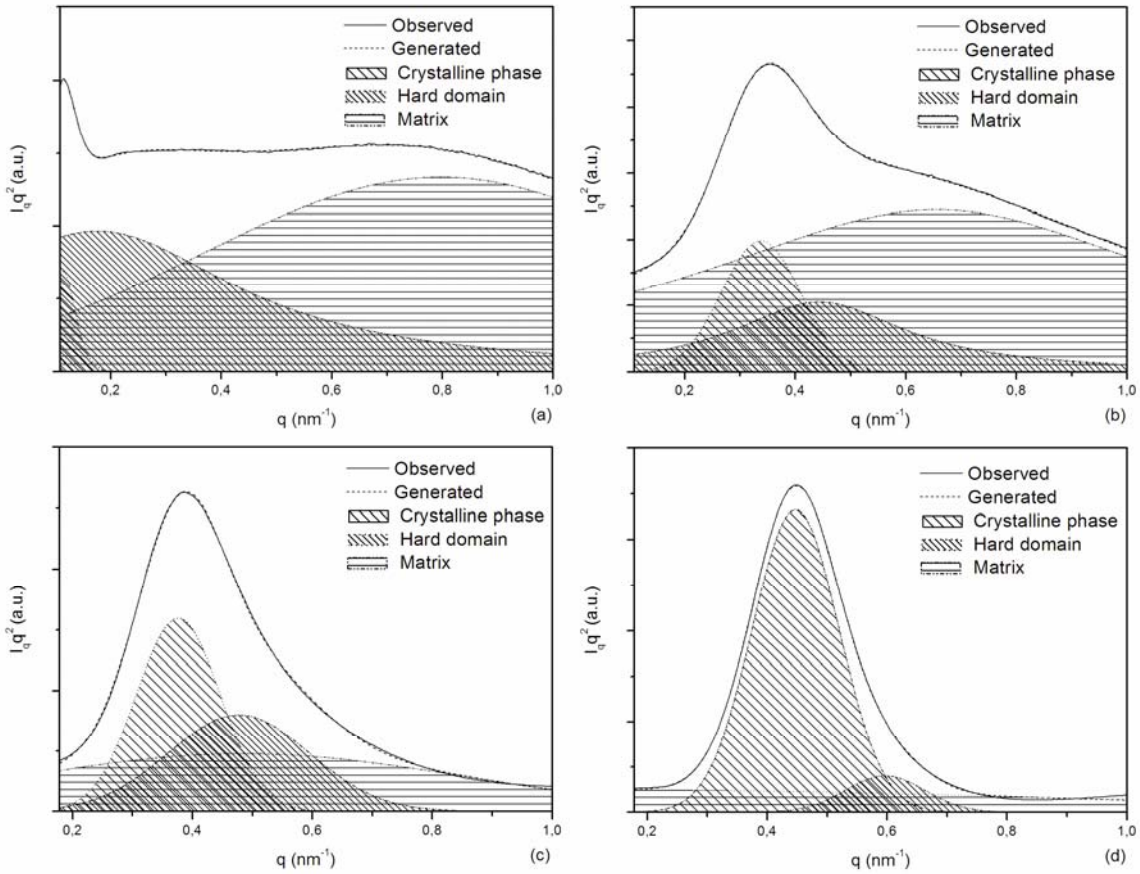

Figure II.7 – Deconvoluted Lorentz SAXS patterns: (a) PU1250, (b) PU2000, (c) PU10000&530 and (d) PU10000.

Q_{inv} of each phase was obtained as a fraction of the total area. The morphology of the polymer was investigated through the inter-domain repeat distance, L_{domain}, and/or lamellar crystalline repeat distance, $L_{Crystal}$. L is estimated from the $q_{\max}$ corresponding to the maximum of $I_{(q)}q^2$ versus q curves using Bragg's equation, Equation II.8 [5, 6, 14]. Table II.4 summarizes the results.

$$L = \frac{2\pi}{q_{\max}} \tag{II.8}$$

Since Q_{inv} is obtained by integrating $I_{(q)}q^2$ over the range of scattering angles, phases with higher electron densities like crystals achieve higher integrated values. As indicated by α_{FTIR} and SAXS's crystalline phase, PU10000&530 is more crystalline

than PU2000, hence one should expected higher integrated values for PU10000&530 than PU2000. However, this is not observed, possibly because the presence of PCL530 in soft segments of PU10000&530 would restrict chain packing efficiency, resulting in the formation of a less perfectly packed crystal structure.

Table II.4 – Deconvoluted SAXS results of crystalline phase, hard domains and matrix.

	Q_{inv}	Q_{inv} (%)			L (nm)	
		Crystalline phase	Hard Domain	Matrix	$L_{Crystal}$	L_{domain}
PU530	8.72	–	–	100.00	–	–
PU1250	54.48	1.72	31.48	66.80	55.30	35.97
PU2000	104.95	13.53	17.50	68.96	18.57	14.17
PU10000&530	82.83	33.70	28.25	38.05	16.69	13.17
PU10000	334.85	72.37	7.93	19.70	14.04	10.53

SAXS and FTIR results show a good correlation. Q_{inv} describes the overall degree of phase separation or $100 - DPM(\%)$ (Figure II.8-a), SAXS's crystalline phase is reflected to α_{FTIR}, (Figure II.8-b).

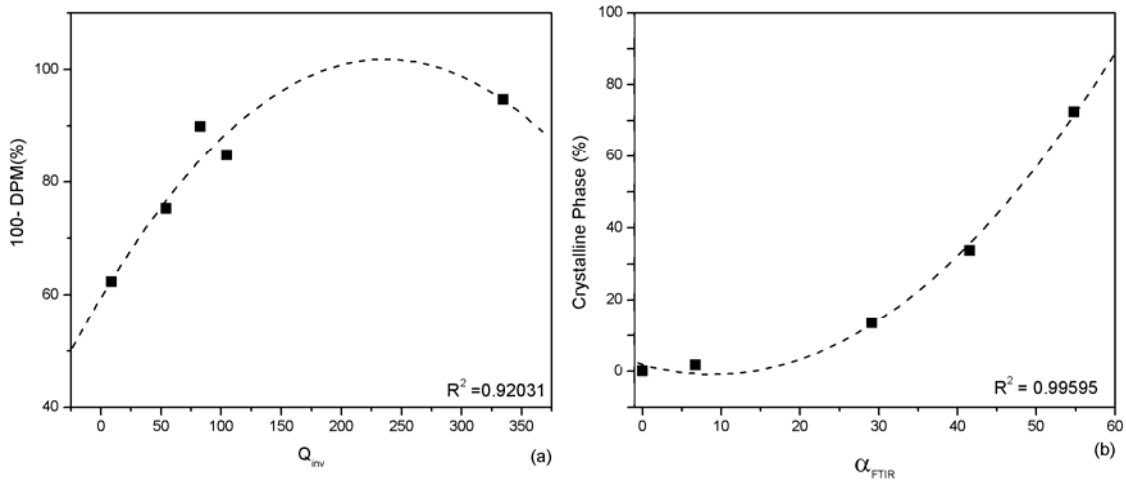

Figure II.8 – Correlation between SAXS and FTIR results.

The $W(HS)$ influence on the microphase separation structure of PUs is illustrated in Figure II.9. High segment contents promote phase mixture and decrease the chain mobility. Thus the soft segments are not able to align themselves to form crystals.
Results in Table II.4 shows that the amount of hard domains tend to decrease for samples having lower weight fractions of the hard segment as it is also observed by the $DPM(\%)$ values in Table II.2.

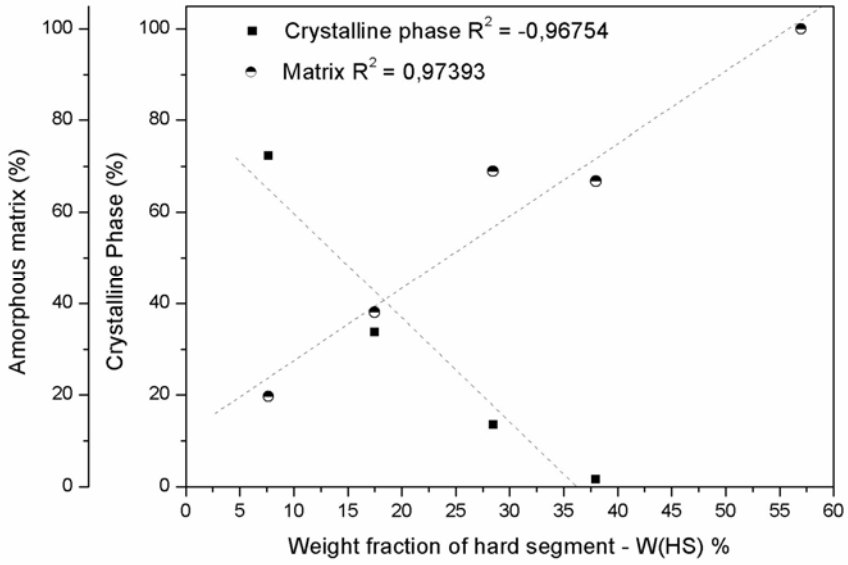

Figure II.9 – Influence of hard segment content and $HBI_{(C=O)}^{(\%)}$ on the multiphase structure of polyurethane.

II.4 – Conclusions

Polyurethane with multiphase structure including: amorphous matrix, hard domains and crystals were produced by altering the hard segment content. High segment contents promote phase mixture and decrease the chain mobility. Thus the soft segments are not able to align themselves to form crystals. SAXS results may be used to estimate the nano-morphology of segmented PUs.

II.5 – Acknowledgments

The authors acknowledge the financial support from the following institutions: National Council for Scientific and Technological Development (CNPq), a foundation linked to

the Ministry of Science and Technology (MCT) of the Brazilian Government; the State of Minas Gerais Research Foundation (FAPEMIG); and the National Synchrotron Light Laboratory (LNLS-Brazil) for the use of the SAXS beamline facilities.

II.6 – References

1 – Nakamae K, Nishino T, Asaoka S, et al. Int J Adhes Adhes 1999;19(5):345–51.

2 – Pompe G, Pohlers A, Pötschke P, Pionteck J. Polymer 1998;39(21):5147–53.

3 – Lin JR, Chen LW. J Appl Polym Sci 1998;69(8):1563–74.

4 – Li YJ, Gao T, Liu J, et al. Macromolecules 1992;25(26):7365–72.

5 – Wang SH, Zhang Y, Ren WT, et al. Polymer Testing 2005;24(6):766–74.

6 – Chang SL, Yu TL, Huang CC, et al. Polymer 1998;39(15):3479–89.

7 – Pereira IM, Carvalho S, Pereira MM, Leite MF, Oréfice RL J Appl Polym Sci 2009; Published Online: Jun 2 2009 DOI: 10.1002/app.30404

8 – Cheong IW, Kong HC, An JH, Kim JH. J Polym Sci A 2004;42:4353–69.

9 – Liu Y, Pan C. Eur Polym J 1998;34(5-6):621–4.

10 – Cho JW, Lee SH. Eur Polym J 2004;40(7):1343–8.

11 – Ayres E, Oréfice RL, Yoshida, MI. Eur Polym J 2007;43(8):3510–21.

12 – Nakamae K, Nishino T, Asaoka S, et al. Int J Adhes Adhes 1999;19(5):345–51.

13 – Bao H, Zhang Z, Ying S. Polymer 1996;37(13):2751–4.

14 – Li YJ, Kang WX, Stoffer JO, et al. Macromolecules 1994;27(2):612–4.

Chapter III (Capítulo III)

Proliferation of human mesenchymal stem cells derived from adipose tissue on polyurethanes with tunable biodegradability

I. M. Pereira[a, b]; V. S. Gomide[b]; A. A. C. Zonari[c], R. L. Oréfice[b*]; M. F. Leite[c], A. M. Goes[d]

[a]Federal Center of Technological Education of Minas Gerais, Av. Amazonas, 1193, Timóteo, MG, 35183-006, Brazil
[b]Federal University of Minas Gerais, Department of Metallurgical and Materials Engineering, Belo Horizonte, Minas Gerais, Brazil
[c]Federal University of Minas Gerais, Department of Physiology and Biophysics, ICB/UFMG, Belo Horizonte, Minas Gerais, Brazil
[d]Federal University of Minas Gerais, Department of Biochemistry and Immunology, ICB/UFMG, Belo Horizonte, Minas Gerais, Brazil

Abstract

Biodegradable polyurethanes (PUs) have been considered good candidates to be used in biomedical temporary devices that require mechanical properties comparable to soft tissues. However, toxicity of some biodegradable PUs is still a concern, since these polyurethanes can contain potential toxic components and residual organic solvents derived from their synthesis. In this work, in vitro tests to measure viability and proliferation of human mesenchymal stem cells (hMSCs) in contact with biodegradable polyurethanes were performed by employing MTT, alkaline phosphatase and collagen secretion assays. PUs were produced in an aqueous environment by employing isophorone diisocyanate/hydrazine (hard segment) and poly(caprolactone diol)/2,2-bis (hydroxymethyl) propionic acid (soft segment) as the main reagents. Three series of PUs having different soft segment contents were synthesized. These PUs had their chemical structure, morphology and hydrolytic degradation investigated. The rate of hydrolysis of the obtained PUs was tailored by modifying the soft segment content of the polymers. In vitro results showed that biodegradable PUs can provide a satisfactory environment for the adhesion and proliferation of hMSCs.

Keywords: Polyurethane, articular cartilage, biodegradation, in-vitro degradation, mesenchymal stem cells

III.1 – Introduction

Normal pain-free movement depends on the unique properties of the articular cartilage that forms the bearing surface of synovial joints. However, articular cartilage has a poor intrinsic capacity for repair. Even a small defect caused by mechanical damage will fail to heal and degenerate over time progressing to the debilitating condition of osteoarthritis [1, 2]. Currently, at an experimental stage, the strategies of tissue engineering are been investigated for the repair of articular cartilage defects.

Tissue engineering is a cross disciplinary field that combines biochemistry, cells, biomedical engineering and materials science to improve or replace biological functions. In the first step of one of the tissue engineering approach, cells are seeded in vitro on bioresorbable scaffolds in a bioreactor to construct a new tissue which will be implanted in vivo to recover the normal tissue function [3]. As the scaffolds play an important role in the formation of new articular surfaces, they should stabilize the growth factors and/or cells in the defect. Moreover, ideal scaffolds are designed to be biocompatible and bioabsorbable. Because the cartilage surface is responsible to dampen and to distribute loads within the cartilage and to the sub chondral bone during a large number of cycles, to increase the chances that the reparative process will be successful, the designed scaffold should match mechanical characteristics of the articular cartilage as compression strength, resilience, and durability [1, 2, 4, 5]. Nowadays, a variety of materials, including biodegradable PUs are been investigated as potential candidates for restoration of an articular surface. PUs are one of the most important families of polymers. A typical PU may contain, in addition to the urethane linkages, aliphatic and aromatic hydrocarbons, esters, ethers, amides, urea, and isocyanurates groups [6]. PUs are known to have special properties such as (1) easy preparation method, (2) high resistance to solvents, (3) long-term stability against exposure to sunlight and (4) consistent elastic properties [7, 8]. Among all the types of polyurethanes available, biodegradable PUs have received considerable attention in the past two decades [9], since they can be suitable candidates to participate in biomedical applications such as: insulators for cardiac pacing leads, blood bags, intra-aortic balloons, ventricular assist devices, vascular prostheses, catheters, surgical drapes,

breast implant coatings, skin wound dressings, gastric balloons, and tissue adhesives [9]. However, biodegradable PUs are still considered potentially toxic for the body, since they are usually produced using aromatic diisocyanates and organic toxic solvents [10].

Transplantation of human mesenchymal stem cells (hMSCs) that are capable of differentiation into cells of the chondrogenic lineage has opened new potential therapeutic approaches for the repair of articular cartilage defects [11]. MSCs are multipotent stem cells that have the ability to self-renew and intrinsically repair and regenerate damaged tissues. In addition, MSCs have the capacity to differentiate into a variety of other connective tissues such cartilage, bone, tendon, adipose tissue and muscle [1]. The multilineage potential of MSCs from the bone marrow stroma has been characterized extensively. However, the clinical use of MSCs has presented problems, including pain, morbidity, and low cell number upon harvest. Additionally, challenges including cell sourcing, sterilization, safety, storage, shipping, quality control, and scale-up has led many researchers to investigate alternative sources for MSCs. The use of human adipose derived adult stem (hADAS) cells represents a feasible approach to many of these issues [11, 12].

In this work, biodegradable PUs for cartilage tissue engineering were synthesized using water as main component for the reaction environment. The obtained waterborne PUs had their biodegradable behavior and morphology studied and were tested in vitro to check the degree of toxicity of the materials when exposed to hMSCs derived from adipose tissue.

III.2 – Materials and Methods

A – Prepolymer synthesis

Poly(caprolactone diol) (PCL – Mn = 1250, 2000 g mol^{-1}), isophorone diisocyanate (IPDI), 2,2-bis(hydroxymethyl), propionic acid (DMPA) and dibutyl tin dilaurate (DBDLT) were obtained from Aldrich (St. Louis, MO). Triethylamine (TEA, 98%) and

hydrazine (HZ, 25%) were purchased from Vetec (RJ, Brazil). All these chemicals were employed throughout this work without any previous treatment.

PUs were prepared by the prepolymer mixing method, using a 250mL three neck glass flask equipped with a heating mantel, a mechanical stirrer, a thermometer, under nitrogen atmosphere. The PCL and DMPA were stirred in the glass reactor at 60ºC for 30min. IPDI was added to the reactor in the presence of DBDLT (NCO/OH ratio of 2) under N_2 atmosphere. The reaction was carried out at 70–75ºC for 3hs. After cooling the prepolymer down to 40ºC, the carboxylic acid groups were neutralized by the addition of TEA. The mixture was then gentle stirred for 40min. The dispersion in water and PU chain extension were obtained by adding HZ and deionized water to the neutralized prepolymer under high-speed stirring. To ensure that the reaction was completed, the mixture was stirred for 30min. This chemical procedure was successful in producing PUs water dispersions with solid content about 30% (PUs). The feed ratios are shown in Table III.1, where $W(SS)$ is weight fraction of soft segment content, obtained according to Equation III.1.

$$W(SS)(\%) = \frac{Weight_{PCL} + Weight_{DMPA}}{Weight_{PU}} \times 100 \qquad \text{(III.1)}$$

Table III.1 – Composition (wt.%) of waterborne PUs

	W(SS)	PCL 1250	PCL 2000	DMPA	IPDI	HZ	TEA	H_2O	DBDLT
PU-A	62	20.12	–	1.63	12.55	0.77	1.23	63.70	0.34
PU-B	67	8.57	13.72	1.38	10.69	0.77	1.05	63.82	0.34
PU-C	72	–	23.92	1.21	9.32	0.67	0.91	63.97	0.34

B – Hydrolytic degradation tests

Hydrolytic degradation tests were carried out by weighing dried samples having 10mm in diameter and 1mm thick and immersing them in two different media: pH 7.4 phosphate buffered solution (PBS) and NaOH 3wt% aqueous solution. The samples

were removed from the media at predetermined time intervals, rinsed three times with distilled water, and immersed in distilled water for 1 hour. This last step aimed to remove the ions absorbed by the polymers. The specimens were then dried to a constant weight at 37ºC for 1 week and weighed again to determine the weight loss. The weight loss of the polymer films after hydrolysis was evaluated as the residual weight (%), which was defined by the Equation III.2 (the average of three measurements was used in the calculations):

$$Residual\ \ Weight\,(\%) = 100 - \left(\frac{w_0 - w_t}{w_0} \times 100 \right) \qquad \text{(III.2)}$$

where w_o and w_t were the initial weight and the weight at time t, respectively.

C – Infrared spectroscopy (FTIR)

Infrared spectra of PUs before and after hydrolytic degradation were collected in a FTIR, Perkin–Elmer, model Spectrum 1000 spectrophotometer. Measurements were carried out using the attenuated total reflectance (ATR) technique. FTIR spectras of PUs were obtained before and after hydrolytic degradation.

D – Wide angle X-ray scattering (WAXS)

Wide angle X-ray scattering (WAXS) analysis was performed by using a Philips, model PW1710 diffractometer operated with CuKα irradiation at a scan rate of 2º 2θ/s in the range of 5 to 60º. WAXS profiles of PUs were obtained before and after hydrolytic degradation.

E – Scanning electron microscopy (SEM)

A JEOL, model JSM-5410 field emission scanning electron microscope was used to observe the surfaces of the samples.

F – Cell origin, isolation, and culturing of adipose tissue-derived stem cell

Human adipose tissue was obtained with informed consent from healthy patients who had liposuction surgery for esthetic reasons in the "Núcleo de cirurgia plástica" (*Center of Plastic surgery*) - Belo Horizonte, Minas Gerais, Brazil. This project was approved by the Ethics Committee of Federal University of Minas Gerais. No diabetes, hepatitis, metabolic diseases, or other systemic complications were reported for these donors. Isolation and culturing of adipose tissue-derived stem cell (hADSC) was performed as described by Zuk et al (11). To isolate hADSC, adipose tissues were washed with phosphate-buffered saline (PBS), and the extracellular matrix was digested with 0.075% type I collagenase for 2 hours to release the cellular fractions tissues and then centrifuged at 1,200 x g for 10 min to obtain a pellet. The pellet was incubated for 2 days at 37°C/5% CO_2 in control medium (DMEM supplemented with 10% FBS, 100U/mL penicillin, and 100 µg/mL streptomycin). Following incubation, the tissue culture plates were washed to remove residual nonadherent cells and maintained at 37°C 15% CO2 in control medium. The stromal cells were then cultured for 7 to 10 days until they reached confluence. The cells were then harvested by digestion with 0.5 mmol/L EDTA/0.05% trypsin, centrifuged at 1200 rpm/min for 5 minutes, suspended in DMEM supplemented with 10% FBS, 100 U/ml penicillin, 100 µg/ml streptomycin, and plated at a density of approximately 2×10^4 cells/cm^2. Cells were cultured to confluence before a second harvesting and replating procedure as described above. The final hADSCs used were taken at 4^{th} passage.

G – Cellular Viability

For the cell culture studies, 2 mm x 3 mm x 1 mm films were cut and sterilized in UV light for 60 min. These PU samples were then gently deposited over the cell culture. After 72 h of incubation, hADSC viability was evaluated by MTT assay, based on the reduction of tetrazolium salt to formazan crystals by dehydrogenase present in living cells mitochondria. We left 200 µl of culture medium in each well and added 60 µl of stock solution of MTT (5 mg/ml). Two hours later, the cell morphology was analyzed by inverted optical microscopy and formazan salts were solubilized with 200 µl of SDS

10% HCl. After incubation, for 18 h, in a controlled 5% CO_2 95% humidified incubator at 37ºC, the optical density measurement was done at 595 nm [13].

H – Alkaline phosphatase activity

Alkaline phosphatase production was evaluated by BCIP-NBT assay. This assay is based on a chromagenic reaction initiated by the cleavage of the phosphate group of BCIP by alkaline phosphatase present in the cells. This reaction produces a proton, which reduces NBT to an insoluble purple precipitate. Briefly, the supernatant of each well was removed and the cell layer was rinsed twice with PBS. Then, 200μl of BCIPNBT solution, prepared as manufacturer's protocol, was added to each well. After 2 h of incubation, the cells were observed by optical microscopy and the insoluble purple precipitates were solubilized with 210 μl of SDS 10% HCl and incubated for 18 h. The optical density measurement was done at 595 nm. We used cultures without samples as control.

I – Collagen secretion measurement

Collagen production was analyzed by SIRCOL assay in supernatants of the cells cultures. This method is based on the selective binding property of the syrius-red dye to the [Gly-X-Y] tripeptide end sequence of mammalian collagen. The collagen present in the supernatant, precipitated by the dye, was solubilized and measured by an optical density analysis at 595 nm. The amount of collagen was calculated based on a standard curve of previously known concentrations of type I collagen and their optical density measurement [14]. As control, we used cultures without samples.

III.3 – Results and Discussion

A – Hydrolytic and alkaline degradation tests

The hydrolysis of PUs in phosphate-buffered saline solution at 37ºC was studied by monitoring the changes in mass of the samples during the tests. Figure III.1(a) shows the results of the hydrolytic degradation of the samples and indicate that the crystalline

fraction (WAXS results will be discussed later) of the materials strongly influenced the degradation rate. Although having lower contents of soft hydrolysable segments, PU-A displayed higher rates of hydrolysis, mainly because of its amorphous structure that is highly assessable to water. On the other hand, PU-B and PU-C have a partially crystalline structure that restricts the penetration of water molecules towards breaking ester sites. Other possible explanation includes a decrease in hydrophilicity for polyurethanes having higher contents of more hydrophobic soft segments. Figure III.1(b) shows the hydrolysis of the samples performed in an alkaline environment. The degradation process of polyurethane in alkaline solution is based on the hydrolytic attack of ester bonds [15]. In this high-pH solution, the PCL crystallites are also promptly hydrolyzed and higher rates of hydrolysis (loss of mass) were observed for samples with higher soft segment contents (PU-B and PU-C).

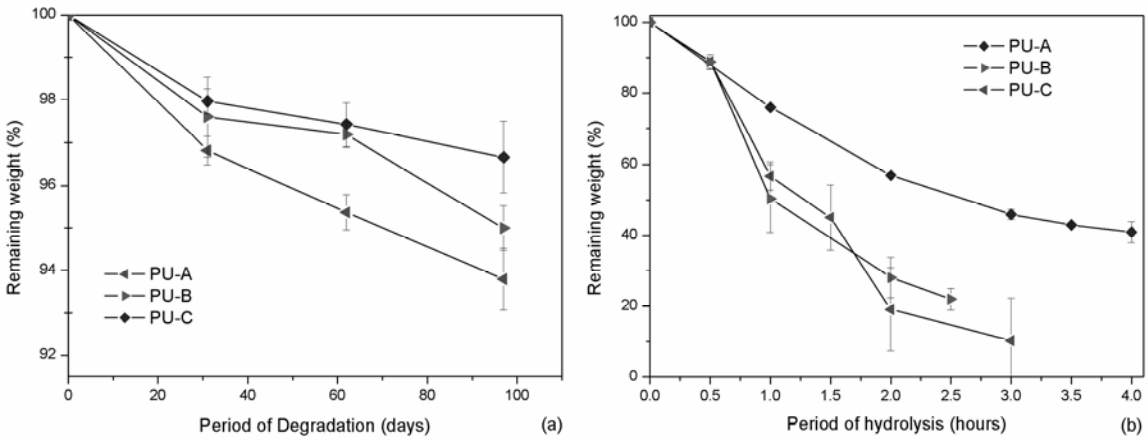

Figure III.1 – Mass changes of polyurethanes upon degradation in: (a) PBS solution and (b) NaOH solution.

B – Infrared spectroscopy (FTIR)

Typical infrared spectra of PU–A, PU–B and PU–C are shown in Figure III.2 where the characteristic IR absorption bands of poly(ester-urethane) are marked.

The primary amine stretching modes appear at 3600–3150 cm^{-1}. The absorption band at about ~3300 cm^{-1} corresponds to hydrogen bonded –N–H group and absorption at ~3500 cm^{-1} to nonbonded –N–H. The carbonyl group stretching vibrations, C=O, appear

at 1760–1600 cm^{-1}. A series of specific absorption bands are present within the 1760–1600 cm^{-1} broad band, such as the absorption band due to the ester bond from PCL soft segments and others associated with multiple interactions between urea and urethane bonds and –N–H groups. IR bands at ~1720 cm^{-1}, ~1700 cm^{-1}, ~1660 cm^{-1}, ~1630 cm^{-1} are assigned, respectively, to free urethane stretching band, hydrogen bonded urethane stretching band, free urea stretching band, hydrogen bonded urea stretching band. The secondary amide absorption, >N–H, appears at 1640–1540 cm^{-1}. The band at 1150 cm^{-1} is assigned to the stretching of the –C–O–C– group [15, 16, 17, 18, 19].

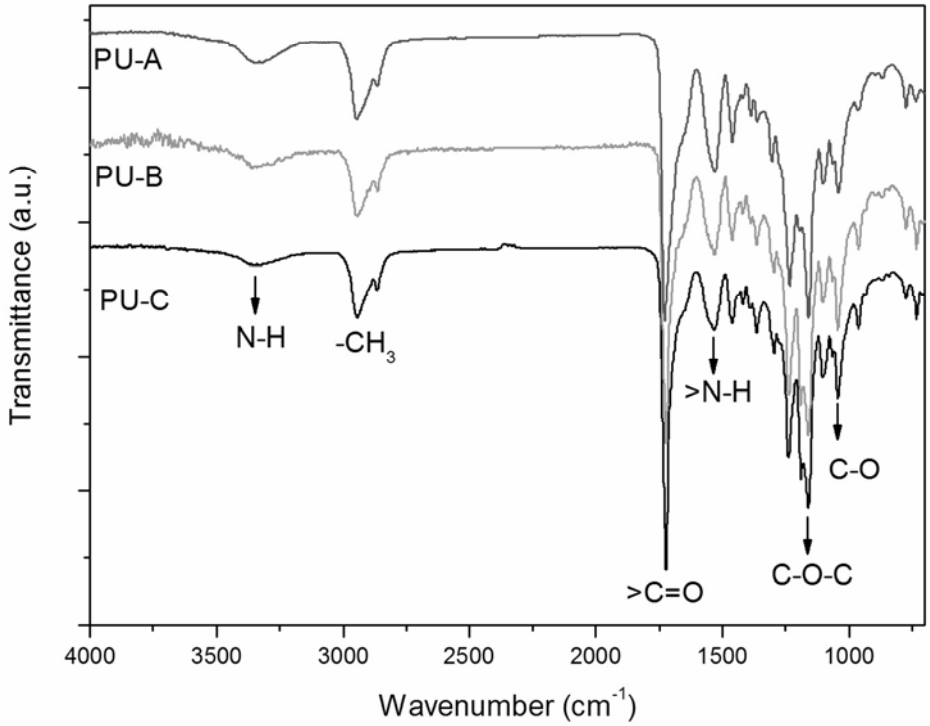

Figure III.2 – FTIR spectra of PU–A, PU–B and PU–C.

FTIR spectra of PU-B after hydrolysis performed at 37ºC in PBS are presented in Figure III.3. The infrared spectra were normalized to the 1045 cm^{-1} band assigned to O–C [20]

Spectrum of the PU-B specimen after 97 days of incubation showed that peak intensities of bands at: 1295 cm^{-1} (υC–N + δN–H, amide III) , 1190 cm^{-1}(C–O–C of C(O)–O, ester, crystalline) [20] and 934 cm^{-1} (δN–H) increased compared with the original sample. On

the other hand, the peak intensities of band 1160 cm^{-1}(υC–O–C, amorphous) [21] decreased. The enhancement in peak intensity of the ester band may indicate that the crystalline fraction increased during degradation.

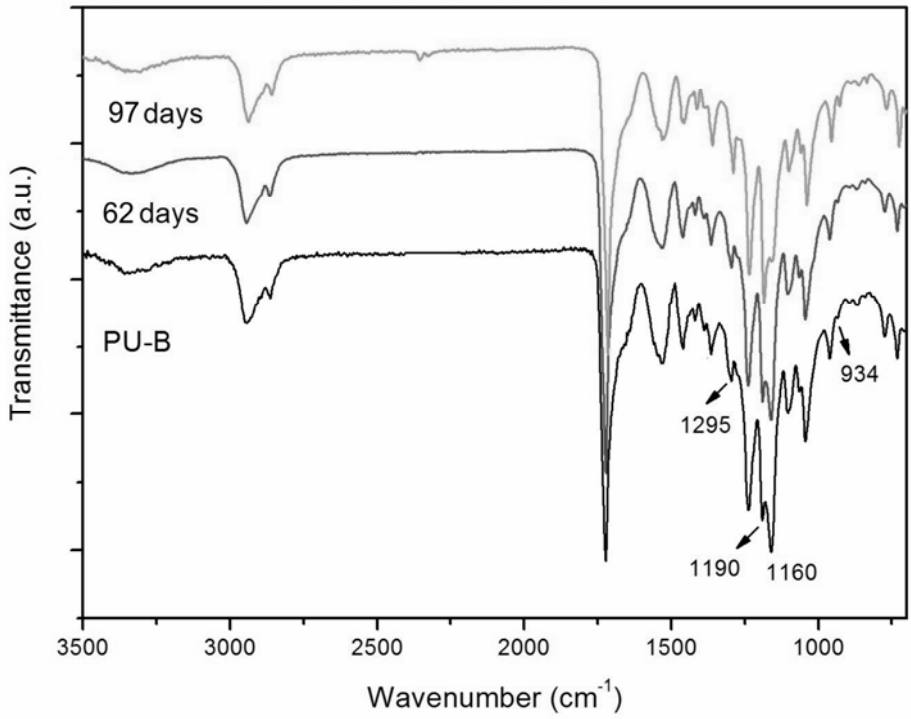

Figure III.3 – FTIR spectra of PU-B after hydrolysis performed at 37ºC in PBS for 62 and 97 days.

The FTIR spectra in Figure III.3 shows that the cleavage of urethane bonds takes place by: (i) the reduction in intensity of the >N–H band, (ii) the increase in the intensity –N–H band [22].

The carbonyl region usually has been investigated for the quantitative study of microphase separation or mixing in PU. The extent of the carbonyl absorption groups participating in hydrogen bonding could be expressed by a hydrogen-bonding index $HBI(\%)$, which is the fraction of hydrogen bonded in the carbonyl groups stretching vibrations Equation III.3 [9,10,15]. Since band overlapping is observed, a deconvolution mathematical procedure (using the PickFiT® software) was performed on spectra of Figure 1 to enhance resolution of carbonly.

$$HBI(\%) = \frac{A_{1700} + A_{1640}}{A_{1700} + A_{1640} + A_{1724} + A_{1660}} \times 100 \qquad \text{(III.3)}$$

where A_{1724}, A_{1700}, A_{1660}, and A_{1640} are respectively the band peak area of free urethane, bonded urethane, free urea, bonded urea and ester.

$HBI(\%)$ of PU-A and PU-C were investigated before degradation. PU-B was investigated before and after hydrolysis for 62 and 97 days. Figure III.4 illustrates the deconvolution procedure used to determine the overlapped band of FTIR spectrum:

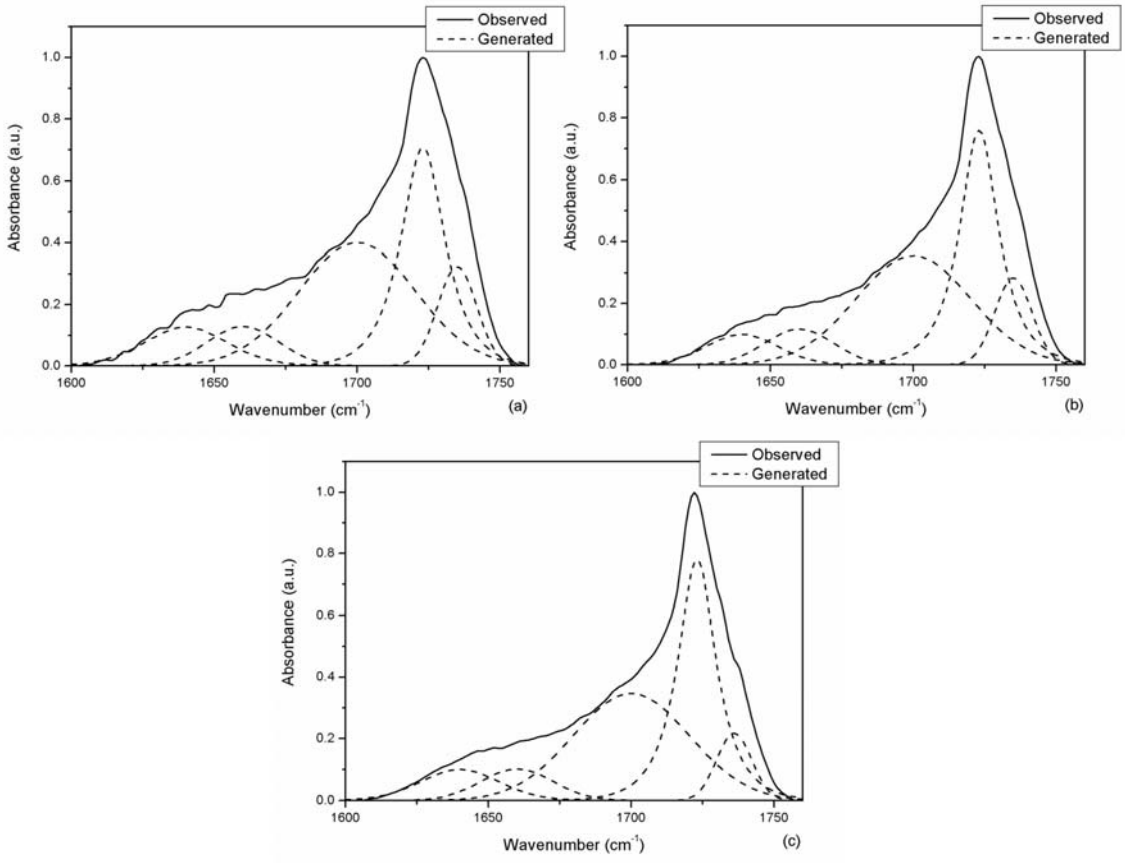

Figure III.4 – Band area development of PU-B during hydrolysis performed at 37ºC in PBS (a) PU-B, (b) after 62 days degradation and (c) after 97 days.

The values of HBI are shown in Figure III.5 and indicate that the degradation process and also the annealing process that occurred at 37ºC set conditions for the stabilization of a new phase separated morphology. Chain cleavage and annealing can alter mobility

and solubility and lead to higher contents of dissolved hard segments within the soft domains that would result in lower values of HBI.

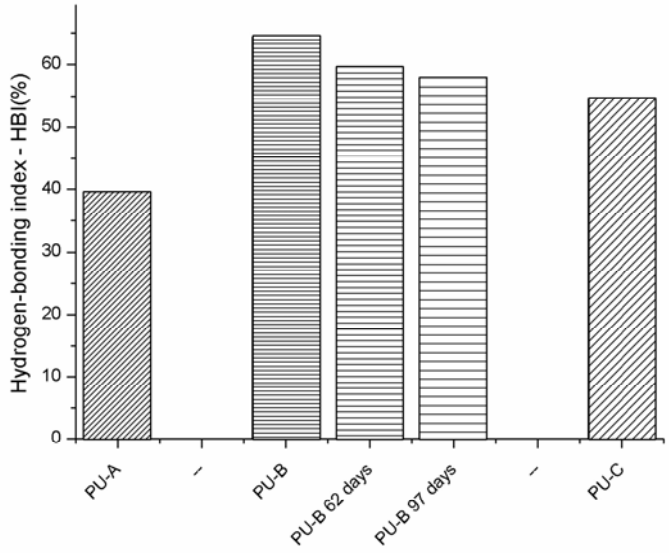

Figure III.5 – HBI(%) of obtained PUs and degraded samples.

C – Wide angle X-ray scattering (WAXS)

Figure III.6 shows the WAXS profiles of PUs. The diffraction curves of PU-A, PU-B and PU-C show broad shoulders around 2θ = 20º, which is typical of noncrystalline state with a characteristic short-scale order (interchain spacing) of 0.4–0.5nm [17].

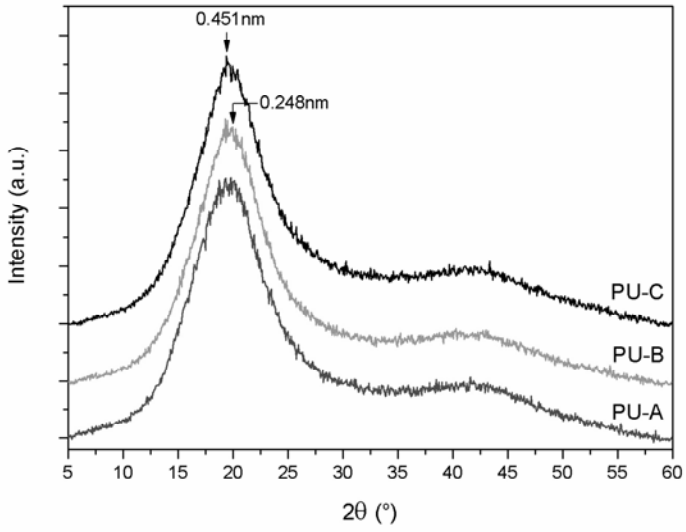

Figure III.6 – WAXS pattern of PU-A, PU-B and PU-C.

Low molar mass PCL oligomers present in PU-A are less effective in adopting conformations that would result in crystallization of soft segments. On the other hand, as the soft segment content and the soft segment chain length increase (PU-B and PU-C), soft segments begin to be able to arrange themselves in more organized structures. The presence of these crystallites is detected as small sharp peaks in the PU-B diffraction pattern that become more distinct at PU-C curve, indicating that the soft segments are long enough to crystallize.

WAXS profiles of PUs after hydrolysis 62 days performed at 37ºC in PBS are presented in Figure III.7. WAXS profiles of PUs are typical for semicrystalline polymers. Results indicated that the hydrogen-bonding structure of PUs is modified during the degradation process releasing the soft segments which allows them to crystallize. Moreover, the facilitated crystallization may be caused by the test temperature, which may relate closely to the annealing thermal condition.

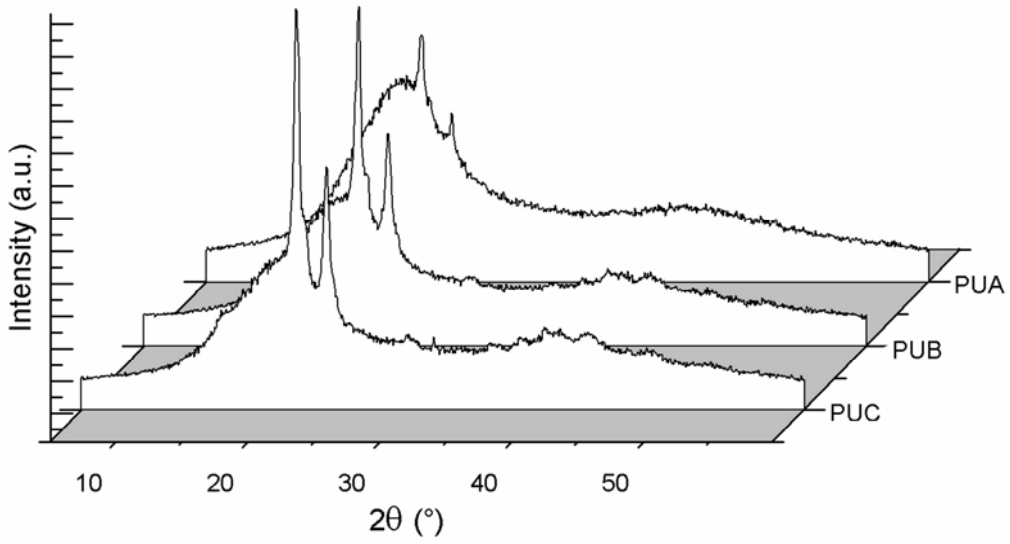

Figure III.7 – WAXS spectra of obtained PUs after 62 days hydrolysis performed at 37ºC in PBS.

To investigate the crystalline structure of degraded PUs, the amorphous and crystalline parts were separated by a deconvolution procedure using the PickFiT® software. Gaussian curves were used to describe the amorphous phase and all the crystalline

reflections, Figure III.8. The crystallinity index, α_X, was defined as the ratio of the area under the separate crystalline pattern ($\sum A_{crystalline}$) and the total scattering $\left(\sum A_{crystalline} + \sum A_{amourphous}\right)$of the original pattern, [23], Equation III.3.

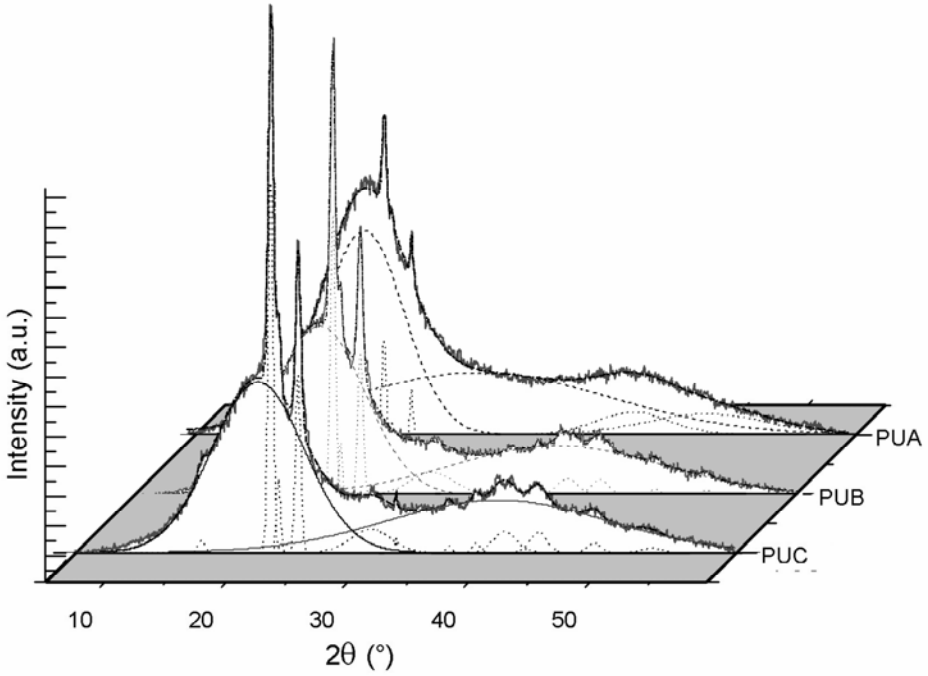

Figure III.8 – Peak deconvolution of the WAXS profiles: (a) PU-A, (b) PU-B and PU-C; after 62 days hydrolysis performed at 37ºC.

$$\alpha_X = \frac{\sum A_{crystalline}}{\left(\sum A_{crystalline} + \sum A_{amourphous}\right)} \times 100 \quad (3)$$

As expected, the crystalline portion of PU-C, after degradation, is larger than PU-A or PU-B. PU-C has longer soft segment chains and longer chains are more likely to crystallize; once the bonds are broken, the chains become free to move and to organize in crystals. Crystals work as barrier to water diffusion decreasing the degradation rate, therefore, the hydrolytic degradation of PU-C is the slowest one. As observed at Table III.2, the degradation kinetics of PU-B and PU-C are similar up to 62 days of degradation, afterwards, the degradation process of PU-B is accelerated compared to PU-C. Figure III.9 shows WAXS results of PU-B and PU-C after hydrolysis, 97 days, performed at 37ºC in PBS. The crystalline and amorphous portion of WAXS patterns

were obtained according to Equation III.3. Results indicate that the crystalline portion of PU-C increases during the degradation process while the crystalline portion of PU-B seems to stabilize, which might explain the slower degradation kinetics of PU-C. Results are summarized in Table III.2

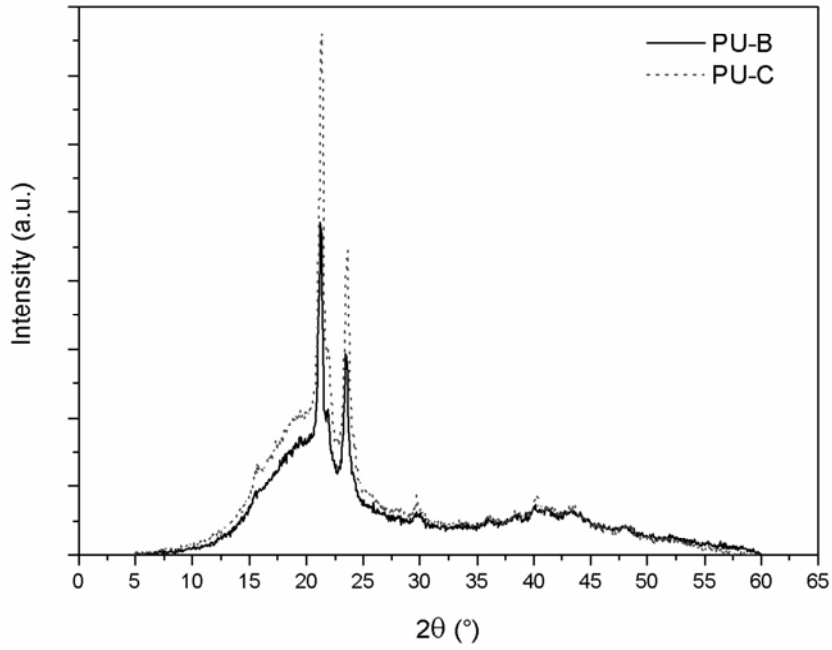

Figure III.9 – WAXS curves of PU-B and PU-C after 97 days hydrolysis performed at 37ºC in PBS.

Table III.2 - Crystallinity index after hydrolysis performed at 37ºC in PBS.

	62days	97 days
PU-A	12.61	NA
PU-B	13.98	13.32
PU-C	16.28	17.51

D – Scanning electron microscopy (SEM)

Figure III.10 shows the surface morphology and fracture surface of PU-B after hydrolysis performed at 37ºC in PBS for 62 and 97 days. As the degradation proceeded, the surface became rugged and eroded. The fracture surfaces show that the degradation occurs from the surface to the bulk of the material, i.e., surface limited erosion. The rate

of water diffusion through the sample should be lower than the rate of hydrolysis. The thickness of the damaged layer due to partial degradation can be used to monitor the evolution of the degradation process. In Figure III.10(b), for example, the thickness of the modified layer is ~26μm, while this value is increased to ~79μm after 97 days (Figure III.10-d).

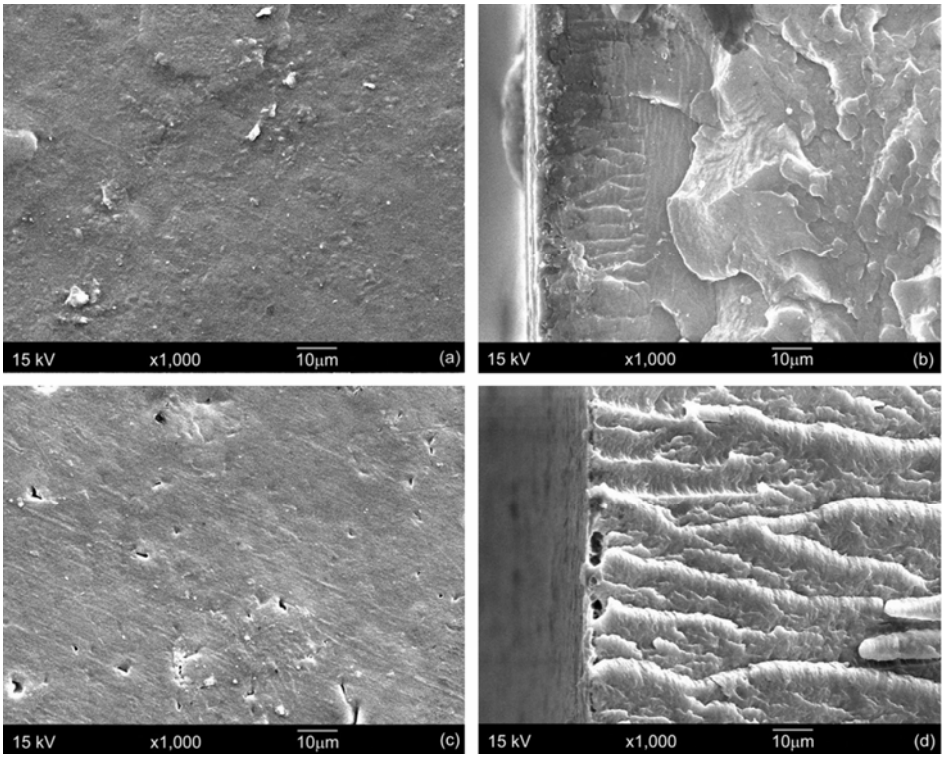

Figure III.10 – SEM images of PU-B sample degraded in PBS solution at 37ºC: (a) surface morphology after 62 days, (b) fracture surface after 62 days, (c) surface morphology after 97 days and (d) fracture surface after 97 days.

E – Cellular Viability

Cellular viability studies performed by using MTT assay are presented in Figure III.11. This method measures the cytotoxicity, proliferation or activation because it detects only living cells and the signal generated is dependent on the degree of activation of the cells [24]. The assay showed that the cells were able to keep their activity when in contact with the produced polyurethanes. When compared to control, the optical density measurements of the solubilized formazan crystals showed a small increase in cell viability in the presence of PU-A and a decrease in PU-C. It is possible that the

amorphous nature of PU-A and its slight higher hydrophobic characteristic can contribute to cell fixation and proliferation. The presence of PUs does not interfere significantly with collagen secretion. It was also observed that the alkaline phosphatase activity in the presence of the PU-A and PU-C was higher when compared with the control group, Figure III.11(a). Only normal cells can metabolize and be colored by BCIP-NBT as observed in the cells of the photomicrographs in Figure III.11(b).

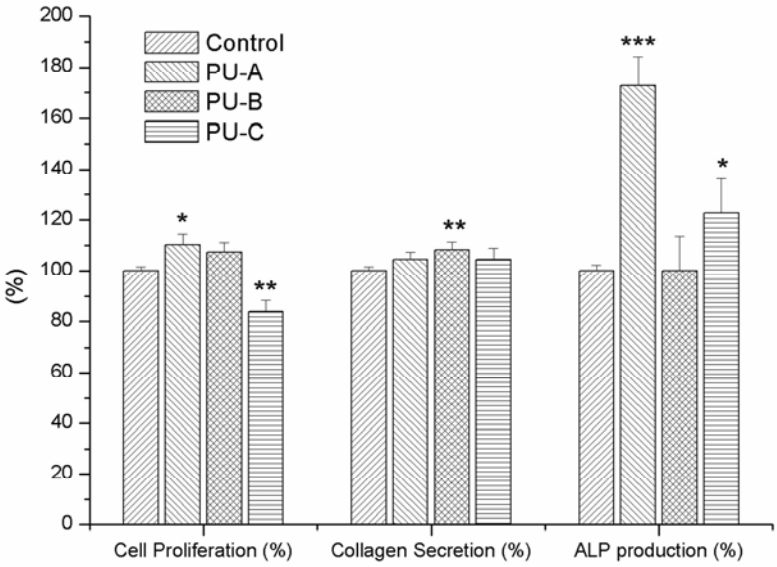

(a)

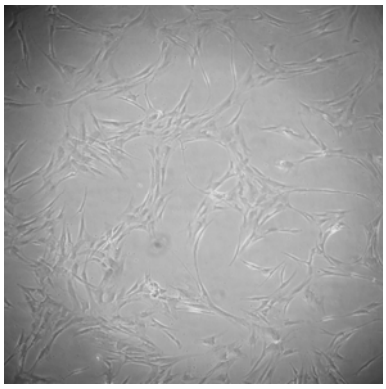

(b)

Figure III.11 – (a) Cellular viability evaluated by MTT assay, collagen secretion by SIRCOL assay and alkaline phosphatase production evaluated by NBT-BCIP assay. Results evaluated after 3 days of incubation. Results represent Mean ± SD of triplicates from 3 separate experiments. (*) indicates that there is a significant difference ($p < 0.05$). (b) Photomicrograph of hMSCs (150X) in contact with PU´s

The results suggest that the obtained PUs, particularly PU-A, support the viability and proliferation of hMSCs. MSCs are the natural precursor cells of cartilage tissue through chondrogenic differentiation into chondrocytes, which produce a cartilaginous matrix.

III.4 – Conclusion

Hydrolysable polyurethanes having different PCL based soft segment contents were successfully produced by using water instead of organic solvents as the reaction

environment. Soft segment content and the chain length were observed to affect the degree of hydrogen bonding and crystallinity. The obtained polyurethanes were hydrolysable in both PBS and alkaline solutions. The rate of hydrolysis was enhanced when alkaline conditions were used during the test. Moreover, the rate of hydrolysis was able to be tailored by altering the soft segment content of the polyurethanes. The obtained PUs are a promising material for cartilage repair, providing a good environment for the adhesion and proliferation of hMSCs.

III.5 – Acknowledgements

The authors acknowledge the financial support from the following institutions: National Council for Scientific and Technological Development (CNPq) and the State of Minas Gerais Research Foundation (FAPEMIG).

III.6 – References

1 – Redman,S. N.; S. Oldfield, F C; Archer, W. Current strategies for articular cartilage repair. European Cells and Materials v. 9, p. 23-32, 2005.

2 – Buckwalter,J. A Articular Cartilage: Injuries and Potential for Healing. Journal of Orthopaedics& sport Physical Therapy v. 28 n. 4 10/2008 192-202

3 – Ratner BD, Hoffmann AS, Schoen FJ, Lemons JE. Biomaterials science: an introduction to biomaterials in medicine. 2nd ed. Elsevier; 2004.

4 – Nöth, U.; Tuli, R.; Osyczka, A. M.; Danielson, K.; Tuan, R. S. In vitro Engineered Cartilage Constructs Produced by Press-Coating Biodegradable Polymer with Human Mesenchymal Stem Cells. Tissue Engineering, v. 8 n. 1 2002 131-144

5 – Martino, A. D.; Sittinger, M.; Risbud, M. V. Chitosan: A versatile biopolymer for orthopaedic tissue-engineering. Biomaterials 26 (2005) 5983–5990

6 - Szycher, M. Introduction. Szycher's Handbook of Polyurethanes. London: CRC Press, 1999. p. 1.1-1.6.

7 - Yang, J. H.; Chun, B. C.; Chung, Y. C., et al. Comparison of thermal/mechanical properties and shape memory effect of polyurethane block-copolymers with planar or bent shape of hard. Polymer, 44(11):3251-3258, 2003.

8 - Hong, J. H.; Jeon, H. J.; Yoo, J. H., et al. Synthesis and characterization of biodegradable poly(epsilon-caprolactone-co-beta-butyrolactone)-based polyurethane. Polymer Degradation and Stability, 92(7): 1186-1192, 2007.

9 - Feng, Y. K.; Li, C. Y. Study on oxidative degradation behaviors of polyesterurethane network. Polymer Degradation and Stability, 91(8): 1711-1716, 2006.

10 - Minnen, B V.; Leeuwen, M. B. M. V.; Stegenga, B, et al. Short-term in vitro and in vivo biocompatibility of a biodegradable polyurethane foam based on 1,4-butanediisocyanate. Journal of Materials Science-Materials in Medicine, 16(3): 221-227, 2005.

11 - Zuk, P. A.; Zhu, M. Ashjian, P.; Ugarte, D. A.; Huang, J. I.; Mizuno, H.; Alfonso, Z. C.; Fraser, J. K. Benhaim, P.; Hedrick, M. H. Human Adipose Tissue Is a Source of Multipotent Stem Cells. Molecular Biology of the Cell Vol. 13, 4279–4295, December 2002

12 - Awada, H. A.; Wickham, M. Q. Leddy, H. A.; Gimble, J. M.; Guilak, F. Chondrogenic differentiation of adipose-derived adult stem cells in agarose, alginate, and gelatin scaffolds Biomaterials 25 (2004) 3211–3222

13 – Amaral, M.; Costa, M. A.; ibid. 23 (2002) 4897.

14 – Reinert, H. T.; Jundt, G., Histochem. Cell. Biol. 112 (1999) 271.

15 - Ayres, E.; Oréfice, R. L.; Yoshida, M. I; Phase morphology of hydrolysable polyurethanes derived from aqueous dispersions. European Polymer Journal, 43(8): 3510–3521, 2007

16 – Chattopadhyay, D. K.; Sreedhar, B.; Raju, K. V. S. N. The phase mixing studies on moisture cured polyurethane-ureas during cure. Polymer, 47(11): 3814–3825, 2006.

17 – Kim B. K.; Lee S. Y.; Xu M. Polyurethanes having shape memory effects. Polymer, 37(26): 5781–5793, 1996.

18 - Marcos-Fernández, A.; Abraham G.A.; Valentín J.L.; San Román J. Synthesis and characterization of biodegradable non-toxic poly(ester-urethane-urea)s based on poly(ε-caprolactone) and amino acid derivatives. Polymer, 47(3): 785–798, 2006.

19 - Coates, J.P. A Practical Approach to the Interpretation of Infrared Spectra. Encyclopedia of Analytical Chemistry, Ed. R.A. Meyers, J. Wiley & Sons, Ltd.; Chichester, UK, p. 10815–10837, 2000.

20 – Feng Y. K.; Li C. Y. Study on oxidative degradation behaviors of polyesterurethane network. Polymer Degradation and Stability v. 91, n. 8, p. 1711-1716, 2006

21 – Dillon, J. Infrared Spectroscopy Atlas of Polyurethanes (Including Model Compounds). Technomic Publishing AG, Basle, ISBN 0-87762-615-4, 1989

22 – Chew M. Y. L.; Goh S. H.; Kang L. H.; et al. Applicability of infrared spectroscopy for sealant degradation studies. Building and Environment, v. 34, n, 1. p. 49-55, 1999.

23 – Pompe G.; Pohlers A.; Pötschke P.; Pionteck J. Influence of processing conditions on the multiphase structure of segmented polyurethane. Polymer v. 39, n. 21, p. 5174–5153, 1998.

24 – Mosmann, T. Rapid Colorimetric Assay for Cellular Growth and Survival: Application to Proliferation and Cytotoxicity Assays Journal oflmmunologicalMethods, 65 (1983) 55-63

Chapter IV (Capítulo IV)

Effect of the degree of clay delamination on the phase morphology, surface chemical aspects and properties of hydrolysable polyurethanes for periodontal regeneration

I. M. Pereira*(a); S. Carvalho(b); M. M. Pereira(b); M.F. Leite(c); R. L. Oréfice(b)

[a]Federal Center of Technological Education of Minas Gerais, Timoteo, Brazil
[b]Federal University of Minas Gerais, Department of Metallurgical and Materials Engineering, Belo Horizonte, Brazil
[c]Federal University of Minas Gerais, Department of Physiology and Biophysics, ICB/UFMG, Belo Horizonte, Minas Gerais, Brazil

Abstract:

In recent years, there has been increased interest in biodegradable polyurethane (PU) for use in regenerative medicine because of their versatility and biocompatibility. Nevertheless, these polymers are usually produced using organic solvents that can lead to the release of toxic components. In this work, polyurethane/montmorillonite nanocomposites were designed to work as guided tissue regeneration membranes to treat periodontal diseases. PUs were synthesized in an aqueous environment. The composition, the morphology, and mechanical properties of the biomaterials were evaluated. The cellular viability, proliferation, and morphology changes of rat culture cementoblasts were also investigated using a MTT assay. Small angle x-ray scattering (SAXS), x-ray diffraction (XRD) and infrared spectroscopy (FTIR) results showed that the degree of clay delamination within the polymer was able to tailor the phase morphology of the polymer, the chemical aspects of the surface, the mechanical properties and the kinetics of hydrolysis of the materials. The produced scaffolds provided a good environment for the adhesion and proliferation of cementoblasts and, thus, can be considered suitable biomaterials for participating in procedures associated with periodontal regeneration.

Keywords: Polyurethane, montmorillonite, tissue regeneration

IV.1 – Introduction

A family of polymers that contains urethane linkages is very often called polyurethanes (PUs). PUs can be designed and produced to yield thermoplastic elastomers that have segmented macromolecular architecture formed by hard (polar) and soft (nonpolar) segments. The properties of this type of material will, therefore, be strongly associated with the hard and soft segments: content, interaction and phase separation [1, 2]. Recently, montmorillonite / polyurethane nanocomposites (PU/MMT) have been studied in order to produce materials with improved properties that could extend the use of PU further [3]. To achieve high levels of properties in polymer nanocomposites, the dispersion and exfoliation of layered silicates within polymeric matrices are considered key steps. Since natural montmorillonite has poor affinity with hydrophobic polymers, cationic modified MMT has been widely used [3, 4] to improve interfacial interactions and exfoliation.

Segmented PUs have been extensively used in biomedical applications because of their biocompatibility; typical examples are catheters, skin wound dressings, tissue adhesives, etc [5]. Therefore, there has been increased interest in biodegradable PUs for use as tissue scaffolds and drug deliver systems. Designed to undergo to hydrolytic or enzymatic degradation, the tissue-engineered scaffolds are intended to be used in regenerative medicine, for instance, regeneration of cardiovascular, musculoskeletal and neurological tissues [6]. However, these PU´s are usually produced using organic solvents that can lead potentially to the release of carcinogenic components [7]. As a consequence, PUs synthesized in an aqueous environment (waterborne PUs) can be very useful in reducing the risk of toxic components derived from organic solvents.

In recent years, the tissue engineering strategies were associated with the concepts of guided tissue regeneration (GTR) to promote periodontal wound healing. GTR was first introduced in 1982 by Nyman et al [8]. Nowadays, it has become an essential part of clinical periodontics [9, 10] to treat periodontal disease which is characterized by inflammation and subsequent loss or damage of tooth supporting tissues, including cementum, bone and periodontal ligament. GTR clinical method involves exclusion of

epithelium and isolation of the root surface from gingival corium by a physical barrier in the form of a membrane. These barriers act as filter to prevent epithelial and connective tissue cell migration to facilitate regenerative potential cells to proliferate and migrate into the protected wound area [10]. A variety of synthetic and naturally derived GTR membranes have been used to facilitate periodontal tissue regeneration. Gore-Tex and TefGen, belong to the first generation of GTR membranes, which are characterized by being non-absorbable [8]. Barrier membranes must meet certain requirements such as: (i) tissue integration to promote wound stabilization; (ii) cell occlusivity to attract desirable cells such as periodontal ligament cells, bone cells, and cementoblasts, (iii) space-making and/or maintaining to allow new attachment formation, and (iv) biocompatibility to ensure material safety [9]. However, other factors such as adequate mechanical properties and biodegradation contribute to tissue regeneration. The mechanically dynamic environment in the mouth requires a material capable to resist to tribological movements occurring in the mouth and a material able to sustain and recover form after various deformations without irritations to the surrounding tissues. Moreover, the use of a biodegradable membrane would eliminate the necessity of second surgical procedure for the removal of the membrane and may thereby facilitate the clinical use of the GTR-strategy. For that reason, a second-generation of absorbable GTR membrane has rapidly gain interest [8].

The aim of the present study was to develop a soft, tough and elastomeric PU with potential application as GTR membrane. In this work, PUs were synthesized in an aqueous environment by combining hard segments derived from aliphatic isophorone diisocyanate and hydrazine with soft segments based on poly(caprolactone diol). PUs were also reinforced with Na^{+}/MMT. The composition, the morphology, and mechanical properties of the biomaterials were investigated. Cementoblasts were used in this study to evaluate the cellular response to PU/MMT membranes. Cementoblasts are cells adjacent to the dentine responsible for the cementogenesis. Cementogenesis is the creation of cementum, a hard mineralized tissue, which covers the roots of teeth and provides attachment of periodontal ligament to roots and surrounding alveolar bone. Cementum is essential for periodontal regeneration, as it provides anchorage between the root surface and periodontal ligament [11-17]. Therefore, biodegradable

biomaterials that can support the growth of cementoblasts are potential strong candidates to be used in the periodontal regeneration.

IV.2 – Materials and Methods

A – Polymer synthesis

Poly(caprolactone diol) (PCL M_n = 1250 g mol^{-1}), isophorone diisocyanate (IPDI), 2,2-bis(hydroxymethyl) propionic acid (DMPA) and dibutyl tin dilaurate (DBDLT) were obtained from Aldrich. Triethylamine (TEA, 98%) and hydrazine (HZ, 25%) were purchased from Vetec. All these chemicals were employed throughout this work without any previous treatment. Natural montmorillonite (MMT) (Cloisite® Na^+) were obtained from Southern Clay.

PUs were synthesized by the conventional prepolymer method, using a 250 mL three neck glass flask equipped with a heating mantel, a mechanical stirrer, a thermometer under nitrogen atmosphere. In the first step, prepolymer was obtained by reacting PCL (20.12 wt %), DMPA (1.63 wt %) and IPDI (12.55 wt %) at 2 NCO/OH ratio for about 3.5h. During this time, DBDLT was added twice. The reaction was carried out at 70–75ºC. After cooling down to 40ºC, the carboxylic acid groups were neutralized by the addition of TEA (1.23 wt %). The mixture was then gentle stirred for 40min. The dispersion in water and PU chain extension were achieved by adding HZ (0.77 wt%) and deionized water (63.70 wt %) to the neutralized prepolymer under high-speed stirring. To ensure that the reaction was completed, the mixture was stirred for 60min. This chemical procedure was well succeeded in producing PUs water dispersions with solid content about 30%. The weight fraction (%) of hard segment, $W(HS)$, is 38% (IPDI + HZ).

B – Nanocomposites

PU/MMT nanocomposites were prepared via solution blending. Initially, the MMT water dispersion was produced by mixing the clay (5 wt %) with deionized water for 24 hs at 65ºC. The PU water dispersion was blended with the MMT water dispersion at

room temperature under mechanical stirring for 15 min. The samples with different MMT weight contents were numbered as PU/MMT-1, PU/MMT-2, PU/MMT-3, PU/MMT-4 and PU/MMT-5, corresponding to MMT weight contents of 0%, 0.4%, 1.2%, 2.0% and 4.0% respectively.

Films were produced by casting the dispersions in a PVC mold and allowing them to dry at 17ºC for one week. The films were then annealed at 80ºC for 72 hs.

C – Characterization

Infrared spectra were collected in a Fourier transform infrared spectrophotometer (FTIR; Perkin–Elmer, model Spectrum 1000). Measurements were carried out using the attenuated total reflectance (ATR) technique. Each spectrum was a result of 64 scans with a resolution of 4 cm^{-1}.

Wide angle X-ray scattering (WAXS) analysis was performed in thin samples having thicknesses ranging from 0.8 to1.0 mm and 15 mm in diameter using a Philips, model PW1710 diffractometer operated with CuK_α irradiation at a scan rate of 2º 2θ/s in the range of 3 to 60º.

Small angle X-ray scattering (SAXS) measurements of synchrotron small angle X-ray scattering were performed using the beam line of the National Synchrotron Light Laboratory (LNLS, Campinas, Brazil). After passing through a thin beryllium window, the beam is monochromatized ($\lambda = 1.488$ Å) and horizontally focused by a cylindrically bent and asymmetrically cut silicon single crystal. The X-ray scattering intensity, $I_{(q)}$, was experimentally determined as a function of the scattering vector, q, whose modulus is given by Equation IV.1:

$$q = \frac{4\pi}{\lambda}\sin\theta \qquad \text{(IV.1)}$$

where λ is the X-ray wavelength and θ being half of the scattering angle. Each SAXS pattern corresponds to a data collection time of 900 s.

Static mechanical tests were performed using a universal testing machine (DL3000, EMIC) at 10 mm/min crosshead speed (DIN60). Samples were deformed up to 500% deformation. The tensile strength (σ_m), initial modulus (E) and toughness of the samples were extracted from the curves. The sample length between the clamps was 20 mm. The tests were performed at 28ºC (room temperature).

Swelling of PU/MMTs was carried out in deionized water at 37ºC using films having 15 mm in diameter. The sample mass-to-water volume ratio was kept constant and equal to 1/50 g.cm^{-3}. The samples were removed from water at the preselected time intervals, wiped gently and weighed using an analytical balance. Changes in sample weight were calculated according to Equation IV.2:

$$Water\ Uptake\,(\%) = \frac{w_t - w_o}{w_0} \times 100 \qquad \text{(IV.2)}$$

where w_o and w_t were the initial weight and the weight at time t, respectively. The average of three measurements was used to plot the results.

Preliminary information regarding the biodegradation of the materials was obtained by submitting them to hydrolysis at high pH. This type of biodegradation test was performed by weighing samples having 10 mm in diameter and immersing them in a NaOH 3 wt % aqueous solution. The samples were removed from the media at preselected time intervals, rinsed three times with distilled water, and immersed in distilled water for another hour. The specimens were then dried to a constant weight at 37ºC for 1 week and weighed using an analytical balance to determine the weight loss. The average of three measurements was used to report the results. The weight loss of the polymer films after degradation was evaluated as the residual weight (%), which was defined by Equation IV.3:

$$Residual\ \ Weight\,(\%) = 100 - \left(\frac{w_0 - w_t}{w_0} \times 100 \right) \qquad \text{(IV.3)}$$

D – Cell culture and viability assays

Extraction and direct contact tests were used to evaluate the cytotoxicity of the PU nanocomposites. Cementoblasts were isolated from the molars extracted from Wistar male rats (8 weeks old, 220-250 g) [18]. The extracted molars were rinsed with Dulbecco's phosphate-buffered saline solution without calcium and magnesium. Then the molars were immersed in a digestion solution, produced with the following components: 20 mL of Dulbecco's Modified Eagle Medium (DMEM)containing 0.04 collagenase (180 u/mL) and 0.5 mL trypsin at 37°C. This solution was used for five consecutive digestions and five cells populations were obtained at the end. The first two populations were discarded, while the other three produced a suspension of periodontal ligament cells that includes cementoblasts. The three suspensions of cells were centrifuged for 5 minutes at 1000 g. The cells of each population were then cultured in DMEM with 10% fetal bovine serum, penicillin G (10 unites/mL), streptomycin sulfate (10 mg/mL) and 0.25 anfotericin-b in a humidified atmosphere of 5% CO_2 at 37ºC. The cells were used for experiments at passage two. Cementoblasts cells were identified by RT-PCR and Western blot F-spondin cell marker.

Cementoblasts were plated in 24 well plates, and, after 2 hours, their viability was evaluated by using the MTT assay. This assay quantifies cell viability based on the reduction of tetrazolium salt to formazan crystals [16]. The PU/MMT samples were sterilized by UV radiation. Three samples were used in each MTT assay. In this study, cells were cultured on wells without PU samples to be used as positive controls and wells with no cells (only medium) were used as the negative control. Cementoblasts were seeded in contact with PU/MMT samples at density of $1x10^5$ cells/cm and then incubated at 37˚C and 5% CO_2. After 2 hours of incubation, the cells on the materials were observed by optical microscopy. After 72 hours of incubation, the culture medium was adjusted to 210 µl and 170 µl of MTT (5 mg ml^{-1}) was added to each well. Four hours later, formazan salts were dissolved with isopropanol. Then, 100 µl of the solution from each well was aspirated and poured in a 96-well plate for absorbance measurement at 595 nm [16].The absorbance was directly proportional to cell viability. Results were expressed as percentage of cell viability.

Data was statically analyzed by using the GraphPad Prism signed rank test. The results, expressed as the average of triplicate wells, were repeated three times. A total of nine wells were assayed in each experimental group. Probabilities less than 0.05 were considered as significant.

IV.3 – Results and Discussion

A – Infrared Spectroscopy

Typical infrared spectra of PU/MMT-1, PU/MMT-2, PU/MMT-3, PU/MMT-4, and PU/MMT-5 are shown in Figure IV.1. The characteristic absorption bands of poly(ester-urethanes) are assigned in Figure IV.1 and described in Table IV.1 where each absorption band frequency and the correspondent functional group are reported. In order to compensate for differences in signal intensity, the infrared spectra were normalized according to the $–CH_3$ region (3000–2800 cm^{-1}). It was observed that the position of the absorption bands of each specific functional group listed in Table IV.1 was similar both for PU/MMT-1 and PU/MMT-2 to PU/MMT-5 composites [19-28].

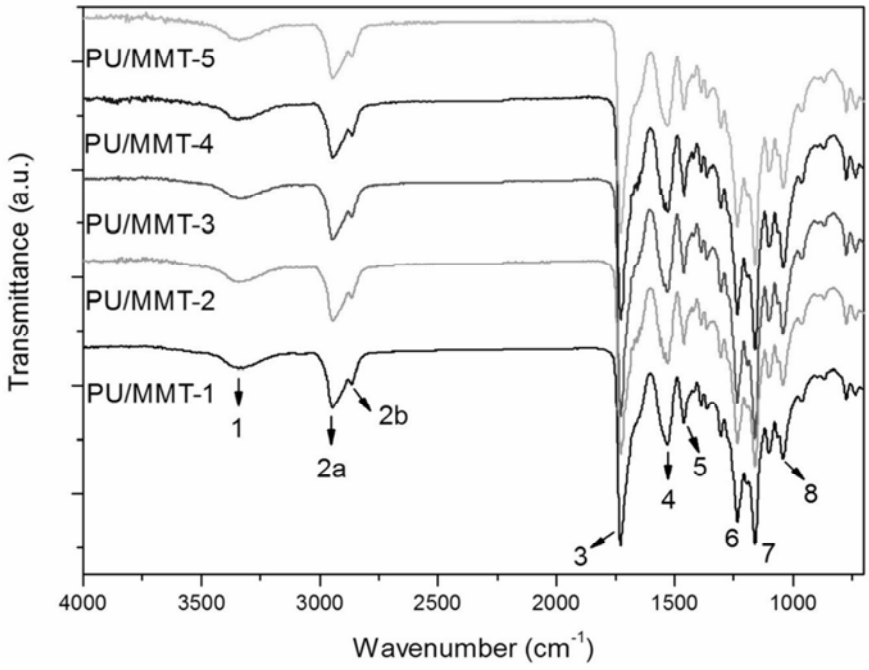

Figure IV.1 – FTIR spectra of PU/MMT-1 to PU/MMT-5 samples.

Table IV.1 – Relationship between FTIR absorption bands and functional group of observed in Figure 1.

Bands	Origin	Frequency (cm^{-1})	Assignment
1	N–H	3600–3150	Primary amine stretching vibration mode
		~3500	Free N–H stretching vibration band
		~3300	Hydrogen bonded N–H vibration band
2	$–CH_3$	3000–2800	Methylene stretching vibration modes
3	C=O	1760–1600	Carbonyl groups stretching vibrations
		1750-1725	Ester stretching vibration modes
		~1720	Free urethane stretching vibration band
		~1700	Hydrogen bonded urethane stretching vibration band
		~1660	Free urea stretching vibration band
		~1630	Hydrogen bonded urea stretching vibration band
4	>N–H	1640–1540	Secondary amide vibration modes
5	$–CH_3$	1470–1430	Methylene groups asymmetric bend vibration modes
6	C–N	1292–1226	Tertiary amide stretching vibration modes
7	C–O–C	1150	Ether stretching vibration
8	Si–O	1038	Stretching vibration mode

In order to obtain more detailed information regarding bands 1, 3, 4 and 6 to 8, the area under each band was calculated using the Origin® software. It is possible to draw a second order polynomial regression for curves where the area of bands 4 and 6 to 8 is plot as a function of the amount of MMT in PUs. The obtained curves show a good 2^{nd} order correlation factor (Figure IV.2-a). Since, the FTIR-ATR technique provides only surface information, up to 3 μm, the 2^{nd} order behavior may indicate that the presence of the filler modifies chain mobility and phase structure, allowing the migration of polar groups to the surface in samples having MMT up to 2%. For higher concentrations of MMT, clay re-agglomeration may occur and the resulting tactoids will be less effective in disturbing chain dynamics and phase morphology. However, no direct correlation

between band areas of bands 1 and 3 (Figure IV.2-b) and the composition of the systems could be drawn, indicating that a series of factors may affect these chemical functionalities when exposed to clay nanoparticles.

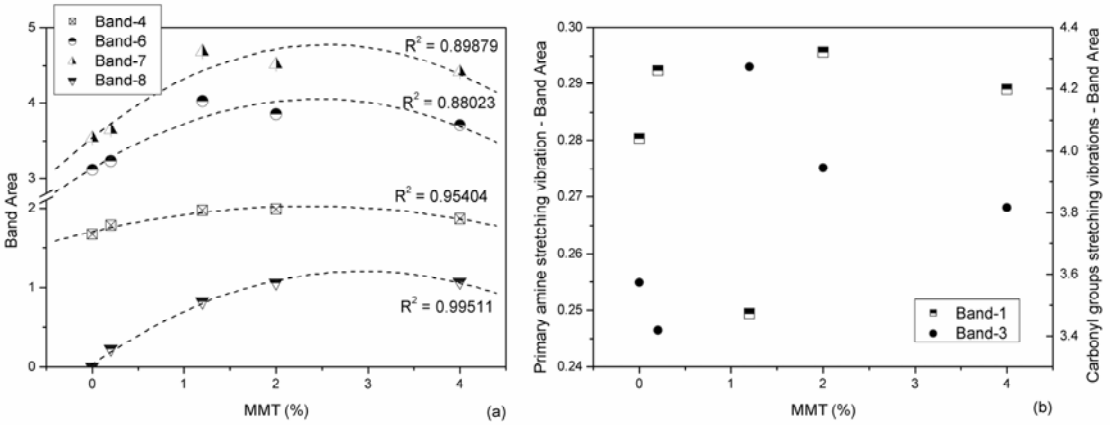

Figure IV.2 – Influence of filler content on band area of PU/MMT-1 to PU/MMT-5: (a) bands 4 and 6 to 8, (b) bands 1 and 3.

Bands 1 and 3 are usually related to the hydrogen bonding in segmented PU. In recent years, the relationship between specific interactions of band 1 and 3 and the phase behavior of polymer nanocomposites has been proposed [27]. In Figure IV.3 [27], possibilities of hydrogen bonding between MMT and PU matrix are sketched. The hydrogen bonding interactions occur between the hydroxyl group of MMT (proton donor) with proton-acceptor entity of PUs such as urea, urethane and ether [27, 29]. Since overlapping in band 1 and band 3 occurs, a deconvolution mathematical procedure (by using the PeakFit® software) was performed on spectra of Figure IV.1 to enhance resolution of each individual band. Figure IV.4(a) and Figure IV.4(b) illustrates, respectively, the deconvolution of the N–H region and the deconvolution of the carbonyl stretching region of PU/MMT samples.

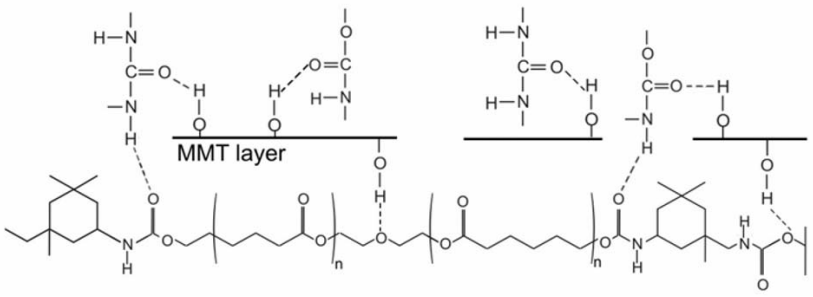

Figure IV.3 – Hydrogen bonding interaction between PU and MMT layer.

The ratio between the absorption band areas of bonded and free NH represents the NH groups which are hydrogen bonded. The extent of the carbonyl groups participating in hydrogen bonding in PUs can be expressed by a hydrogen-bonding index HBI(%), which is described by Equation IV.4 [2, 27]:

$$HBI(\%) = \frac{A_{1700}}{(A_{1700} + A_{1720})} \times 100 \qquad \text{(IV.4)}$$

where A_{1700} and A_{1720} are respectively the FTIR absorption band area of free urethane at 1720 cm^{-1} and bonded urethane at 1700cm^{-1}.

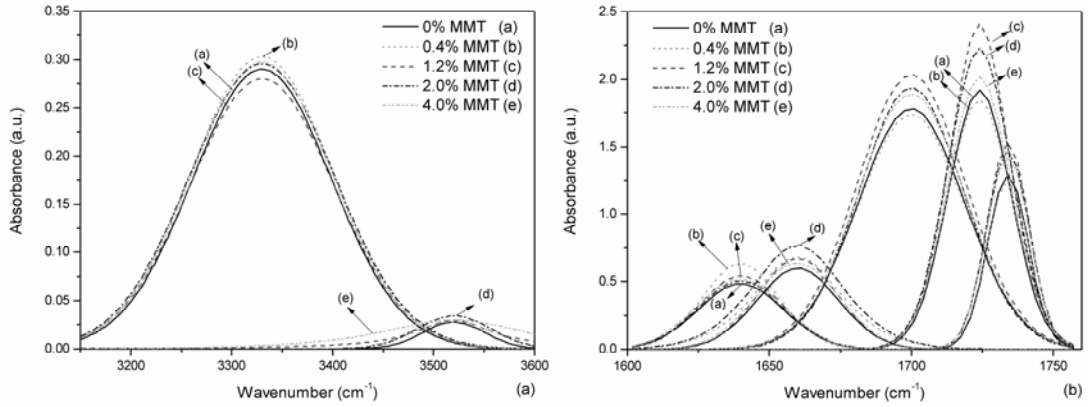

Figure IV.4 – Deconvoluted FTIR spectrum: (a) N–H stretching region, (b) carbonyl stretching region.

Figure IV.5(a) shows that the ratio between hydrogen bonded NH groups and free NH groups is slightly dependent on the MMT content. It can be seen that the NH bands of MMT/PUs are all nearly completely hydrogen bonded. Figure IV.5(a) shows also the 2nd-order relationship between $HBI(\%)$ and MMT(%), the plot suggests that the amount of carbonyl groups participating in hydrogen bonding in PU/MMTs goes through a minimum at clay contents close to 2 wt %. Well dispersed nanoparticles derived from clay can disturb the formation of hard and soft domains by reducing the mobility of the chain segments confined at the clay surfaces and by restricting the formation of hydrogen bonds between amine and carbonyl groups. These facts can lead

to materials having an enhanced degree of phase mixing. The introduction of clay nanoparticles into PU in concentrations higher than 2 wt % can lead to the production of agglomerates (tactoids) during film formation. The presence of agglomerates can reduce interfacial area and interactions between the polymer and clay particles. The degree of phase mixture, $DPM(\%)$, can be calculated from FTIR data as expressed Equation IV.5 [29]. Results are summarized in Figure IV.5(b).

$$DPM(\%) = \frac{(1 - HBI(\%)) \times W(HS)}{(1 - HBI(\%)) \times W(HS) + (1 - W(HS))} \quad \text{(IV.5)}$$

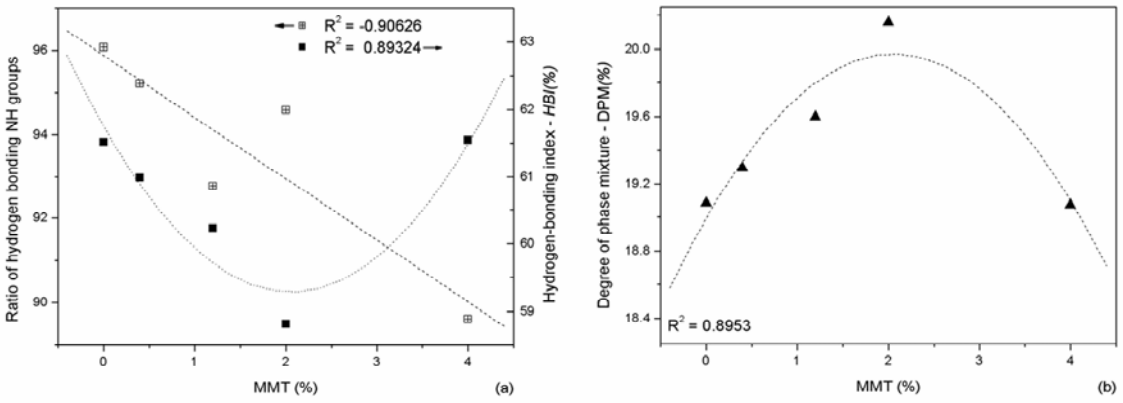

Figure IV.5 – Influence of filler content on: (a) ratio of hydrogen bonding NH groups and HBI(%) and (b) phase mixture.

Clay agglomerates are much larger than PU domains and phase separation would not be highly affected when agglomerates, instead of high aspect ratio nanoparticles, are present. Therefore, FTIR data suggests that the incorporation of clay particles up to 2 wt % MMT can result in highly well dispersed and delaminated clay platelets, while PUs containing clay particles in concentrations higher than 2wt% MMT can lead to particle re-agglomeration during film formation.

B – Wide angle X-ray scattering (WAXS)

Two types of polymer-layered nanocomposites are well described in the literature: intercalated nanocomposites and exfoliated nanocomposites. In the former, the polymer chains alternate with the inorganic layers in a fixed compositional ratio to yield a well

defined number of polymer layers in the intralamellar space. In this case, the WAXS patterns of intercalated nanocomposites show usually diffraction peaks associated with the interlayer distance at lower diffraction angles (2θ between 3-10º). In exfoliated nanocomposites, no diffraction peaks are shown, the number of polymer chains between the layers is almost continuously variable and the layers stand >10 nm apart [30, 31, 32]. Figure IV.6 shows the WAXS patters of PUs nanocomposites containing different amounts of MMT.

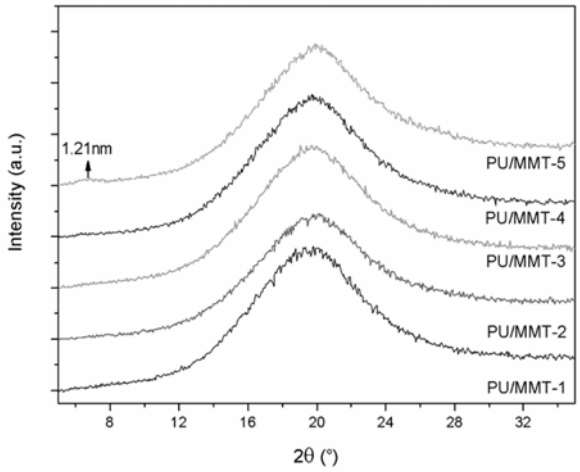

Figure IV.6 – WAXS pattern of PU/MMT-1 to PU/MMT-5.

No major diffraction peaks were observed for PU/MMTs, which can be related to the amorphous nature of poly(ester-urethane) produced by using low molar mass PCL diols (M_n<2000 g/mol) and low soft segment contents. Poly(ester-urethane) containing soft segments based on low molar mass PCL can present low degrees of phase separation that restrict soft segment segregation and therefore crystallization [33]. The large halo around 2θ=20º on the WAXS curves is typical of materials that have only short range order [33, 34, 35, 36].

Previous studies [32] showed that the diffraction peak of the MMT/Na^+ occurs around 2θ=7.4º, corresponding to the interlayer spacing of 1.21 nm. Thus the disappearance of peaks around 2θ=2–10º may indicate that the silicate layers were completely exfoliated and distributed uniformly within the amorphous domains in the PU matrix, being a nanometer-scaled composite. However, in PU/MMT-5, a small and broad diffraction

peak around 2θ=7.4º can be observed, which implies that part of the clay had re-agglomerated during the drying stage.

C – Small angle X-ray scattering (SAXS)

Figure IV.7(a), (b) and (c) shows, respectively, SAXS patterns of PU/MMT-1, PU/MMT-2 and PU/MMT-3. PU/MMT-4 and PU/MMT-5 SAXS experiments were not carried out. As expected from the randomly distributes particles embedded in an amorphous matrix, a circular scattering pattern with a homogeneous intensity distribution along the circle was obtained. The symmetric scattering patterns of PU/MMTs indicate that the films are isotropic.

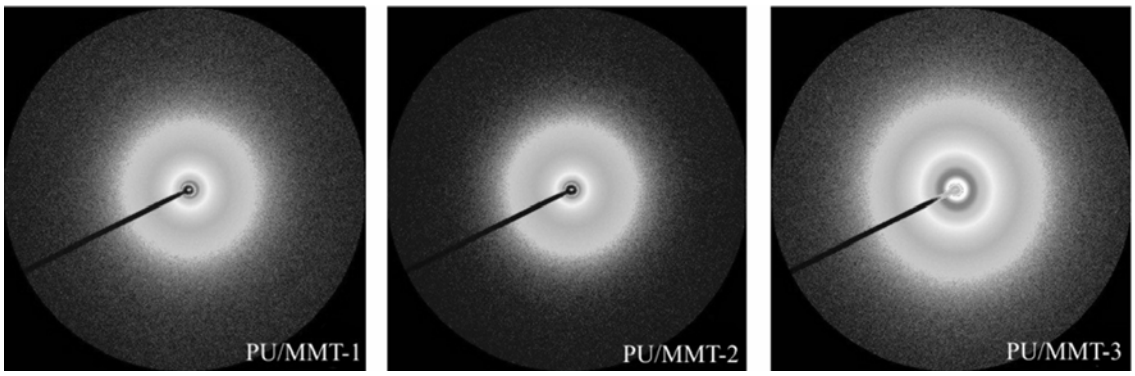

Figure IV.7 – SAXS pattern of: (a) PU/MMT-1, (b) PU/MMT-2 and (c) PU/MMT-3.

SAXS profiles as a function of the scattering vector, q, is shown in Figure IV.8(a). SAXS profiles do not exhibit any peak, confirming WAXS results and indicating that a high degree of exfoliation can be achieved by the clay dispersion, during mixing with PUs water dispersion. Further evaluation was obtained by applying the Lorentz correction on SAXS data (Figure IV.8(b)). The Lorentz correction describes the electron density fluctuation of polymer and is a good description of overall phase separation.
PU/MMT-1 corrected profile displays a broad scattering peak around q = 0.78nm^{-1}. This peak characterizes the presence of domains having different electronic densities that can be associated with the phase separation derived from the incompatibility between soft and hard segments in PU. Scattering data in Figure IV.8 also shows that the presence of clay nanoparticles disturbed the phase separation of the system, changing the matrix morphology. At low filler content, the scattering peak due to the PU phase separation

became narrowed, attesting the gradual increase of the hard-soft-segment degree of mixing. It is also possible to observe that scattering increased due to the presence of clay particles. Having clay particles higher electronic density than PU matrix, the scattered radiation achieves higher levels when nanoparticles were incorporated into PU. The same phenomenon is observed at PU/MMT-3 SAXS profile which is 10 times more intense due to the presence of 1.2 wt % MMT. At 1.2 wt % MMT composition, no scattering peak can be observed, demonstrating that a high degree of phase mixture was obtained. The SAXS results agree with WAXS and DPM(%) results described previously, confirming that a high degree of exfoliation can be achieved by the clay dispersion during mixing with PUs water dispersion for compositions with low clay content (<1.2 wt % MMT).

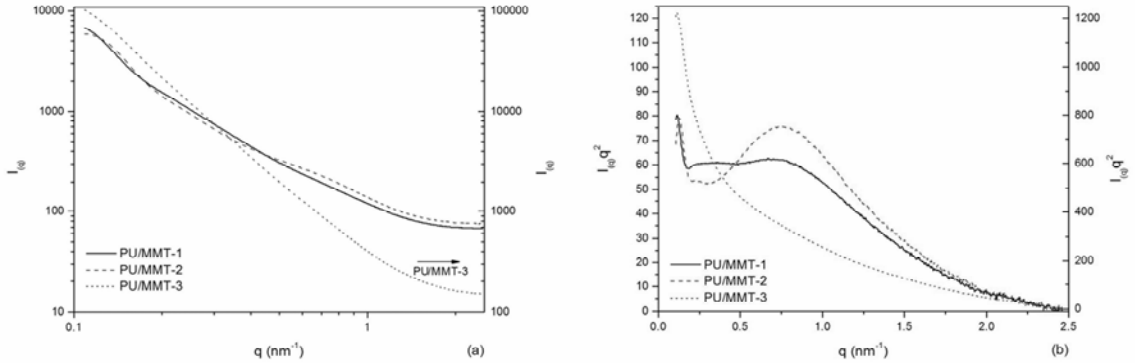

Figure IV.8 – (a) SAXS profiles of PU/MMT-1, PU/MMT-2 and PU/MMT-3 and (b) Lorentz correction.

D – Mechanical Properties

Figure IV.9 shows typical stress–strain curves for PU/MMT samples. Table IV.2 summarizes the values for the mechanical properties. The values of toughness and resilience in Table IV.2 were obtained by integrating the stress-strain curves and they can represent, respectively, the energy absorbed up to 500% deformation and the energy absorbed during elastic deformation. Finally, the work hardening degree was also calculated as the difference between toughness and resilience.

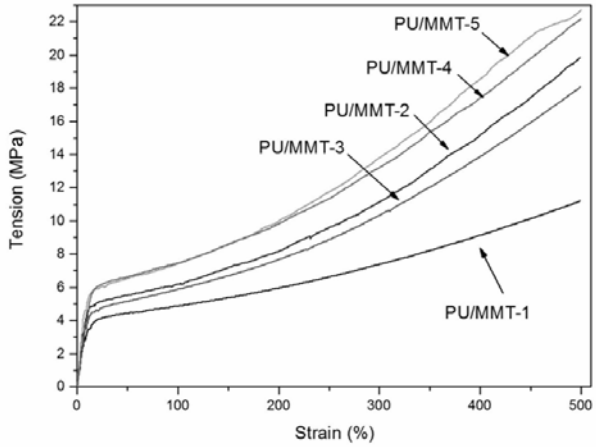

Figure IV.9 – Stress–strain curve of PU/MMT-1 to PU/MMT-5.

Table IV.2 – Mechanical properties of PU/MMT-1 to PU/MMT-5:

PU	σ_m (MPa)	Resilience (MJ/m^3)	Toughness (MJ/m^3)	Work hardening (MJ/m^3)
PU/MMT-1	11.40 ± 0.14	2.09 ± 0.69	703.59 ± 10.6	701.50 ± 11.2
PU/MMT-2	19.81 ± 0.97	1.88 ± 0.14	1053.49 ± 51.0	1051.60 ± 51.1
PU/MMT-3	19.09 ± 1.98	1.50 ± 0.50	1022.12 ± 99.1	1020.61 ± 114.1
PU/MMT-4	23.75 ± 1.07	2.65 ± 0.04	1300.42 ± 41.0	1297.78 ± 41.0
PU/MMT-5	24.63 ± 2.49	1.40 ± 0.80	1343.59 ± 167.4	1342.18 ±168.3

Obs.: σ_m = stress at 500% deformation

It was found good 2nd-order correlations between σ_m and the amount of filler content and between work hardening and amount of filler content, Figure IV.10. However, the resilience is not influenced significantly by the MMT content, as shown Figure IV.11.

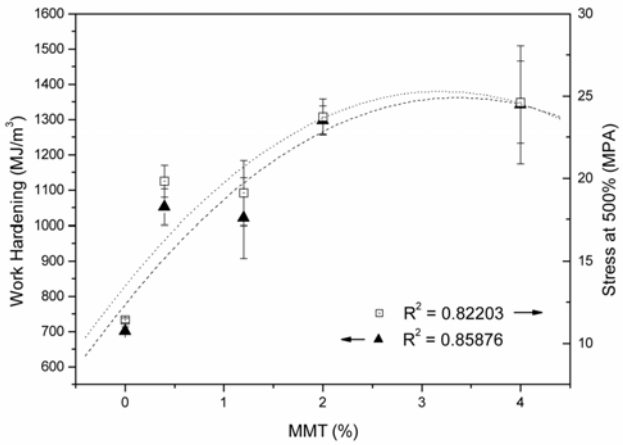

Figure IV.10 – Influence of MMT content on σm and work hardening

Results indicate that the filler content affect the deformation mechanisms during plastic deformation rather than the elastic deformation. Up to 2 wt % MMT content, the exfoliated particles interact strongly with polymeric chains, hindering plastic deformation and increasing the work hardening. According to Figure IV.6, in PU/MMT-5 that has contents of clay higher than 2%, part of clay particles is agglomerated. Since the agglomerated clay (tactoids) should have lower interfacial contact area, it works as localized regions of stress concentration rather than as reinforcing agents.

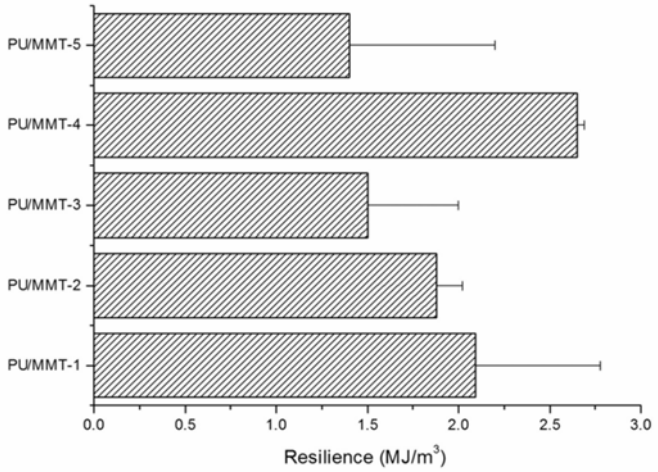

Figure IV.11 – Influence of MMT content on resilience.

E – Polymer Swelling

All polymers obtained in this study absorb water when immersed in distilled water as shown in Figure IV.13. The kinetics of water uptake differs for samples with and without nanoparticles. The rate of water uptake of PU/MMT-2 to PU/MMT-5 decreases with time going through a saturation limit, while PU/MMT-1 does not reach this limit, Figure IV.12.

The obtained waterborne PU matrix and PU nanocomposites contain anionic hydrophilic groups and thus have high water affinity. As predicted by Figure IV.2, the nanocomposites have superior hydrophilicity (they have larger number of surface polar

groups and hydrophilic particles) and thus higher initial rates of water uptake. In the initial stage of water absorption, PU/MMT-4 showed the highest rate of water uptake due to the larger number of surface polar groups (Figure IV.2) and higher degree of phase mixing (Figure IV.5(b)) derived from the presence of better dispersed nanoparticles. For samples having higher concentrations of MMT than PU/MMT-4 (i.e. PU/MMT-5 that has 4 wt.% of clay), the presence of agglomerates promotes the production of a PU having a lower degree of phase mixing and a less polar surface.

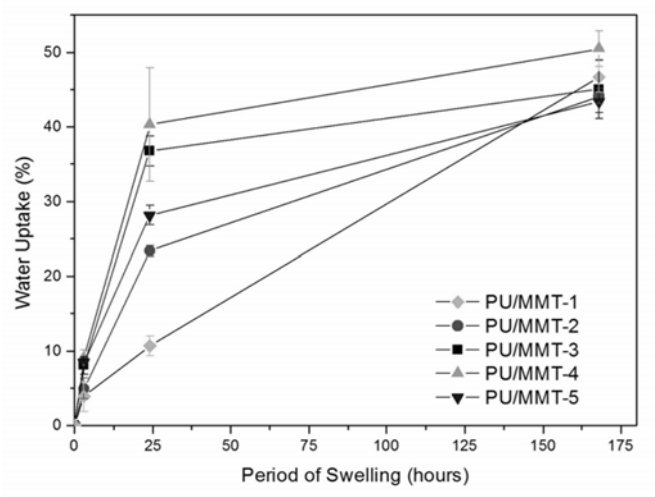

Figure IV.12 – Water uptake of PU/MMT-1 to PU/MMT-5.

F – Alkaline degradation tests

The alkaline degradation tests aim to accelerate the hydrolytic degradation process of PU. Figure IV.13 shows the kinetics of alkaline degradation of the samples. The degradation process of some polyester and PUs in alkaline solution is based on the hydrolytic attack of ester bonds [21]. As shown in Figure IV.13, this procedure caused a fast decay in sample mass during the first four hours of the test. These results also show that clay particles enhance the rate of PU hydrolysis, mainly because the rate of water absorption in PUs containing clay is much higher than in pure PU within the first moments of the contact between water and the materials (as observed in Figure IV.13).

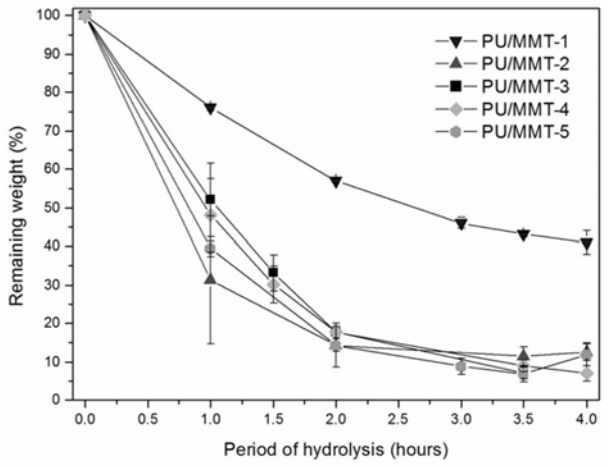

Figure IV.13 – Alkaline degradation of PU/MMT-1 to PU/MMT-5.

G – Cellular Viability

The cell viability measurements are presented in Figure IV.14 for cementoblasts cultured in contact with PU nanocomposites. There are no statistical differences in cell viability when PU nanocomposites are compared with the control. Therefore, PU nanocomposites can be considered non-toxic and capable of sustaining the proliferation of cementoblasts.

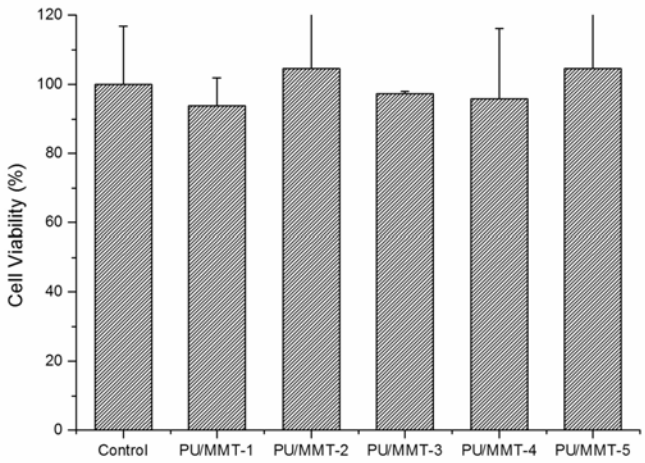

Figure IV.14 – Results from the MTT assay for PU/MMT-1 to PU/MMT-5. The percentage of cell viability of all samples was calculated versus the control medium.

IV.4 – Conclusion

Exfoliated waterborne PUs nanocomposites were successfully produced by direct solution blend. MMT content modified the degree of hydrogen bonding and the degree

of phase-separation, changing the matrix morphology. Data suggests that the incorporation of filler up to 2 w t% MMT resulted in highly well dispersed and delaminated clay platelets that contributed to an enhancement in the degree of phase mixture of the system. PU nanocomposites containing clay particles in concentrations higher than 2 wt % MMT led to particle re-agglomeration and phase separation. Both the rate of water absorption and the rate of hydrolytic degradation were increased by the presence of clay nanoparticles. Clay particles up 2 wt % were well dispersed in PU, leading to the formation of structures with higher degrees of phase mixing, polar surfaces and displaying improvements in mechanical properties. The obtained PU nanocomposites provided a good environment for the adhesion and proliferation of cementoblasts. They can be then considered suitable biomaterials for participating in procedures associated with periodontal regeneration.

IV.5 – Acknowledgements

The authors acknowledge the financial support from the following institutions: National Council for Scientific and Technological Development (CNPq), a foundation linked to the Ministry of Science and Technology (MCT) of the Brazilian Government; the State of Minas Gerais Research Foundation (FAPEMIG); and the National Synchrotron Light Laboratory (LNLS-Brazil) for the use of the SAXS beamline facilities.

IV.6 – References

1 – Pan, H.; Chen, D. Eur Polym J 2007, 43, 3766.

2 – Chen, G.; Ma, Y.; Zheng, X.; et al. J Polym Sci Phys 2007, 45, 654.

3 – Feng, Y. K.; Li, C. Y. Polym Degrad Stab 2006**,** 91, 1711.

4 – Jeong, E. H.; Yang, J.; Lee, H. S., et al. J Appl Polym Sci 2008**,** 107, 803.

5 – Wang, J.; Chen, Y.; Chen, R. J Polym Sci Phys 2007, 45, 519.

6 – Guelcher, S.A. Tissue Eng 2008, 14, 3.

7 – Minnen, B. V.; Leeuwen, M. B. M. V. J Mater Sci - Mater Med 2005, 16, 221.

8 – Hou, LT.; Yan, JJ. ; Tsai, AYM, et al. J Clin Periodontol 2004, 31, 68.

9 – Takata, T.; Wang, H. L.; Miyauchi, M. J Periodont Res 2001, 36, 322.

10 – Warrer, K.; Karring, T.; Nyman, S.; et al. J Clin Periodontol 1992, 19, 633.

11 – Coelho, M. B.; Pereira, M. M. J Biomed Mater 2005, 75B, 451.

12 – Pereira, M. M.; Jones, J. R.; Oréfice, R. L.; Hench, L. L. J Mater Sci - Mater Med 2005, 16, 1045.

13 – Pereira, M. M.; Jones, R. L.; Hench, L. L. Adv Appl Ceram 2005, 104, 35.

14 – Pereira, M. M.; Nazhat, S. N.; Jones, R. L.; Hench, L. L. Bioceramics 17 2005, 284, 757.

15 – Valerio P.; Guimaraes M. H. R. J Mater Sci - Mater Med 2005, 16, 851.

16 – Valerio P.; Pereira M. M.; Goes, A. M.; Leite, M. F. Biomaterials 2004, 25, 2941.

17 – Pereira, M. M.; Al-Saffar, N.; Selvakumaran, J.; et al. Bioceramics 17 2005, 284, 589.

18 – Kaneda, T.; Miyauchi, M.; Takekoshi, T.; et al. Bone 2004, 38, 420.

19 – Chattopadhyay, D. K.; Sreedhar, B.; Raju, K. V. S. N. Polymer 2006, 47, 3814.

20 – Bao, H.; Zhang, Z.; Ying, S. Polymer 1996, 37, 2751.

21 – Ayres, E., Oréfice, R. L., Yoshida, M. I. Eur Polym J 2007, 43, 3510.

22 – Marcos-Fernández A.; Abraham G. A.; Valentín J. L.; San Román J. Polymer 2006, 47, 785.

23 – Gorna, K.; Gogolewski, S. Polym Degrad Stab 2002, 75, 113.

24 – Gunes I. S.; Jana S. C. J Nanosci Nanotechnol 2008, 8, 1616.

25 – Coates, J. P. A Practical Approach to the Interpretation of Infrared Spectra. Encyclopedia of Analytical Chemistry, Ed. R.A. Meyers, J. Wiley & Sons, Ltd., Chichester, UK, 10815–10837, 2000.

26 – Jiang, X.; Li, J. H.; Ding, M. M.; et al. Eur Polym J 2007, 43, 1838.

27 – Jia, Q. M.; Zheng, M.; Zhu, Y. C.; et al. Eur Polym J 2007, 43, 35.

28 – Liu Y.; Pan C. Eur Polym J 34 1998, 621.

29 – Kim, B. H.; Choi, H. J.; Park, H. S.; et al. Compos Interfaces 2006, 13, 285.

30 – Tien, Y. I.; Wei, K. H. Polymer 2001, 42, 3213.

31 – Wang, J. C.; Chen, Y. H.; Wang, J. L. J Appl Polym Sci 2006, 99, 3578.

32 – Ayres, E. Poliuretanos e nanocompósitos biodegradáveis derivados de dispersões aquosas projetados para aplicações biomédicas. 2006. 196p., Tese Doutorado em Engenharia Metalúrgica e de Minad - Universidade Federal de Minas Gerais, Minas Gerais.

33 – Kim, B. K.; Lee, S. Y.; Xu, M. Polymer 1996, 37, 5781.

34 – Xu, J.; Shi, W.; Pang, W. Polymer 2006, 47, 457.

35 – Charnetskaya, A. G.; Polizos, G.; Shtompel, V. I.; Privalko, E. G.; Kercha, Y.; Pissis, P. Eur Polym J 2003, 39, 2167.

36 – Wu, S.; Cheng, A.; Hua, H.; et al. Polym Plast Technol Eng 2006, 45, 685.

Chapter V (Capítulo V)

Study of the morphology exhibited by linear segmented polyurethanes during shape memory cycles: an in situ experiment

I. M. Pereira[1,2]; R. L. Oréfice[2*]

[1]Coordenação de Metalurgia – Centro Federal de Educação Tecnológica de Minas Gerais – CEFET/MG Campus VII – Timóteo-MG
[2]Departamento de Engenharia Metalúrgica e de Materiais – Universidade Federal de Minas Gerais – UFMG, Belo Horizonte-MG

Abstract:

By using small-angle X-ray scattering, this study aims to identify the role of the morphological structures of linear segmented thermoplastic polyurethane during shape memory cycle. A deformed specimen was placed on a heating stage mounted at the beamline; the shape recovery was measured during 20 min. Furthermore, to study the influence of the temperature during recover, the specimens were subjected to different thermo-cycles. In each condition, the phase morphology and composition were investigated. Recovery process was separated into three stages. Bulk incompatibility and entropic recovery were the two controlling features for determining the final polyurethane morphology.

Keywords: Segmented polyurethanes, SAXS, microphase separation, and nano-morphology

V.1 – Introduction

Linear segmented thermoplastic polyurethane (PU) elastomers are multiblock copolymers which consist of the so-called hard and soft segments which can microphase separate to form hard and soft domains. The properties of these materials are dependent of phase morphology and phase separation of these domains [1, 2, 3]. Recent approaches have tailored PUs properties to yield thermo-responsive materials that can be used to create smart devices with the ability to memorize a permanent shape that can substantially differ from their initial temporary shape [4]. Described as shape memory polymers (SMP), they have many advantages over shape memory metal alloys. (i) low density (1.0–1.3 g/cm^3), (ii) wide range of actuation temperature, (iii) high shape recovery, (iv) low manufacturing cost, and (v) easy processing [5].

Generally, a SMP can be thought of as a material with morphology consisting of two phases: a shape fixing matrix phase and a shape memorizing dispersed phase. Above the actuation transition of the shape fixing phase, the polymer can be deformed from its primary shape to a secondary shape by the application of stress, and then locked into the secondary shape by cooling to below the actuation transition [6]. Although some research have been done in the past, the details of the morphological changes during shape memory cycle are still poorly understood, mainly because segmented PUs exhibit a complex phase structure depending on the type and size of segments used as well as on the processing conditions. By using small-angle X-ray scattering, this study aims to identify the role of the morphological structures of PU´s during shape memory cycle.

V.2 – Materials and Methods

A – Polymer synthesis

Poly(caprolactone diol) (PCL – Mn = 2000 g mol^{-1}), isophorone diisocyanate (IPDI), 2,2-bis(hydroxymethyl), propionic acid (DMPA) and dibutyl tin dilaurate (DBDLT) were obtained from Aldrich (St. Louis, MO). Triethylamine (TEA, 98%) and hydrazine

(HZ, 25%) were purchased from Vetec (RJ, Brazil). All these chemicals were employed throughout this work without any previous treatment.

PU was synthesized by the conventional prepolymer method, using a 250 mL three neck glass flask equipped with a heating mantel, a mechanical stirrer, a thermometer under nitrogen atmosphere. In the first step, prepolymer was obtained by reacting PCL (23.9 wt %), DMPA (1.2 wt %) and IPDI (9.3 wt %) at 2 NCO/OH ratio for about 3.5h. During this time, DBDLT was added twice. The reaction was carried out at 70–75ºC. After cooling down to 40ºC, the carboxylic acid groups were neutralized by the addition of TEA (0.9 wt %). The mixture was then gentle stirred for 40min. The dispersion in water and PU chain extension were achieved by adding HZ (0.7 wt %) and deionized water (64 wt %) to the neutralized prepolymer under high-speed stirring. To ensure that the reaction was completed, the mixture was stirred for 60min. This chemical procedure was successful in producing PUs water dispersions with solid content about 35%. The weight fraction (%) of hard segment, $W(HS)$, is 38% (IPDI + HZ). PU synthesis procedure is detailed described in a previous work [7].

B – Infrared spectroscopy

Infrared spectra were collected in a Fourier transform infrared spectrophotometer (FTIR; Perkin–Elmer, model Spectrum 1000). Measurements were carried out using the attenuated total reflectance (ATR) technique. Each spectrum was a result of 64 scans with a resolution of 4 cm^{-1}.

C – Synchrotron small angle X-ray scattering (SAXS)

SAXS measurements of synchrotron small angle X-ray scattering were performed using the beam line of the National Synchrotron Light Laboratory (LNLS, Campinas, Brazil). After passing through a thin beryllium window, the beam is monochromatized ($\lambda = 1.488$ Å) and horizontally focused by a cylindrically bent and asymmetrically cut silicon single crystal. The X-ray scattering intensity, $I_{(q)}$, was experimentally

determined as a function of the scattering vector, q, whose modulus is given by Equation V.1:

$$q = \frac{4\pi}{\lambda}\sin\theta \qquad \text{(V.1)}$$

where λ is the X-ray wavelength and θ being half the scattering angle.

Each SAXS pattern corresponds to a data collection time of 900 s. From the experimental scattering intensity produced by all the studied samples, the parasitic scattering intensity produced by the collimating slits was subtracted. All SAXS patterns were corrected for the non-constant sensitivity of the position sensitive X-ray detector, for the time varying intensity of the direct synchrotron beam and for differences in sample thickness. Because of the normalization procedure, the SAXS intensity was determined for all samples in the same arbitrary units so that they can be directly compared. The sample-detector distance of 551.6 mm was used during the measurements.

D – Mechanical Properties and Shape memory properties (SM)

Shape memory experiments were done at room temperature using a universal testing machine (DL3000, EMIC). The sample length between the clamps was 20mm. A shape recovery cycle consisted of the following steps: (1) Samples DIN60 were deformed to a defined strain, $L_m = 120$ mm, at 10 mm/min crosshead speed. (2) While maintaining the strain at L_m, samples were cooled with liquid N_2. (3) Mechanical constraints on the polymers were removed. (4) The samples were subsequently submitted to a thermo-cycle to recover its original shape. Figure V.1 illustrates a shape-memory thermomechanical cycle test.

During Cycle-A, the deformed sample was heated to 37^{o}C in an oven, and stayed at this temperature for 17hs. The recovery during thermo-cycle “B” was carried out within two heating stages. First, the specimen was heated to 37^{o}C for 17hs then heated for 10 min

at 50°C. During thermo-cycle "C", the sample was heated to 50°C for 30min. Finally, in Cycle-E the sample stayed at 80°C for 20min. The thermo-cycle parameters are described in Table V.1.

Figure V.1 – Shape memory cycle steps

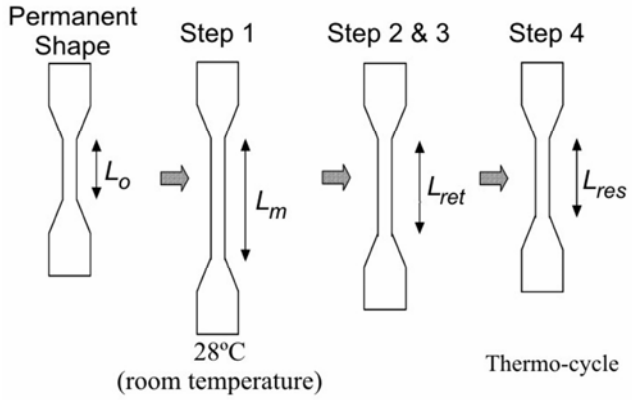

Table V.1 – Thermo-cycle

	Temp.	time
Cycle-A	37°C	17 hs
Cycle-B	37°C	17 hs
	50°C	10 min
Cycle-C	50°C	30 min
Cycle-E	80°C	20 min

The SM properties of the materials were described by the strain recovery ratio, R_R, and the strain fixity ratio, R_f. Both can be determined according to Equation V.2 and Equation V.3:

$$R_r(\%) = \frac{L_m - L_{\mathrm{Res}}}{L_m - L_o} \times 100 \qquad \text{(V.2)}$$

$$R_f(\%) = \frac{L_{\mathrm{Ret}} - L_o}{L_m - L_o} \times 100 \qquad \text{(V.3)}$$

where: L_o is the original length, L_m is the deformed length, L_{ret} is retained length and L_{res} is the length after the recovery.

The mechanical properties were described by the yield strength (σ_e), maximum strength (σ_m), and the young modulus (E).

E – In situ recovery

One deformed specimen was placed on a heating stage mounted at the beamline. The specimen was heated to 50°C – 60°C and the shape recovery was measured during 20 min. The SAXS patterns were recorded at 7.2 min, 8.3 min, 9.3 min, 11.0 min, 12.1 min, 13.1 min, 14.2 min, 15.2 min, 16.3 min, 17.3 min, 18.4 min and 19.4 min.

V.3 – Results and discussion

A typical infrared spectrum of obtained PU is shown in Figure V.2(a). The characteristic bands of poly(ester-urethane) are marked in the figure. The primary amine stretching modes appear at 3600–3150 cm^{-1}. The carbonyl group stretching vibrations, C=O, appear at 1760–1600 cm^{-1}. The secondary amide absorption, >N–H, appears at 1640–1540 cm^{-1}. The band at 1150 cm^{-1} is assigned to the stretching of the –C–O–C– group [7]. Figure V.2(b) shows typical stress–strain curves of shape memory specimens.

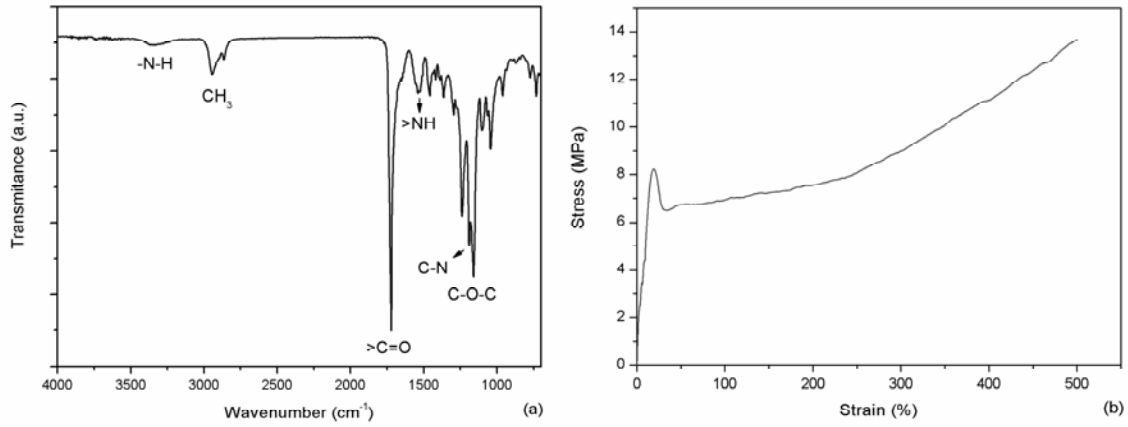

Figure V.2 – (a) FTIR curve and (b) Stress X strain curve.

PU's are characterized by the following mechanical properties: σ_e = 8.2±0.5 MPa, σ_{max} = 13.8±0.1 MPa and E = 2.2±0.5 MPa. R_R of Cycle-A, Cycle-B, Cycle-C and Cycle-E are, respectively, 71%, 82%, 88% and 98%. Low values of strain fixity ratio were observed, R_f =31±2.2%. Upon removing the strains at Step3 a significant recover of strain occurs and thus low values of R_f were observed. Different factors, derived from the SM cycle configuration, may have contributed to the present results. To maintain a

deformed shape in a stable manner, new chain positions must be fixed by new bonds. The development of the new physical entanglements (temporary bonds) between the polymeric chains is a result of a temperature decrease and/or forced chain alignment [8]. In the present work, after Step-1, samples were gripped to an apparatus, removed from the testing machine and immersed in liquid nitrogen. In consequence, the metastable structure, developed during the strain, were partially released, contributing to low values of R_f. A second factor, temperature, may also contribute to low values of R_f. According to Ping *et al* [9], when the deformation temperature is too low (30^{o}C below the melting temperature of the soft segment), the shape recovery starts at a lower temperature and takes place over a wide temperature range. As room temperature is superior to 25^{o}C, the lowest recovery temperature of obtained PUs might be lower than the room temperature and shape recovery may start after Step-3.

Figure V.3 illustrates SAXS patterns of the obtained PU during different stages of shape-memory thermomechanical cycle and during *in situ* recovery. SAXS measures the scattering intensity as a function of the incident X-ray beam. The technique is informative for fine morphologies at the nanometer level because it is sensitive to the differences in electron density within a material. The patterns and intensity distribution of SAXS are dependent on the shape, the size and size distribution of scattering objects [10]. In Figure V.3(b), it is observed two maxima occurring along the stretching direction on both sides of the beam stopper. The maxima are due to the scattering from the oriented structure formed during deformation process. The patterns indicate a high degree of orientation obtained from deformation process [11]. When the deformation is applied to the specimen, polymer chains will align to the extension direction and promote crystallization. During *in situ* recovery tests, the anisotropic orientation of the lamellae in the samples disappears. The different thermo-cycle promotes unlike reorientation of the deformed structure. The new patterns are function of the energy injected in the system. Higher temperature treatment brought more energy to the system which returned to the original configuration. As observed, the initial high scattering intensity phase was restored.

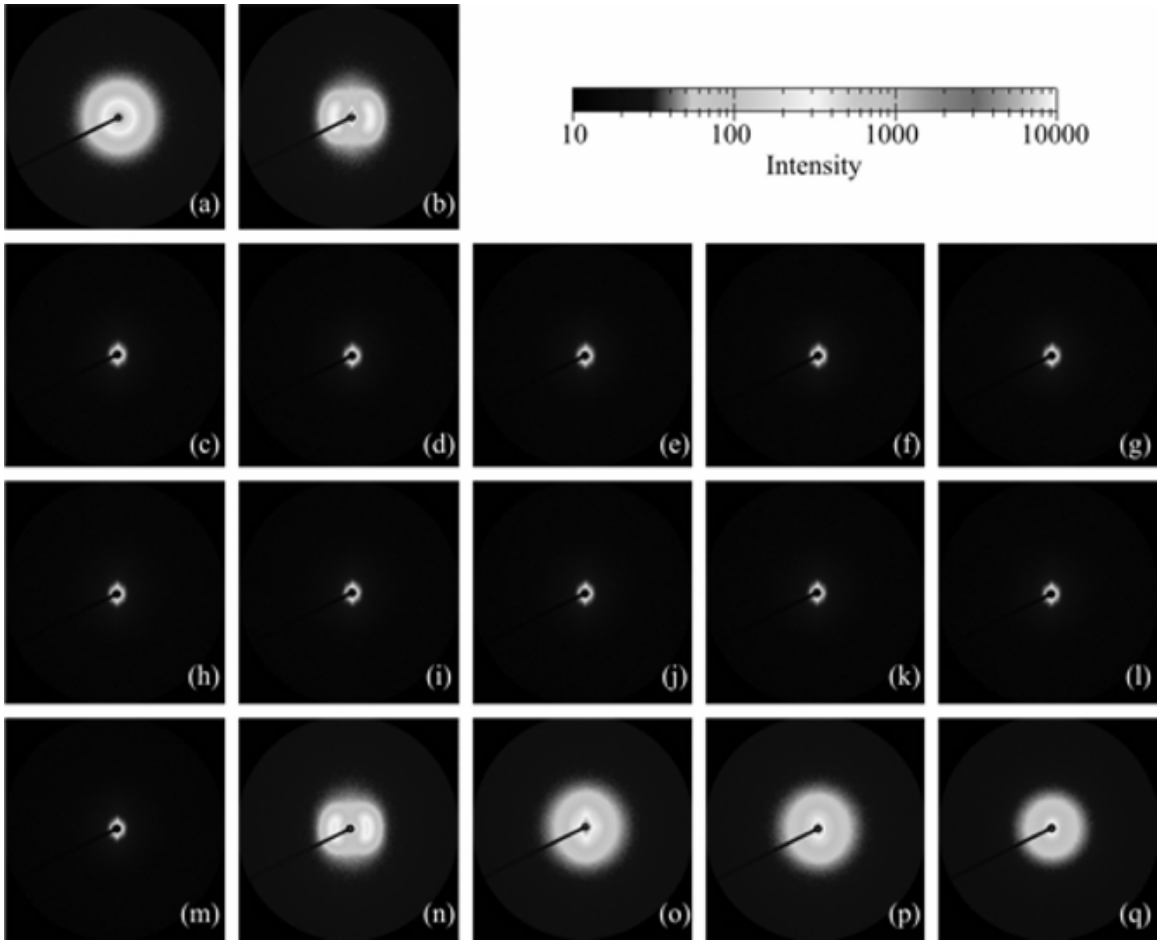

Figure V.3 – SAXS pattern of: (a) undeformed specimen, (b) deformed specimen, (c-m) *in situ* recovery: 7.2 min to 18.4 min, (n) Cycle-A, (o) Cycle-B, (p) Cycle-C, (q) Cycle-E.

Figure V.4(a) illustrates SAXS data of the obtained PU during different stages of shape-memory thermomechanical cycle. The scattering peak observed arises due to local heterogeneities in the electron density of the materials and it is usually interpreted as a consequence of the presence of distinct microphases with different electronic densities. However, discussing the phase separation, it is convenient to employ the Lorentz correction, Q_{inv}, which describes the electron density fluctuation of polymer and is a good approximation to estimate the overall degree of phase separation in segmented polymers, Figure V.4(b) [10, 12, 13]. The invariant quantity, Q_{inv}, can be obtained by integrating $I_{(q)}q^2$ over the range of scattering angles, Equation V.4 [10, 12, 13].

$$Q_{inv} = \int_0^{\infty} I_{(q)} q^2 dq \tag{4}$$

where $I_{(q)}$ is X-ray scattering intensity and q the scattering vector.

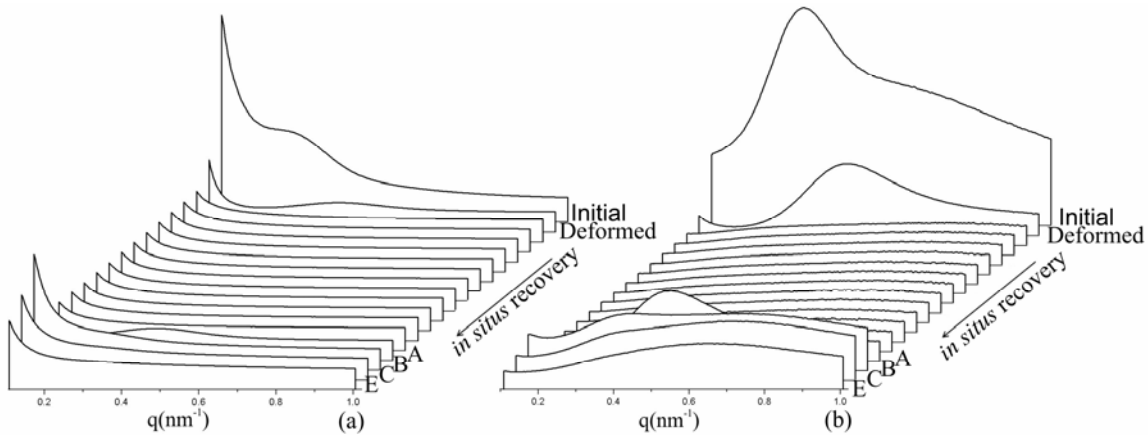

FigureV.4 – (a) SAXS curves of obtained and (b) Deconvoluted Lorentz SAXS pattern

The contribution of each phase to the Lorentz corrected SAXS patterns was separated by a deconvolution procedure. Figure V.5 illustrates the obtained deconvoluted curves.

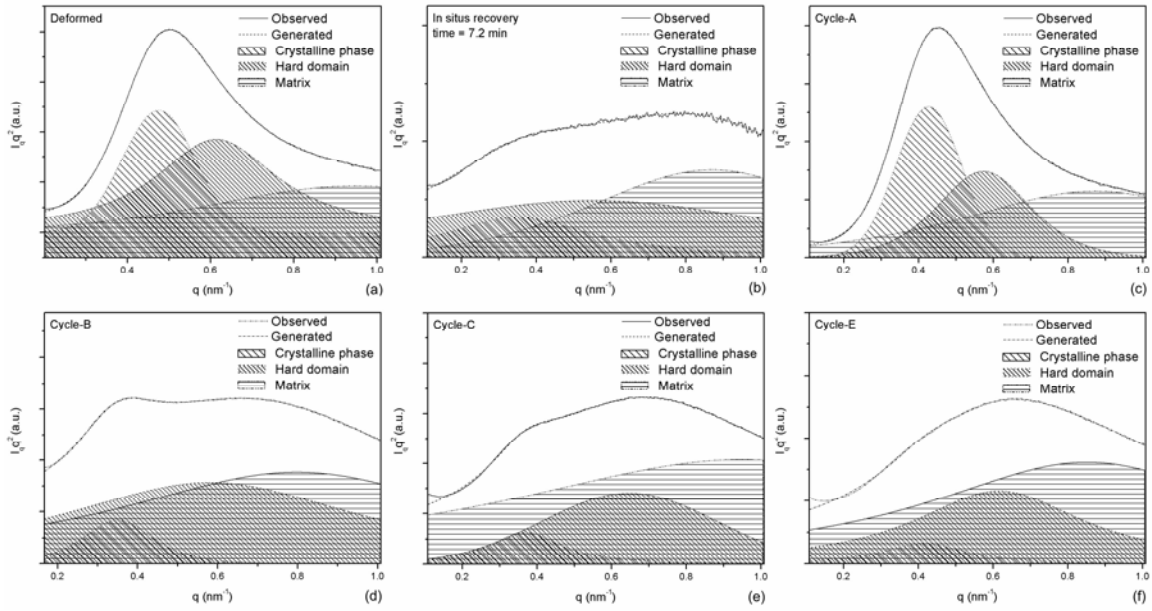

Figure V.5 – Deconvoluted Lorentz SAXS pattern: (a) deformed specimen, (b) in situ recovery, (c) Cycle-A, (d) Cycle-B, (e) Cycle-C, (f) Cycle-E.

Q_{inv} of each phase was obtained as fraction of the total area. As observed in Figure V.6, shape recovery during SAXS experiment occurred within three stages. The stages are distinguished at the hard domain curve. During the first seven minutes of recovery, the hard domain content decrease (first phase) followed by a fast increase in the hard domain fraction (second phase) and, finally, the hard domain fraction become stable (third phase). During the *in situ* tests, the crystalline fraction decreases because the soft segment crystals melt, enriching the matrix phase with soft segments. As a consequence, in the bulk matrix, the repulsive interaction between the dissimilar hard and soft segments increases, increasing their immiscibility and leading to hard domain formation. However, the hard domain segregation is limited by the hard segment nature. The hard segment low mobility stops the segregation process and the hard domain formation stabilizes [13].

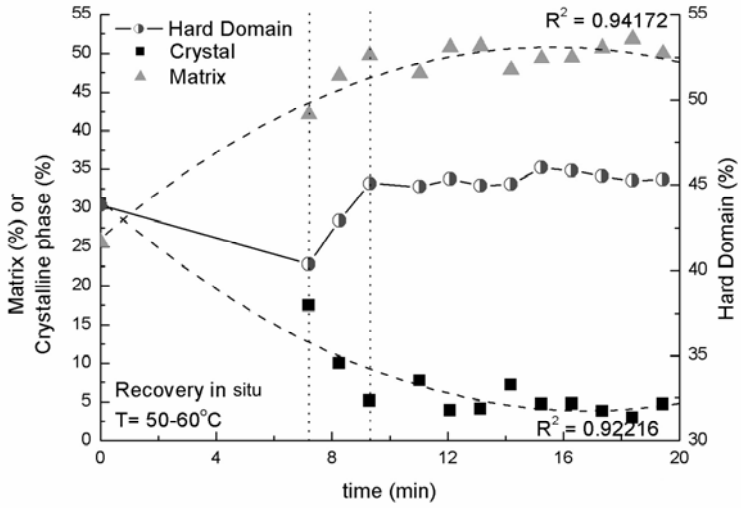

Figure V.6 – PU multi-phase evolution during in situ tests.

Figure V.7 illustrates PU morphology after the different thermo-cycles. *In situ* results may be extrapolated to the results observed after the thermo-cycle. According to SM tests, the thermo-cycle "A" promotes shape recovery, however, the energy injected in the system is enough to ensure only the first stage of shape recovery. As observed at Figure V.7, during Cycle-A the hard domain fraction decrease, but the temperature treatment is not enough to melt the crystals, change the matrix composition, increase the incompatibility and promote domain formation. Cycle-B ensures the three stages of shape recovery. However, higher values of R_R were not achieved due to the first step of

the thermo-cycle. The cycle-B first step acts as stress release treatment, decreasing the energy stored during deformation. Therefore, the polymeric chains are not able to recover their strongly coiled conformation consequently lower values of R_R are obtained. Thermo-cycle "C" and "E" complete the 3 stages of shape recovery. Thermo-cycle "E" ensures higher R_R values mainly because the higher temperature treatment guarantees melting of larger crystals fraction.

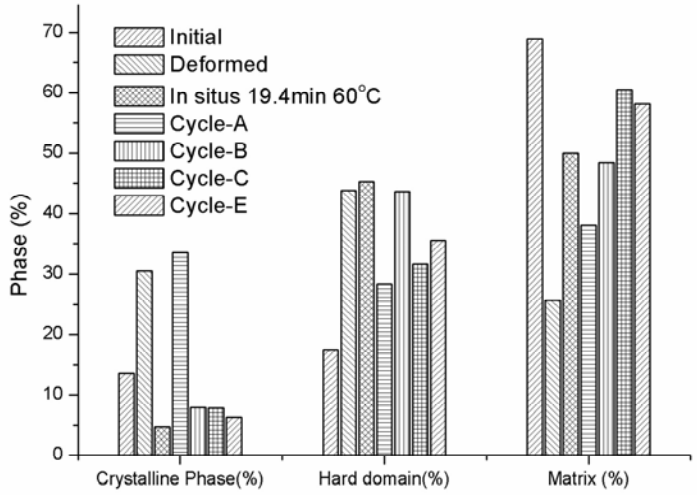

Figure V.7 –PU multi-phase evolution during in situ tests; (b) PU multi-phase during SM cycle.

V.4 – Conclusions

The development of the phases during shape memory cycles applied to polyurethanes was successfully monitored by using in situ SAXS experiments. It was shown that during the recovery stage of the PU shape, soft segment crystallites are progressively melted while phase separation becomes increasingly important until a new thermodynamic equilibrium point is reached that defines the final PU nanostructure.

V.5 – Acknowledgments

The authors acknowledge the financial support from the following institutions: National Council for Scientific and Technological Development (CNPq), a foundation linked to

the Ministry of Science and Technology (MCT) of the Brazilian Government; the State of Minas Gerais Research Foundation (FAPEMIG); and the National Synchrotron Light Laboratory (LNLS-Brazil) for the use of the SAXS beamline facilities.

V.6 – References

1 – Oertel, Günter. Polyurethane Handbook. 2nd ed. New. York: Hanser Publisher, 1994 (11–45).

2 – Pan H, Chen D. Eur Polym J 2007;43:3766–72

3 – Chen G, Ma Y, Zheng X, et al. J Polym Sci B 2007;45(6):654–60.

4 – Lendlein A, Langer R. Science 2002;296(5573):1673–6.

5 – Yang JH, Chun BC, Chung YC, Cho JH. Polymer 2003;44(11):3251–8.

6 – Wilson TS, Small W, Benett WJ, et al. Proc SPIE - Int Soc Opt Eng. 60070R-1-8, 2005.

7 – Pereira IM, Carvalho S, Pereira MM, Leite MF, Oréfice RL J Appl Polym Sci 2009; Published Online: Jun 2 2009 DOI: 10.1002/app.30404.

8 – Gall K, Dunn ML, Liu YP, Stefanic G, Balzar. Appl Polym Sci 2004, 85(2):290–2.

9 – Ping P, Wang W, Chen X, Jing X. Biomacromolecules 2005, 6(2):587–92.

10 – Chang SL, Yu TL, Huang CC, et al. Polymer 1998;39(15):3479–89.

11 – Jiang ZY, Tang YJ, Men YF, et al. Macromolecules 2007;40(20):7263–9.

12 – Wang SH, Zhang Y, Ren WT, et al. Polymer Testing 2005;24(6):766–74.

13 – Li YJ, Kang WX, Stoffer JO, et al. Macromolecules 1994;27(2):612–4.

Chapter VI (Capítulo VI)

The morphology and phase mixing studies on poly(ester urethane) during a low temperature shape memory cycle

I. M. Pereira[1,2]; R. L. Oréfice[2*]

[1]Coordenação de Metalurgia – Centro Federal de Educação Tecnológica de Minas Gerais – CEFET/MG Campus VII – Timóteo-MG
[2]Departamento de Engenharia Metalúrgica e de Materiais – Universidade Federal de Minas Gerais – UFMG, Belo Horizonte-MG

Abstract:

Three series of low molecular weight shape memory poly(ester-urethane) with varying hard-segment content were synthesized. The materials were designed to display a three-phase structure consisting of a disperse phase formed by crystallites and hard domains embedded in an amorphous matrix. The structure and thermal properties were investigated using techniques such as: modulated differential scanning calorimetry (MDSC), dynamic mechanical analysis (DMA) and small angle X-ray scattering (SAXS). The results were associated with the morphological changes observed during a low temperature shape-memory cycle. The recover was observed to be triggered by the melting of the crystallites and by the strong interactions among hard domains. Temporary shape was stored by the metastable structure formed during deformation.

Keywords: Shape memory, poly(ester urethane), SAXS, DMA, MDSC

VI.1 – Introduction

Shape memory polymers (SMPs) are thermo-responsive materials generally consisted of two phases: a fixing matrix phase and a shape memorizing dispersed phase. These polymers are able to store and recover large strains by application of a prescribed thermo-mechanical cycle. The procedure is to apply a specified initial deformation (pre-deformation), cool the pre-deformed shape under constraint to a lower temperature where the shape is fixed (storage), and then heat the material to recover the original shape (recovery) [1-4].

In SMPs, the relative motion and rearrangement of molecular chains is the primary inelastic strain mechanism responsible for the shape-memory effect. The establishment and the annihilation of a metastable structure store and recover the deformation during the SM cycle. For instance, to store a deformed shape in a stable manner, new chain positions must be fixed by new bonds. A fixed shape can be achieved by cooling the material below a transition temperature following significant chain alignment after chain slip. The newly formed bonds provide a storage mechanism for macroscopic stresses and increased chain organization (lower entropy). To recover the original shape, the formed bonds are released upon subsequent heating. At higher temperatures, the bonds are weakened and the low entropy state drive individual chains toward their initial positions, facilitating shape memory [2, 3].

This study aims to identify the role of the chemical and the morphological structures of a series of shape-memory segmented polyurethanes with different hard segment content during a low temperature shape memory cycle – sample subjected to deformation at temperatures lower than T_{trans}.

The modulated differential scanning calorimetry (MDSC) was used to study morphology. A dynamic mechanical analyzer (DMA) was used to determine the temperature dependence of the modulus in the transition regime. Additionally, SAXS measurements were carried out to investigate the structural changes during shape memory cycle.

VI.2 – Materials and Methods

A – Prepolymer synthesis

Poly(caprolactone diol) (PCL – Mn = 1250, 2000 g mol^{-1}), isophorone diisocyanate (IPDI), 2,2-bis(hydroxymethyl), propionic acid (DMPA) and dibutyl tin dilaurate (DBDLT) were obtained from Aldrich (St. Louis, MO). Triethylamine (TEA, 98%) and hydrazine (HZ, 25%) were purchased from Vetec (RJ, Brazil). All these chemicals were employed throughout this work without any previous treatment. PUs were prepared by the prepolymer mixing method, according to a procedure described in previous work [5]. The feed ratios are shown in Table VI.1, where $W(HS)$ is weight fraction of hard segment content, obtained according to Equation VI.1.

$$W(HS) = \frac{Weight_{IPDI} + Weight_{HZ}}{Weight_{PU}} \times 100 \qquad \text{(VI.1)}$$

Table VI.1 – Composition (wt. %) of waterborne PUs

	PCL		DMPA	IPDI	HZ	TEA	$W(HS)$
	1250	2000					
PUA	55.4	–	4.5	34.6	2.1	3.4	38.0
PUB	23.7	37.9	3.8	29.6	2.1	2.9	32.6
PUC	–	66.1	3.3	25.8	1.9	3.0	28.5

B – Modulated differential scanning calorimetry (MDSC)

MDSC measurements were performed using a TA Instruments 2920. The following protocol was applied to each sample: (1) heating from room temperature to 110°C at 15°C min^{-1}, (2) holding for 3.00 min at 110°C, (3) cooling to –110°C at 3.00°C/min, modulating +/– 1.00°C every 60 seconds, (4) holding for 3.00 min at –110°C and (5) heating again to 110°C with 3.00°C/min modulating +/– 1.00°C every 60 seconds. The melting temperature was taken as peak maxima, the glass transition temperature (T_g) was obtained by the analyzing software of the calorimeter.

C – Dynamic Mechanical Analysis – DMA

Dynamic mechanical properties were investigated by a TA Instruments DMA 800 equipment, with a single cantilever clamp at heating rate of 3°C/min and N_2 atmosphere. The test frequency was 5 Hz. The temperature varied from -100°C to 90°C.

D – Synchrotron small angle X-ray scattering (SAXS)

SAXS measurements of synchrotron small angle X-ray scattering were performed using the beam line of the National Synchrotron Light Laboratory (LNLS, Campinas, Brazil). After passing through a thin beryllium window, the beam is monochromatized ($\lambda = 1.488$Å) and horizontally focused by a cylindrically bent and asymmetrically cut silicon single crystal. The X-ray scattering intensity, $I_{(q)}$, was experimentally determined as a function of the scattering vector, q, whose modulus is given by Equation VI.2:

$$q = \frac{4\pi}{\lambda}\sin\theta \qquad \text{(VI.2)}$$

where λ is the X-ray wavelength and θ being half the scattering angle.

Each SAXS pattern corresponds to a data collection time of 900 s. From the experimental scattering intensity produced by all the studied samples, the parasitic scattering intensity produced by the collimating slits was subtracted. All SAXS patterns were corrected for the non-constant sensitivity of the position sensitive X-ray detector, for the time varying intensity of the direct synchrotron beam and for differences in sample thickness. Because of the normalization procedure, the SAXS intensity was determined for all samples in the same arbitrary units so that they can be directly compared. The sample-detector distance of 551.6 mm was used during the measurements.

E – Mechanical Properties

The tensile strength (σ_m), elongation at break (ε_m), the initial modulus (E), toughness and resilience of the samples (DIN60) were measured using universal testing machine (DL3000, EMIC) at 10mm/min crosshead speed. The sample length between the clamps was 20mm. The tests were performed at 28°C (room temperature). The values of toughness and resilience were obtained by integrating the stress-strain curves and they can represent, respectively, the energy absorbed until rupture and the energy absorbed during elastic deformation.

F – Shape memory properties (SM)

SM experiments were done at room temperature using a universal testing machine (DL3000, EMIC). The sample length between the clamps was 20mm. A shape recovery cycle consisted of the following steps: (1) Samples DIN60 were deformed to a defined strain, close to L_m = 120 mm, at 10 mm/min crosshead speed. (2) While maintaining the strain at L_m, samples were cooled with liquid N_2. (3) Mechanical constraints on the polymers were removed. (4) The samples were subsequently heated to 80°C in an oven, and stayed at this temperature for 20min to recover their original shape. This completes one thermo-mechanical cycle, Figure VI.1.

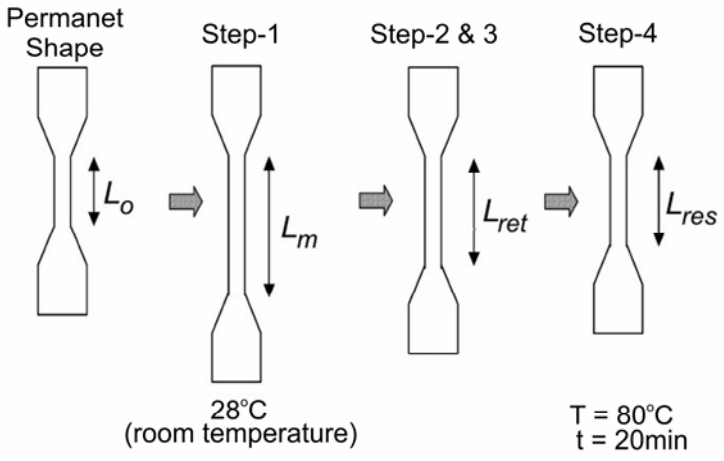

Figure VI.1 – Shape memory cycle steps.

The SM properties of the materials were described by the strain recovery ratio, R_R, and the strain fixity ratio, R_f. Both can be determined according to Equation VI.3 and Equation VI.4:

$$R_r(\%) = \frac{L_m - L_{Res}}{L_m - L_o} \times 100 \quad \text{(VI.3)}$$

$$R_f(\%) = \frac{L_{Ret} - L_o}{L_m - L_o} \times 100 \quad \text{(VI.4)}$$

where: L_o is the original length, L_m is the deformed length, L_{ret} is retained length and L_{res} is the length after the recover.

VI.3 – Results and discussion

In DSC analysis, the width of transition zone provides a qualitative measure of phase homogeneity, and the variation in the magnitude of T_g can indicate the degree of microphase separation [6]. In the first heating run, Figure VI.2(a), it is observed, for PU-B and PU-C, a first order transition around 45°C corresponding to a melting endotherm. Neither the melting endothermic peak, associated with the crystalline fraction, nor a crystallization peak were observed during the second heating run or in the cooling run respectively. The episode might be consequence of fast heating/cooling rates employed during the subsequent runs. In the cooling run, Figure VI.2(b), it is observed a glass transition around –60°C. From T_g data, it is found a linear correlation between glass transition temperature and $W(HS)$, Figure VI.2(c). It means that higher contents of hard segment led to higher concentration of hard segment dissolved within soft domain. According to DSC results, the degree of phase miscibility of obtained PUs is: PU-A>PU-B>PU-C.

The effect of hydrogen-bonding on the microphase separation of obtained PUs according to FTIR results was discussed in previous works, Chapter II. All obtained PUs showed an endothermic inflection centered at T_1 associated with the hard segment domain. According to Seymour and Cooper [8], the endotherm region observed in the DSC for PUs may all be ascribed to a morphological effect, and it is a function of hard segment length. Clusters of shorter hard segments give rise to lower temperature endotherms [6, 8]. Thermal properties are summarized in Table VI.2.

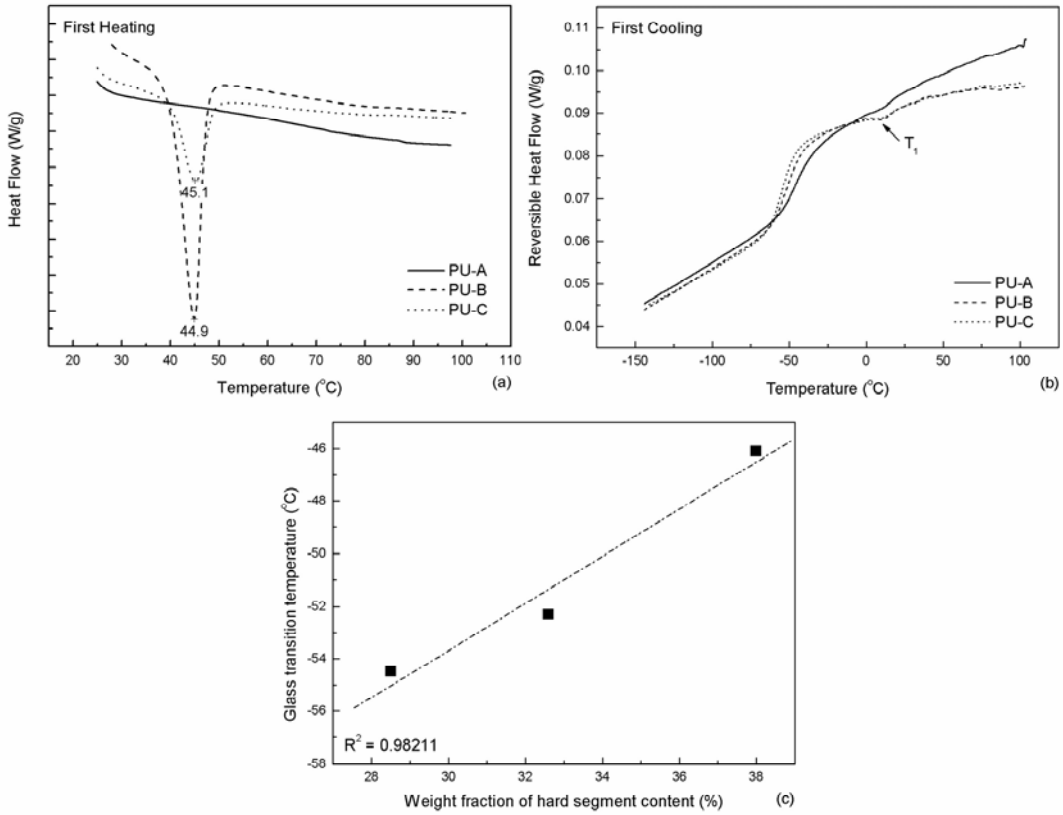

Figure VI.2 – DSC curves of the obtained PUs: (a) first heating (b) first cooling and (c) influence of W(HS) (%) on glass transition temperature.

Table VI.2 – DSC results of obtained poly(ester urethane).

	T_g (°C)	T_{onset} (°C)	T_{end} (°C)	Zone width	T_1 (°C)	T_m (°C)
PU-A	–46.1	–53.8	–33.6	20.2	19.0	–
PU-B	–52.3	–58.2	–42.4	15.8	21.9	44.9
PU-C	–54.5	–59.6	–46.4	13.2	15.4	45.1

DMA is an important technique capable of providing considerable information on the position of transitions and the thermomechanical properties of polymers [9]. The storage modulus, E', and tanδ of obtained PUs are shown, respectively, in Figure VI.3(a) and Figure VI.3(b).

DMA results indicate that SM properties of the obtained PUs can be ascribed to the molecular motion of the soft segments. It can be seen two significant drops in E' for all

samples during heating, that are ascribed to the soft segment phase glass and melting transitions. Below the glass transition, the glass state modulus increases with increasing hard segment content. This is due to the greater phase mixture and the strong interactions among amorphous hard domain in the glass state. Moreover, the almost complete amorphous structure of PU-A collaborates to its higher glassy-state modulus. Regarding shape memory properties, a larger glass modulus is desired in the sense that it gives larger shape fixity upon cooling [4]. After the melting transition, the storage modulus of the PU-C decreases with increasing temperature. However, PU-A and PU-B storage moduli increase. Above the soft-segment melting transition, the storage modulus is strongly dependent of the hydrogen bonding among hard segments. The hydrogen bonding generate a reinforcing effect which contributes to enhancement of the rubbery modulus plateau [10-12]. Thus, after the melting transition, the storage modulus is controlled by the hard segment content. Below the soft segments melting point, the partially crystalline state of soft domain together with the interaction among amorphous hard domain in the rubber state ensures higher storage modulus of PU-C [12]. The tanδ curves in Figure VI.3(b) shows a greater and sharper glass transition for PU-A indicating that the miscibility between the soft segments and the hard segments is more pronounced. As the temperature increases above the melting of soft segment, the damping abruptly increases especially for PU-B because of the higher soft segment content and the higher crystalline fraction.

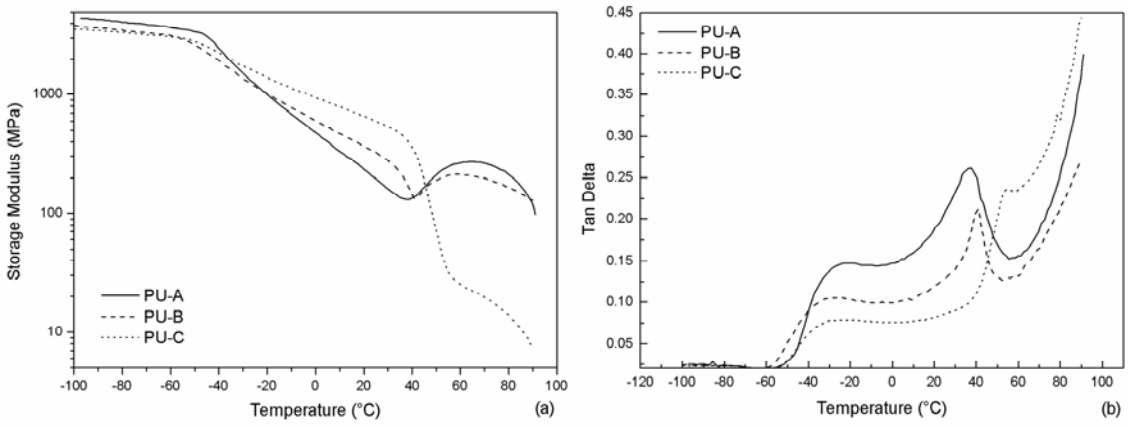

Figure VI.3 - (a) Storage modulus and (b) tanδ of PUs.

Figure VI.4 illustrates SAXS pattern of obtained PU during different stages of shape-memory cycle: permanent shape, Step-3 and Step-4. SAXS measures the scattering intensity as a function of the incident X-ray beam stopper. At Figure VI.4(b), it is observed two maxima occurring along the stretching direction on both sides of the beam. The maxima are due to the scattering from the oriented structure formed during deformation process [13] thereby crystallization. During Step-4 of the shape memory cycle, the PUs patterns recovered the original non-oriented structure.

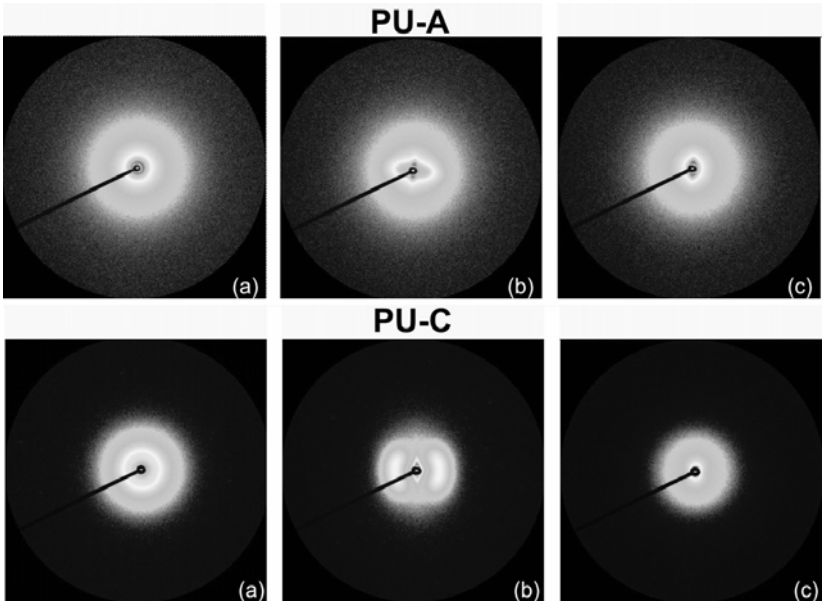

Figure VI.4 – SAXS pattern of: (a) permanent shape, (b) Step-3, (c) Step-4.

To estimate the overall degree of phase separation, it was employ the Lorentz correction, the invariant quantity, Q_{inv}, which is obtained by integrating $I_{(q)}q^2$ over the range of scattering angles, Equation VI.4 [14-16].

$$Q_{inv} = \int_0^{\infty} I_{(q)} q^2 dq \qquad \text{(VI.4)}$$

The obtained PUs are a three-phase structure including: amorphous matrix, hard domains and crystals. The contribution of each phase to the Lorentz corrected SAXS patterns were separated by a deconvolution procedure. Figure VI.5 illustrates the deconvoluted SAXS data during different stages of shape-memory thermomechanical

cycle. Q_{inv} of each phase was obtained as fraction of the total area. Table VI.3 summarizes the results.

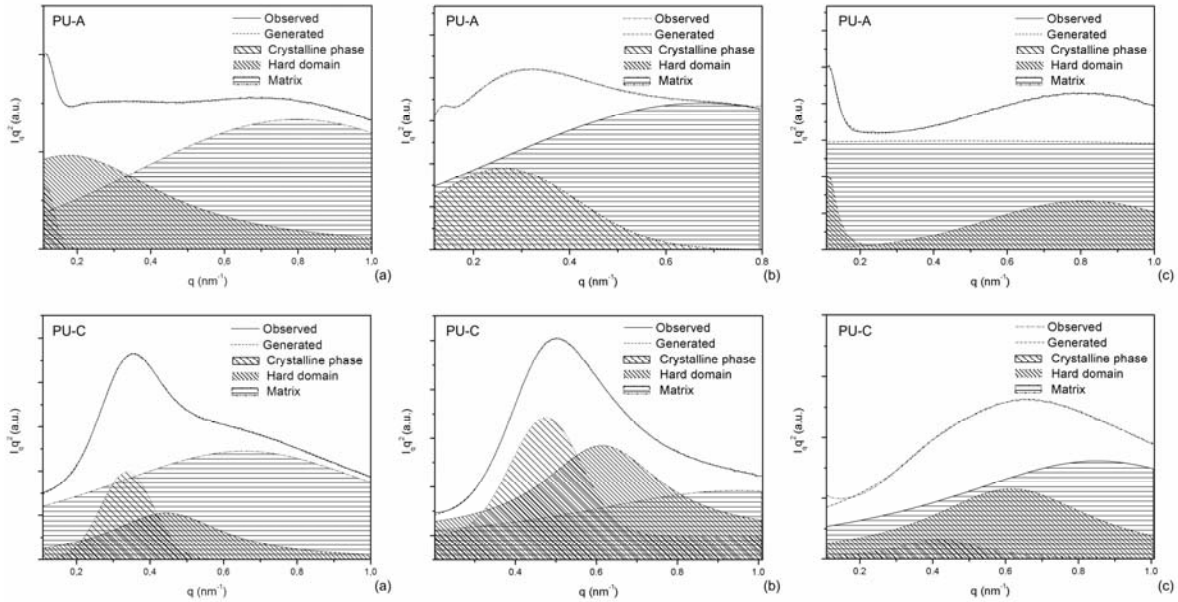

Figure VI.5 – Deconvoluted Lorentz SAXS pattern of PU-A and PU-C: (a) permanent shape, (b) Step-3, and (c) Step-4

Table VI.3 – Deconvoluted SAXS results

		Permanent Shape		Step-3		Step-4	
		Q_{inv} (%)	L (nm)	Q_{inv} (%)	L (nm)	Q_{inv} (%)	L (nm)
PU-A	matrix	66.80	–	75.35	–	77.44	–
	domains	31.48	36.0	24.03	22.5	19.79	7.7
	crystals	1.72	55.3	0.62	48.1	2.77	55.3
PU-C	matrix	68.96	–	25.65	–	58.15	–
	domains	17.50	14.2	43.82	10.2	35.58	10.2
	crystals	13.53	18.6	30.52	13.2	6.27	15.1

Ratio		Initial	Step-3	Step-4
Matrix / Disperse phase	PU-A	2.01	3.06	3.43
	PU-C	2.22	0.35	1.38

Table VI.4 summarizes the values for the mechanical and SM properties. The average of 3 measurements was obtained.

Table VI.4 – Mechanical and shape memory properties of PU-A, PU-B and PU-C.

PU	σ_m (MPa)	ε_m (%)	E (MPa)	Resilience (MJ/m^3)	Toughness (MJ/m^3)	R_f (%)	R_R (%)
A	16.5±0.4	768±61	3.3±0.6	5.6±0.2	1467±176	14±0.8	92.9±0.3
B	20.7±2	1053±45	2.4±0.4	5.9±0.8	2288±270	20±0.5	94.0±0.1
C	22.5±2	1211±41	2.1±0.6	7.8 ±2.7	2831±337	31.±2.2	98.2±0.8

The deformation induces changes in the phase proportion of PU-C, promoting crystallization and phase separation. However, crystallization is not observed at PU-A after Step-3. The implications to SM properties are discussed later. Neither PU-A nor PU-C are efficient to recover the original ratio between matrix and disperse phase after Step-4. However, PU-C promotes more recovery after Step-3. The PU-C ratio changes from 0.35 to 1.38 while PU-A ratio changes from 3.06 to 3.43. The disperse phase is formed by the hard domains and the crystals.

It is clear that an increase in $W(HS)$ produced a decrease in strain and stress at rupture and an increase in modulus (Table VI.4). These results show that the mechanical properties of PUs are highly dependent on the hard segment content, which agree well with previous reports [17-19]. Hard segments can bind themselves via hydrogen bonds that results in an enhancement in the stiffness, however, it prevents chain slippage, reducing strain.

The efficiency of a shape memory polymer is empirically controlled by the polymer's chemical structure, molar mass, degree of cross-linking, and fraction of amorphous and crystalline domains [20]. For the presently studied PUs, entanglement, hydrogen bonding and crystals were used as a fixed structure memorizing the original shape. The development of the new physical entanglements (temporary bonds) between the

polymeric chains and the creation of new crystals were used as metastable structure to maintain the deformed shape in a stable manner. As seen in Figure VI.4(b) and Table VI.3, PU-A is less efficient than PU-C to promote crystallization during chain slippage. When the deformation is applied to the PU-A specimen, polymer chains will align to the extension direction, however, PU-A high degree of phase mixture hinders the formation of new crystals and so the metastable structure development. Therefore, PU-A R_f values are smaller then PU-C. Nevertheless, upon removing the strains at Step-3 low values of strain fixity ratio are observed for all obtained PUs. Different factors, derived from the SM cycle configuration, may have contributed to the present results. These factors are discussed in Chapter IV. As seen in Table VI.4, all of the samples tested showed more than 90% shape recovery at each hard segment contents. The reversible phase was designed to actuate during the softening of soft domains or the melting of crystallites. However, shape recovery of obtained PUs is also highly dependent on the hydrogen-bonding. As observed at Figure VI.3, after the melting transition, strong interactions among hard segments provide enough energy to restore the polymer back to the original shape.

Additionally, higher forces are applied during a low temperature cycle and plastic deformation occurs during the Step-3. It is interesting to notice that the values of toughness in Table VI.4 may be also correlated to R_f or R_R. In the present study, crystallization occurs during deformation, preventing the movement of the polymeric chains, increasing, thereby, the energy absorbed during deformation. This mechanism is important to set the temporary shape and to recover the original shape since it represents the stored energy thus the driving force to guide the system to restore its original structure after being deformed.

VI.4 – Conclusions

Shape memory properties of obtained PUs can be ascribed to the molecular motion of the soft segments. Recovery and fixating were driven by the hydrogen bonding and the crystallization. PU-A poor shape memory results may be related to the high degree of phase miscibility which hinder the polymeric chain movement and restrict

crystallization. SAXS results showed also that the ability to recover shape is related to facility of specific macromolecular architectures to have their nanostructure rebuilt after the shape memory cycle.

VI.5 – Acknowledgments

The authors acknowledge the financial support from the following institutions: National Council for Scientific and Technological Development (CNPq), a foundation linked to the Ministry of Science and Technology (MCT) of the Brazilian Government; the State of Minas Gerais Research Foundation (FAPEMIG); and the National Synchrotron Light Laboratory (LNLS-Brazil) for the use of the SAXS beamline facilities.

VI.6 – References

1 – Lendlein A, Langer R. Science 2002;296(5573):1673–6.

2 – Gall K, Dunn ML, Liu YP, Stefanic G, Balzar. Appl Polym Sci 2004, 85(2):290–2.

3 – Gall K, Kreiner P, Turner D, Hulse M. J Micro Sys 2004, 13(3): 472-83

4 – Kim BK, Lee SY, Xu M. Polymer 1996;37(26):5781–93.

5 – Pereira IM, Patrício PSO, Oréfice RL in: 9º Congresso Brasileiro de Polímeros, Campina Grande, 2007, Vol. 1, 46.

6 – Bao H, Zhang Z, Ying S. Polymer 1996;37(13):2751–4.

7 – Pereira IM, Carvalho S, Pereira MM, Leite MF, Oréfice RL J Appl Polym Sci 2009; Published Online: Jun 2 2009 DOI: 10.1002/app.30404.

8 – Seymour RW, Cooper RL. Macromolecules 1973;6:48–53.

9 – Mondal S, Hu JL. Polym Int 2006;55:1013–20.

10 – Kim BK, Shin JS, Cho SM, Jeong HM. J Polym Sci Phys 2000;38:2652-7.

11 – Meng Q, Hu JL, Zhu Y, Lu J, Liu Y. Smart Mater Struct 2007;16:1192–7.

12 – Zhu Y, Hu JL, Yeung Kw, Choi Kf, Liu Y, Liem H. Appl Polym Sci 2007;103:545-56.

13 – Jiang ZY, Tang YJ, Men YF, et al. Macromolecules 2007;40(20):7263–9.

14 – Chang SL, Yu TL, Huang CC, et al. Polymer 1998;39(15):3479–89.

15 – Wang SH, Zhang Y, Ren WT, et al. Polymer Testing 2005;24(6):766–74.

16 – Li YJ, Kang WX, Stoffer JO, et al. Macromolecules 1994;27(2):612–4.

17 – Liu Y, Pan C. Eur Polym J 1998;34(5-6):621–4.

18 – Nakamae K, Nishino T, Asaoka S, et al. Int J Adhes Adhes 1999;19(5):345–51.

19 – Pompe G, Pohlers A, Pötschke P, Pionteck J. Polymer 1998;39(21):5147–53.

20 – Miaudet P, Derre A, Maugey M, et al. Science 2007;318:1294–6.

Chapter VII (Capítulo VII)
The morphology and phase mixing studies on poly(ester urethane) during shape memory cycle

I. M. Pereira[1,2]; R. L. Oréfice[2*]

[a]Federal Center of Technological Education of Minas Gerais, Timoteo, Brazil
[b]Federal University of Minas Gerais, Department of Metallurgical and Materials Engineering, Belo Horizonte, Brazil

Abstract:

Three series of shape memory poly(ester-urethane) with varying hard-segment content were synthesized. The materials were designed to display a three-phase structure consisting of a disperse phase formed by crystallites and hard domains embedded in an amorphous matrix. The initial undeformed morphology was investigated using techniques such as: modulated differential scanning calorimetry (DSC), fourier transform infrared (FTIR) and wide angle X-ray scattering (WAXS). These techniques established the phase separation, the hydrogen-bonding structure and the crystalline fraction of specimen prior to the thermo-mechanical treatments. Values subsidized the small angle X-ray scattering (SAXS) investigations of morphological changes during shape memory cycle. The deformation cycle led to the formation of an oriented nano-structure derived from chain alignment. The nano-structure recovered was observed to be triggered by the melting of the crystallites and bulk incompatibility. A relationship between the ability of the studied poly(ester-urethane) to recover their original shape and their original nanostructure was determined.

Keywords: Polyurethane; Shape Memory; Phase mixture; SAXS.

VII.1 – Introduction

Polyurethanes (PUs) are one of the most important classes of special polymers that comprise a diverse family [1]. Linear segmented thermoplastic PU elastomers are polyurethanes characterized by having the chain backbone arranged as a block copolymer. The properties of these materials are dependent of the two- or the polyphase morphology. On the other hand, the morphology and the structure are dependent on the chemical composition and on the length of the segments, and so forth. In general, segmented PUs have soft and hard segments. The soft segments display high mobility, are usually presented in coiled conformation and are alternated with units of hard segments [2]. Due to the incompatibility between the hard and soft segments, segmented PUs elastomers can microphase separate to form hard and soft domains [3,4]. Recent approaches have tailored PUs properties to yield thermo-responsive materials, described as shape memory polymers (SMP), with the ability to memorize a permanent shape that can substantially differ from their initial temporary shape [5].Generally, SMP can be thought of as a material with morphology consisting of two phases: a shape fixing matrix phase and a shape memorizing dispersed phase. Above the actuation transition of the shape fixing phase, the polymer can be deformed from its primary shape to a secondary shape by the application of stress, and then locked into the secondary shape by cooling to below the actuation transition [6]. The efficiency of a shape memory polymer is empirically controlled by the polymer's chemical structure, molecular weight, degree of cross-linking, and fraction of amorphous and crystalline domains [7].

Although some research have been done in the past [8,9], the details of the morphological changes during shape memory cycle are still poor understood, mainly because segmented PUs exhibit a complex phase structure depending on the type and size of segments used as well as on the processing conditions. Furthermore, these features impact not only the shape memory properties but also the physical properties. Hence, understanding the correlation between the chemical and morphological structures with the shape memory properties is essential in designing SMPs for practical applications.

Therefore, this study aims to identify the role of the chemical and the morphological structures of PU´s during shape memory cycle. DSC, WAXS and FTIR were used to study the morphology features. Additionally, mechanical properties and shape memory properties were determined and discussed in relation to the results of WAXS and FTIR. Finally, SAXS measurements were carried out to investigate the structural changes during shape memory cycle.

VII.2 – Materials and Methods

A – Materials

Poly(caprolactone diol) (PCL M_n = 530, 10000 g mol^{-1}), isophorone diisocyanate (IPDI), 2,2-bis(hydroxymethyl) propionic acid (DMPA) and dibutyl tin dilaurate (DBDLT) were obtained from Aldrich. Triethylamine (TEA, 98%) and hydrazine (HZ, 25%) were purchased from Vetec. All these chemicals were employed throughout this work without any previous treatment.

B – Prepolymer synthesis

PUs were prepared by the prepolymer mixing method, using a 250mL three neck glass flask equipped with a heating mantel, a mechanical stirrer and a thermometer. The PCL and DMPA were stirred in the glass reactor at 65^{o}C for 30min. IPDI was added to the reactor in the presence of DBDLT (NCO/OH ratio of 2) under N_2 atmosphere. The reaction was carried out at 70–75^{o}C for 3hs.

C – Neutralization of the prepolymer

After cooling down to 40^{o}C the prepolymer, the carboxylic acid groups were neutralized by the addition of TEA. The mixture was then gentle stirred for 40min.

D – Dispersion and chain extension

The dispersion in water and PU chain extension were obtained by adding HZ and deionized water to the neutralized prepolymer under high-speed stirring. To ensure that

the reaction was completed, the mixture was stirred for 30min. This chemical procedure was successful in producing PUs water dispersions with solid content about 30% (PUs). The feed ratios are shown in Table VII.1.

Table VII.1 – Composition (wt. %) of waterborne PUs.

Sample	PCL		DMPA	IPDI	HZ	TEA
	530	10000				
PU-I	18.78	–	3.59	27.63	1.99	2.70
PU-II	5.59	56.82	1.64	12.66	0.91	1.24
PU-III	–	64.33	0.65	5.02	0.36	0.49

where $W(HS)$ is weight fraction of hard segment, obtained according to Equation VII.1:

$$W(HS) = \frac{Weight_{IPDI} + Weight_{HZ}}{Weight_{PU}} \times 100 \qquad \text{(VII.1)}$$

E – Film formation

Films were produced by casting the dispersions in a PVC mold and allowing them to dry at 17^{o}C for one week. The films were then annealed at 80^{o}C for 72h.

F – Infrared spectroscopy

Infrared spectra were collected at room temperature in a Fourier transform infrared spectrophotometer (FTIR; Perkin–Elmer, model Spectrum 1000). Measurements were carried out using the attenuated total reflectance (ATR) technique. Each spectrum was a result of 64 scans with a resolution of 4 cm^{-1}.

G – Wide angle X-ray scattering (WAXS)

Wide angle X-ray scattering (WAXS) analysis was performed in samples having 0.8–1.0mm in thickness and 14mm in diameter using a Philips, model PW1710 diffractometer operated with CuK_α irradiation at a scan rate of 2º 2θ/s in the range of 5 to 60º.

H – Thermal Analysis

Modulated differential scanning calorimetry (DSC) measurements were performed using a TA Instruments 2920. The following protocol was applied to each sample: (1) heating from room temperature to 110°C at 15°C min^{-1}, (2) holding for 3.00min at 110°C, (3) cooling to -110°C at 3.00°C/min, modulating +/- 1.00°C every 60 seconds, (4) holding for 3.00min at -110°C and (5) heating again to 110°C with 3.00°C/min modulating +/- 1.00°C every 60 seconds. Data were collected from the first cooling and second heating. The melting and the re-crystallization temperatures were taken as peak maxima, the glass transition temperature (T_g) and the enthalpies of the melting peaks were obtained by the analyzing software of the calorimeter.

I – Mechanical Properties

The tensile strength (σ_m), initial modulus (E) and elongation at break (ε_m) of the samples (DIN60) were measured using a universal testing machine (DL3000, EMIC) at 10mm/min crosshead speed. The sample length between the clamps was 20mm. The tests were performed at room temperature.

J – Shape memory properties (SM)

Shape memory experiments were done using a universal testing machine (DL3000, EMIC), having a constant temperature heating device. Specimens were heated using a fluorescent lamp, and cooled by cold water. A thermocouple was attached to the specimen to control its temperature. Specimens were deformed at 10 mm/min crosshead speed. Scheme VII.1 exemplifies the heating and cooling system.

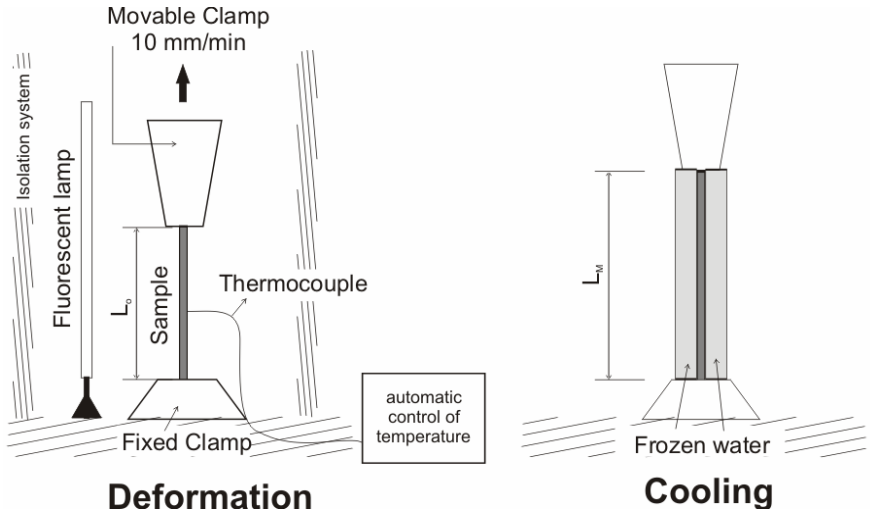

Scheme VII.1 – Shape memory test set-ups.

A shape recovery cycle consisted of the following steps: (1) Samples were deformed to a defined strain, L_m, at 80°C. (2) While maintaining the strain at L_m, samples were cooled to room temperature. (3) Mechanical constraints on the polymers were removed. (4) The samples were subsequently heated to 80°C in an oven, and stayed at this temperature for l5min to recover its original shape. This completes one thermomechanical cycle leaving a residual strain. Scheme VII.2 illustrates a shape-memory thermomechanical cycle test.

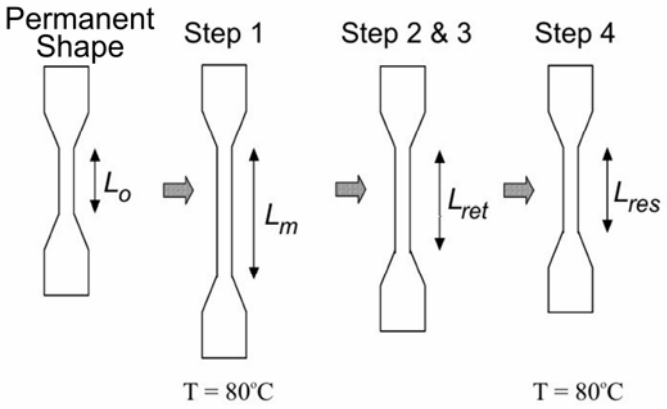

Scheme VII.2 – Thermomechanical shape memory cycle.

The loading stage of the thermomechanical cycle test defines a stress–strain curve. The SM properties of the materials were described by the strain recovery ratio, R_R, and the strain fixity ratio, R_f. Both can be determined according to Equation VII.2 and Equation VII.3:

$$R_r(\%) = \frac{L_m - L_{Res}}{L_m - L_o} \times 100 \qquad \text{(VII.2)}$$

$$R_f(\%) = \frac{L_{Ret} - L_o}{L_m - L_o} \times 100 \qquad \text{(VII.3)}$$

where: L_o is the original length, L_m is the deformed length, L_{ret} is retained length and L_{res} is the length after the recover. Values of L_m close to 22mm were used.

K – Synchrotron small angle X-ray scattering (SAXS)

SAXS measurements of synchrotron small angle X-ray scattering were performed using the beam line of the National Synchrotron Light Laboratory (LNLS, Campinas, Brazil). After passing through a thin beryllium window, the beam is monochromatized ($\lambda = 1.488$Å) and horizontally focused by a cylindrically bent and asymmetrically cut silicon single crystal. The X-ray scattering intensity, $I_{(q)}$, was experimentally determined as a function of the scattering vector, q, whose modulus is given by Equation VII.4:

$$q = \frac{4\pi}{\lambda} \sin\theta \qquad \text{(VII.4)}$$

where λ is the X-ray wavelength and θ being half the scattering angle. Each SAXS pattern corresponds to a data collection time of 900 s. From the experimental scattering intensity produced by all the studied samples, the parasitic scattering intensity produced

by the collimating slits was subtracted. All SAXS patterns were corrected for the non-constant sensitivity of the position sensitive X-ray detector, for the time varying intensity of the direct synchrotron beam and for differences in sample thickness. Because of the normalization procedure, the SAXS intensity was determined for all samples in the same arbitrary units so that they can be directly compared. The sample-detector distance of 551.6 mm was used during the measurements.

VII.3 – Results and discussion

A – Thermal Analysis

The thermal behavior of the obtained PUs is shown in Figure VII.1(a) during cooling and in Figure VII.1(b) during the second heating. Thermal properties are summarized in Table VII.2.

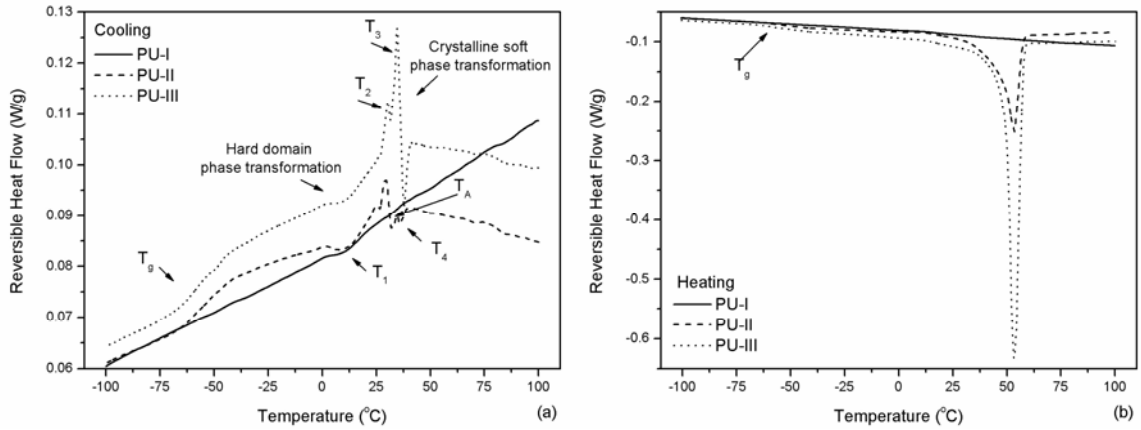

Figure VII.1 – DSC curves for obtained PUs: (a) cooling and (b) heating

Table VII.2 – DSC results of obtained poly(ester urethane).

	T_g (°C)	T_{onset} (°C)	T_{end} (°C)	Zone width	T_1 (°C)	T_2(°C)	T_A(°C)	T_3 (°C)	T_4 (°C)	C_P (J/g)
PU-I	–	–	–	–	8.9	–	–	–	–	–
PU-II	-57.7	-64.7	-45.5	19.1	7.7	24.8	28.9	34.6	53.5	127.8
PU-III	-60.2	-64.1	-53.1	11.0	8.4	30.4	–	34.6	53.3	179.0

High molar mass PCL has a glass transition at –60°C, a first order transition at 69.8°C corresponding to a melting endotherm, an exothermic crystallization peak around 25°C and crystallization heat of 16.9 kJ.mol^{-1}[10,11].

In DSC analysis, the width of transition zone provides a qualitative measure of phase homogeneity, and the variation in the magnitude of T_g can indicate the degree of microphase separation [12]. In the cooling run, Figure VII.1(a), it is observed for PU-II and PU-III a glass transition around –60°C. From T_g data, Table VII.2, it is found that the PU-II glass transition temperature is higher than PU-III. It means that higher amount of hard segment dissolves in PU-II soft domain, resulting in an increase in the soft-segment glass transition temperature. In addition to the increase in T_g values, the broadening of the width of the transition zone is observed, suggesting as well higher degree of phase mixture in PU-II. All obtained PUs showed an endothermic inflection centered at T_1 associated with the hard segment domain. According to Seymour and Cooper [13], the endotherm region observed in the DSC, for PUs may all be ascribed to a morphological effect, and it is a function of hard segment length. Clusters of shorter hard segments give rise to lower temperature endotherm [12, 13]. On cooling, PU-II and PU-III recrystallized to a certain extent. During recrystallization, PU-II displayed three exothermic peaks T_2, T_3 and T_A while PU-III displayed only two: T_2 and T_3. The difference could be to the unlike crystal structure of PU-II and PU-III.

During second heating, PU-I showed a smooth baseline whereas PU-II and PU-III showed a glass transition and an endothermic inflection centered at T_4 assigned to melting of crystalline soft segment phase. The endotherm maxima were observed below the 69.8°C given for pure high molecular weight PCL. This reduction could be due to the mixing of hard phase or/and to the imperfections in the crystal packing hence, the phase mixture not only disturbs crystallization, reducing the crystal fraction but also promotes the formation of less perfect crystals which need less energy to melt. The data evidences the complex phase morphology of the obtained PUs which the soft segment forms a continuous matrix with the glass transition temperature around –60°C, and a disperse phase consisted of poorly ordered microregions, possibly containing ionic groups, and well ordered but still not perfect crystallites.

B – Infrared spectroscopy

Typical infrared spectra of PU-I, PU-II and PU-III, that have compositions defined in Table VII.3, are shown in Figure VII.2. The characteristic bands of poly(ester-urethane) are marked in Figure VII.2 and described in Table VII.3 where the band frequency and the correspondent functional group are shown [14,15,16,17,18,19,20,12,21].

Table VII.3 – Origin, the group frequency, and the functional group of spectral bands observed in Figure VII.2.

Item	Origin	Group Frequency Wavenumber (cm^{-1})	Assignment
1	N–H	3600–3150	Primary amine stretching modes
		~3500	Free N–H stretching band
		~3300	Hydrogen bonded N–H band
2	$–CH_3$	3000–2800	Methylene groups stretching modes
			2A – Asymmetric mode
			2B – Symmetric mode
3	C=O	1760–1600	Carbonyl groups stretching vibrations
		1750–1725	Ester stretching modes
		~1720	Free urethane stretching band
		~1700	Hydrogen bonded urethane stretching band
		~1660	Free urea stretching band
		~1630	Hydrogen bonded urea stretching band
4	>N–H	1640–1540	Secondary amide modes
5	$–CH_3$	1470–1430	Methylene groups asymmetric bend modes
6	C–N	1292–1226	Terciary amide stretching modes
7	C–O–C	~1150	Ether stretching vibration

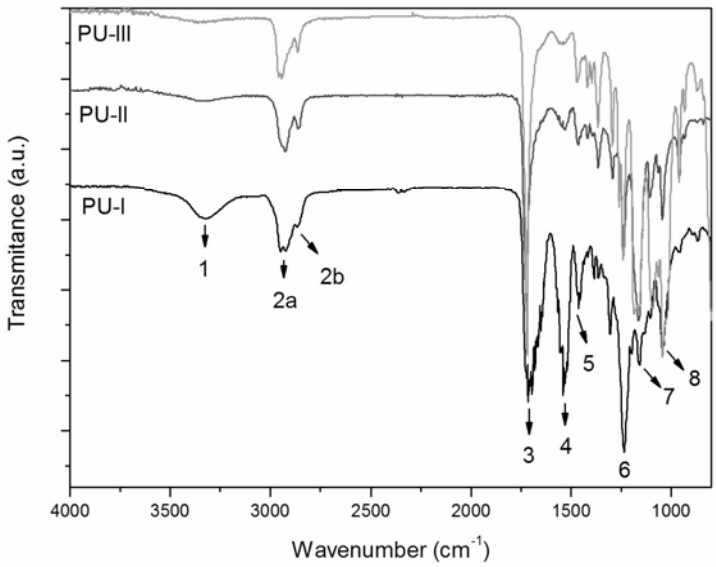

Figure VII.2 – FTIR spectra of PU-I, PU-II and PU-III.

Hydrogen bonding is known as an important driving force for the phase separation of a hard segment from a soft-segment matrix. Two main spectral regions are of interest in studying the hydrogen bonding of segmented PUs: N–H and C=O, respectively, primary amine stretching and carbonyl group stretching. As band overlapping occurs at band 1 and 3, a deconvolution mathematical procedure (by using the PickFiT® software) was performed in spectra of Figure VII.2. Figure VII.3(a), and (b) illustrate, respectively, the deconvolution procedure used to determine the overlapped band 1 and 3 of FTIR spectrum of obtained PUs.

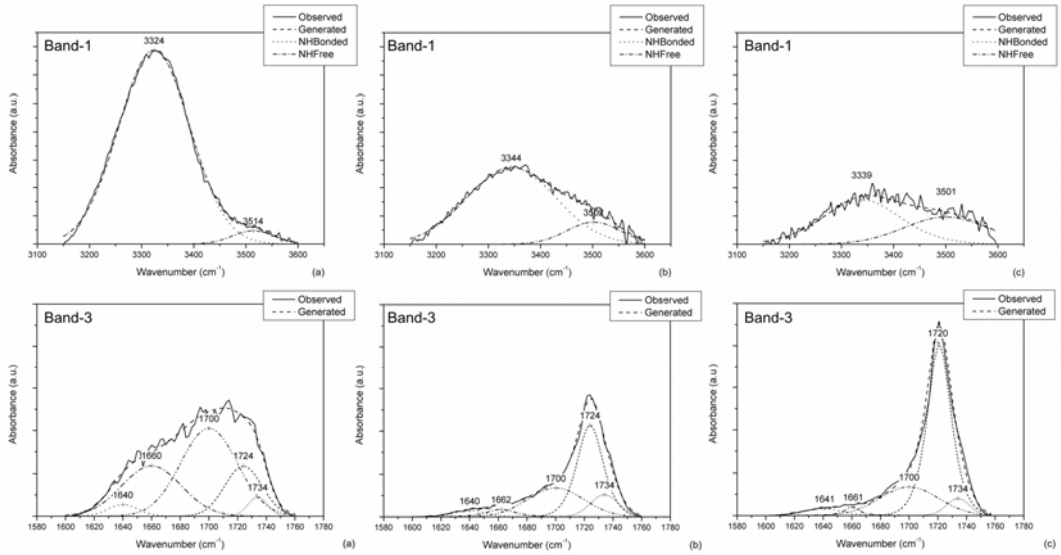

Figure VII.3 – Deconvoluted FTIR spectrum, N–H stretching region, of samples: (a) PU-I, (b) PU-II and (c) PU-III.

N–H bands of PU-I and PU-II are nearly completely hydrogen-bonded. The ratio between the band areas shows, respectively, that 97% and 86% of the NH groups are hydrogen bonded. PU-III, however, has only 64% of hydrogen bonded.

The extent of the carbonyl absorption groups participating in hydrogen bonding could be expressed by a hydrogen-bonding index $HBI(\%)$, which is the fraction of hydrogen bonded in the carbonyl groups stretching vibrations (Equation VII.5) [18,22,23,24].

$$HBI(\%) = \frac{A_{1700} + A_{1640}}{A_{1700} + A_{1640} + A_{1724} + A_{1660}} \times 100 \qquad \text{(VII.5)}$$

where A_{1724}, A_{1700}, A_{1660} and A_{1640} are respectively the FTIR absorption band area of free urethane, bonded urethane, free urea, bonded urea.

The microphase separation structure of PUs depends on many factors, i.e.: structure and molecular weight of the soft segment, nature of chain extender, hard segment content and interactions, thermal and solvent history during sample preparation [25]. The multi-phase structure of PUs was first proposed by Cooper and Tobolsky [26] and is a result of the repulsive interaction between dissimilar segments and thermodynamic immiscibility of hard and soft segments at low temperature [26,27,28].

PU-I, PU-II and PU-III $HBI(\%)$ results are, respectively, 52.1%, 39.8% and 29.8%. DSC results predicts that the degree of phase mixture of PU-I>PU-II>PU-III. The highly hydrogen bonded hard segments of PU-I act as physical cross-links, restricting segmental motion of the polymer chain. However, it does not result in a more significant phase separation between hard and soft segments because the weight fraction of hard segment in PU-I is 3 times larger than PU-II and 7 times larger than PU-III. On the other hand, the lower values of $HBI(\%)$ of PU-II and PU-III do not result in a more extensive phase mixing because of their lower weight fraction of hard segment. Moreover, loser and longer polymer chain are more likely to realign and crystallize, increasing the phase separation. Some previous works [29,30,31] did not consider the

effect of the hard segment content on the phase separation. Nevertheless, *HBI* (%) values alone were not able to predict the phase separation structure of obtained the PUs.

C – Wide angle X-ray scattering (WAXS)

Figure VII.4 shows the WAXS profiles of PUs and PCL10000. The diffraction curve of PU-I is a broad shoulder around $2\theta=20^{o}$, which is typical of noncrystalline state with a characteristic small-scale order (interchain spacing) of 0.4–0.5nm [32,33,34]. The diffraction pattern of PU-II and PU-III are typical of semicrystalline polymers. In PU containing only PCL 530 (i.e. PU-I), the fraction of hard segments is high enough to restrict PCL crystallization, and the high levels of hydrogen-bonding, observed through the FTIR results, also contributes for the stabilization of the amorphous structure.

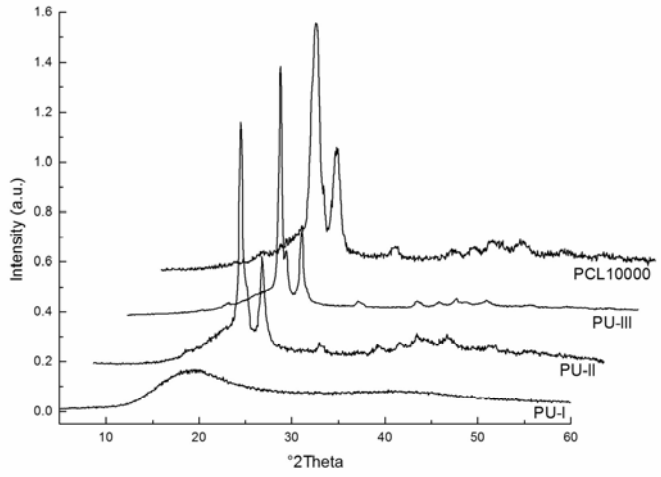

Figure VII.4 – WAXS pattern of obtained poly(ester-urethane) and PCL10000.

The amorphous and crystalline part of PCL10000, PU-II and PU-III were separated by a deconvolution procedure using the PickFiT® software. Gaussian curves were used to describe the amorphous phase and the crystalline reflections. The crystalline peaks were established according to WAXS scattering results. The experimental WAXS results and the deconvoluted separated curves are given in Figure VII.5.

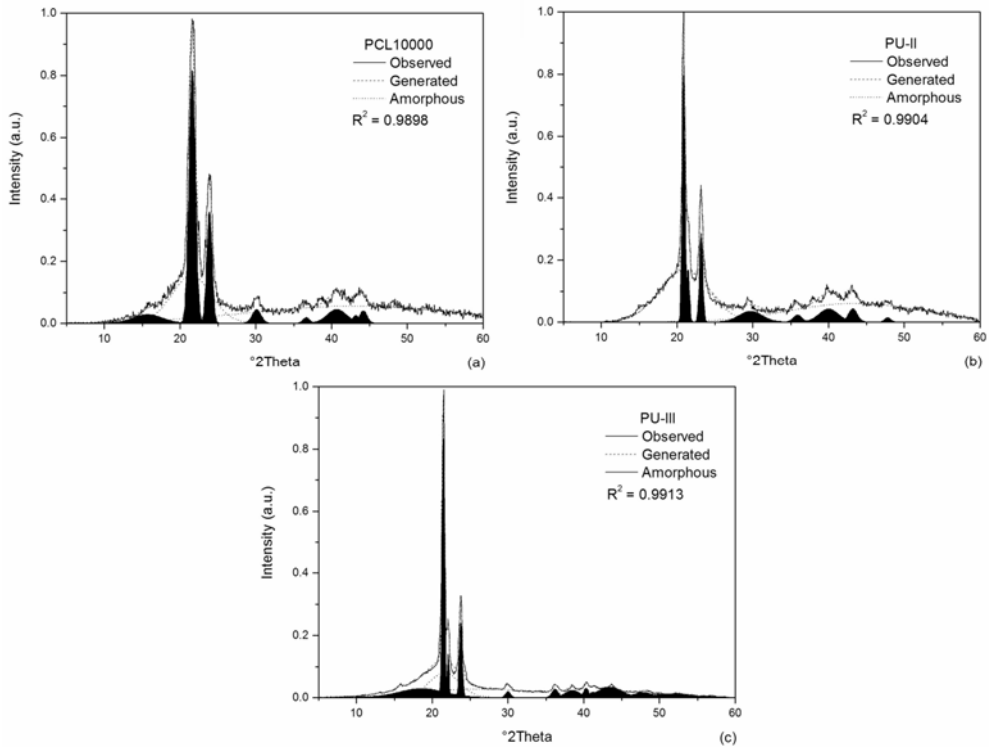

Figure VII.5 – Experimental WAXS curves and its separation in amorphous and crystalline parts: (a) PCL10000, (b) PU-II and (c) PU-III.

The crystallinity index, α_X, is defined as the ratio of the area under the separate crystalline pattern ($\sum A_{crystalline}$) and the total scattering , $\sum A_{crystalline} + \sum A_{amourphous}$, of the original pattern, according to Equation VII.6 [26,35]:

$$\alpha_X = \left[\frac{\sum A_{crystalline}}{\left(\sum A_{crystalline} + \sum A_{amourphous} \right)} \right] \times 100 \qquad \text{(VII.6)}$$

PU-II, PU-III and PCL10000 crystallinity index are, respectively, 27.1%, 54.9% and 34.5%.

It is important to say that the thermal history of PU-III is different form PU-I or PU-II. As PU-III is a brittle polymer, PU-III specimens were stamped at high temperature.

D – Synchrotron small angle X-ray scattering (SAXS)

In this work, SAXS technique was used to provide information regarding the effect of the poly(ester-urethane) macromolecular architecture on the morphology of the polymer and on the microphase separation phenomenon during different stages of the shape memory cycle.

The patterns and intensity distribution of SAXS are dependent on the shape, the size and size distribution of scattering objects. Thus, this technique is suitable for studying the structure of mass fractal aggregates, including primary particles. The angular dependence of the scattering vector is mainly determined by the size of the colloidal particles, their tendency to aggregate, the porosity of the disperse system and the magnitude of the specific surface area [36].

Figure VII.6 illustrates SAXS pattern of PU-I, PU-II and PU-III during three stages: (a) Permanent Shape, (b) Step 3 and (c) Step 4, as illustrated in Scheme VII.2. It is observed two maxima occurring along the stretching direction on both sides of the beam stop for PU-II and PU-III. The maxima are due to the scattering from the oriented structure. The patterns indicate a high degree of orientation obtained from deformation process [37]. During Step 4 of the shape memory cycle, the PUs patterns recovered the original non-oriented structure.

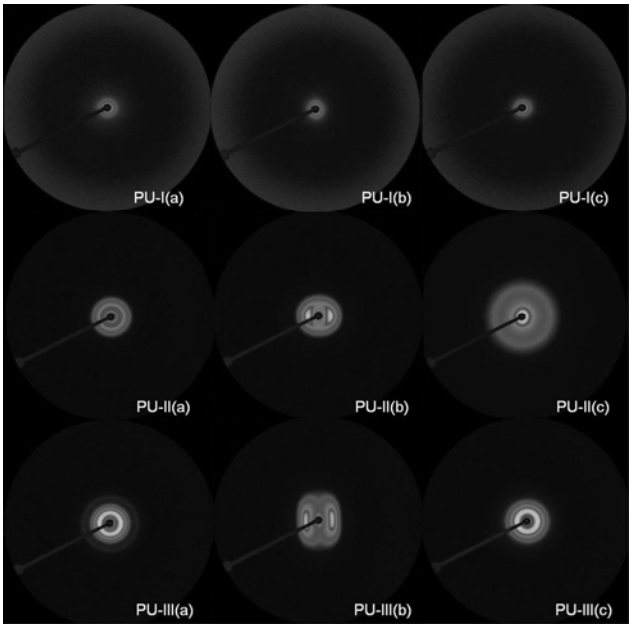

Figure VII.6 – Small angle X-ray scattering patterns of PU-I, PU-II and PU-III during three stages: (a) Permanent Shape, (b) Step 3 and (c) Step 4.

Figure VII.7 illustrates SAXS data of PU-I, PU-II and PU-III as a function of the scattering vector, q. The samples were studied during the same three stages: (a) Permanent Shape, (b) Step 3 and (c) Step 4. In order to allow direct comparison between curves, PU-III data was divided by 10.

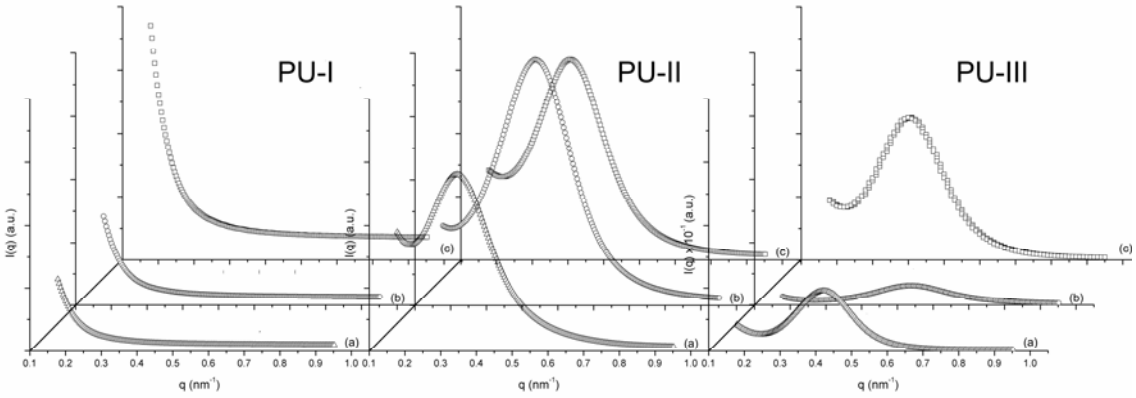

Figure VII.7 – SAXS curves for poly(ester-urethane) samples during different stages of shape memory cycle (a) Permanent Shape, (b) Step 3 and (c) Step 4.

The scattering peak observed in SAXS data of PU-II and PU-III arises due to local heterogeneities in the electron density of the materials and it is usually interpreted as a consequence of the presence of distinct microphases with different electronic densities [36,38,39].

PU-II and PU-III were designed as three-phase structure including: amorphous matrix, hard domains and crystals. In order to discuss the phase separation, it is convenient to employ the Lorentz correction, the invariant quantity, Q_{inv}, which describes the electron density fluctuation of polymer and is a good approximation to estimate the overall degree of phase separation in segmented polymers [38], Q_{inv} can be obtained by integrating $I_{(q)}q^2$ over the range of scattering angles, Equation VII.7 [36,38,39].

$$Q_{inv} = \int_0^\infty I_{(q)} q^2 dq \qquad \text{(VII.7)}$$

Since Equation VII.8 can not be applied to the overall data of PU-II and PU-III during Step 3, because of the anisotropic orientation of the lamellae in the samples [37], the contribution of each phase to the Lorentz corrected SAXS patterns were separated by a

deconvolution procedure. Gaussian curves were used to describe the scattering phenomena due to each phase. As predicted by DSC results, the phases that are responsible for the observed X-ray scattering were: crystalline phase in soft domains, hard domains and the amorphous matrix. As Q_{inv} is obtained by integrating $I_{(q)}q^2$ over the range of scattering angles, phases with higher electronic densities achieve higher integrated values hence the deconvoluted crystalline phase was associated with the phase with higher intensity values.

The experimental results and the deconvoluted separated curves of PU-II during: (a) Permanent Shape, (b) Step 3 and (c) Step 4 are given in Figure VII.8(a). The same procedure was also adopted for PU-III, Figure VII.8(b).

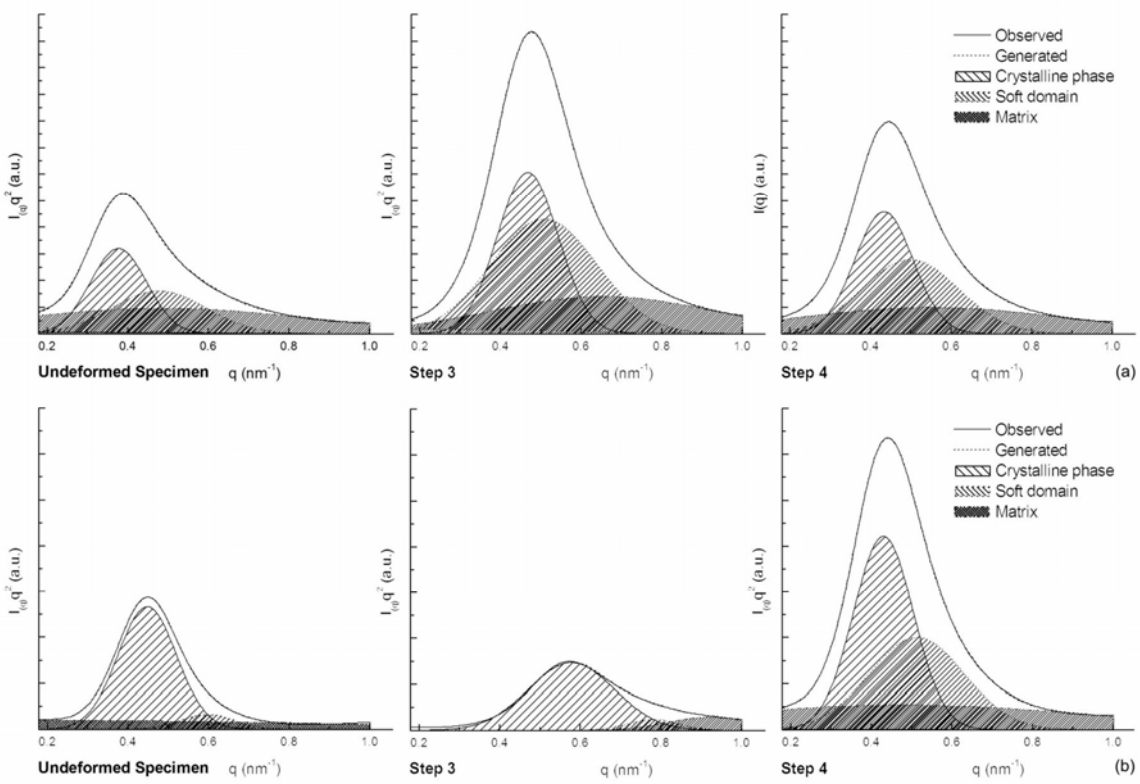

Figure VII.8 – Deconvoluted Lorentz SAXS pattern of samples: (a) PU-II, and (b) PU-III.

Q_{inv} of each phase obtained as fraction of the total area. Figure VII.9 describes the three-phase structure of PU-II and PU-III during the shape memory cycle. Table VII.4 summarizes the results.

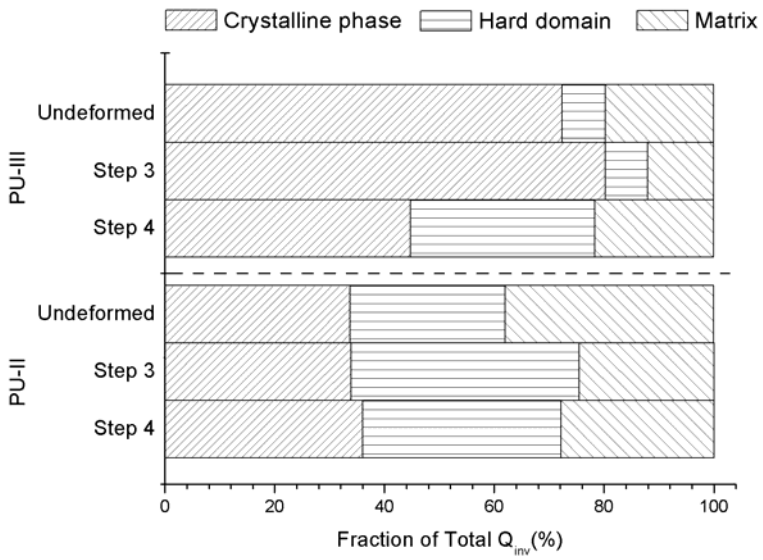

Figure VII.9 – PU-II and PU-III obtained three-phase structure during shape memory cycle.

Table VII.4 – Deconvoluted SAXS results of crystalline phase, hard domains and the amorphous matrix as fraction of the total Q_{inv}.

				Permanent Shape	Step 3	Step 4
PUII	Disperse Phase		Crystalline phase	33.7%	33.9%	36.1%
			Hard Domain	28.3%	41.6%	36.1%
	Matrix			38.0%	24.5%	27.8%
PUIII	Disperse Phase		Crystalline phase	72.4%	80.3%	44.8%
			Hard Domain	7.9%	7.7%	33.6%
	Matrix			19.7%	12.0%	21.7%
Matrix / Disperse phase ratio			PUII	0.61	0.32	0.39
			PUIII	0.25	0.14	0.28
Hard Domain / Crystalline phase ratio			PUII	0.84	1.23	1.00
			PUIII	0.11	0.10	0.75

The permanent shape deconvoluted SAXS results predict that the segmental macromolecular architecture of the PU-II and PU-III is semi-crystalline and the crystalline fraction of PU-I<PU-II<PU-III. Furthermore, SAXS results predict that the

degree of phase separation of PU-I<PU-II<PU-III, in accord with WAXS and DSC results, suggesting that the method is capable of providing information about the polymer morphology.

The inter-domain repeat distance, L_{domain}, or lamellar crystalline repeat distance, $L_{Crystal}$ depend on the molecular length of the polyester soft segment, the number and size of hard domain and also on the lamellar crystalline structure. L can be estimated from the $q_{\max}$ corresponding to the maximum of $I_{(q)}q^2$ versus q curves using Bragg's equation, Equation VII.8 [36,38,39].

$$L = \frac{2\pi}{q_{\max}} \tag{8}$$

Figure VII.10 describes the inter-domain repeat distance, and the lamellar crystalline repeat distance of PU-II and PU-III during the shape memory cycle derived from the deconvoluted curves in Figure VII.10. Variations in the repeat distances observed in Figure VII.10 can be related to the proportion of the phases determined in Figure VII.11, i.e., phases with high contents display shorter interdomain and/or intercrystallite distances. Previous results [38,39] reported similar inter-lamellar repeated distances, varying from 12-16nm.

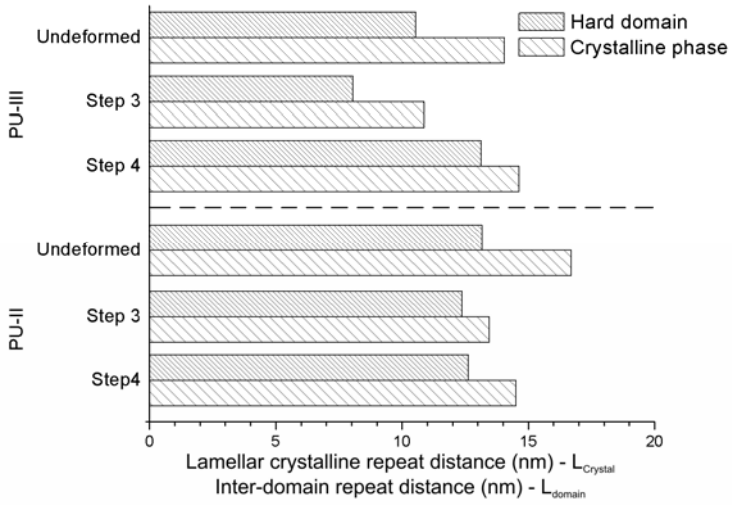

Figure VII.10 – Inter-domain repeat distance and lamellar crystalline repeat distance of PU-II and PU-III during shape memory cycle.

The shape memory cycle induces changes in the phase proportion. Deformation promoted crystallization and phase separation. Recovery, however, does not modify appreciably PU-II structure. The presence of PCL530 in soft segments would restrict chain packing efficiency of PU-II, resulting in the formation of a less perfect crystal structure.

In SMPs, the relative motion and rearrangement of molecular chains is the primary inelastic strain mechanism responsible for the shape-memory effect. The establishment and the annihilation of a metastable structure store and recover the deformation during the SM cycle [8,9]. In the present work, the metastable structure formed during deformation, the disperse phase, stores the temporary shape in a stable manner and provides to the system a lower entropy storage mechanism. To recover the initial shape, the disperse phase melting drives the individual chains toward to their initial position.

Figures VII.6 and VII.7 indicate that there is a relationship between the ability of the studied PUs to recover their original shape after a sequence of thermo-mechanical treatments (that will be discussed later) and the ability to recover their original nanostructure. It is also possible to realize that this ability to recover the original nanostructure is less pronounced in PU-II because PU-II would not have enough driving force to guide the system to restore its original structure after being deformed. This observation correlates well with the results obtained by measuring the shape memory properties of the samples, as it will be reported later. Figure VII.9 indicates that PU-III disperse phase, hard domains and the crystalline phase, are more efficient to memorize the initial disperse phase because the ratio between matrix and disperse phase does not significantly change after the shape memory cycle even though the shape recovery brings major changes to PU-III ratio between hard domain and crystalline phase, Table VII.4. Thereby, PUIII is more efficient to recover the original shape, indicating that recovery is not only related to the composition of the disperse phase but also to its ability to reorganize during entropic recovery to more stable energy stages. Unlike PU-II, deformation promotes the crystallization of PU-III soft segment.

During recovery, the crystals melt and enrich the matrix phase with soft segments. As consequence, in the matrix bulk, the repulsive interaction between the dissimilar hard and soft segments increases, increasing their immiscibility and leading to hard domain segregation. Moreover, FTIR results suggest that, for the obtained PUs, phase separation is not only controlled by the interactions among hard domains, the bulk immiscibility and chain mobility also control the partition between hard domain and crystal and, at recovery temperature, chain mobility, due to the system extra energy, and bulk incompatibility, because of soft phase melting, are at higher level. The same is not observed for PU-II mainly because its different crystal structure where the presence of PCL530 soft segments reduce the polymeric chain ability to rearrange.

As predicted by FTIR results, due to soft segment macromolecular architecture of PU-I, $HBI(\%)$ and $W(HS)$, a high degree of phase mixing between hard and soft segments was observed. Therefore, the scattering intensity of PU-I in Figure VII.10 decreases monotonically with q. The monotonically decreasing profile of PU-I suggests the Guinier plot for an isolated domain system at very high dilution [36,40]. In this case, the particle system is made up of many particles with different sizes. This results in the experimental curve departing from linearity and becoming concave at higher values of q. The size of dispersion particles can be calculated by Guinier's method if the distance between particles is much larger than the particle size. In most cases, the shape of the particles is unknown [36].

By Guinier's method, the dependence of SAXS intensity, $I_{(q)}$, on scattering angle can be described by the following relationship, Equation VII.9 [36].

$$I_{(q)} = I_e n^2 N \exp\left(-\frac{4\pi^2\phi^2 R_o^{\,2}}{3\lambda^2}\right) = K_o \exp\left(-\frac{4\pi^2\phi^2 R_o^{\,2}}{3\lambda^2}\right) \qquad \text{(VII.9)}$$

where I_e is the scattering intensity when the X-ray is subject to the scattering of a single electron, N is the Avogadro constant, n is electron number of the scattering object, ϕ is the scattering angle, λ is the wavelength of the X-ray, and R_o is the radius of

gyration of the dispersion system. For spherical particles, the radius of these particles (r) can be calculated from the following Equation VII.10 [36,40]:

$$R_o = \sqrt{\frac{3}{5}} r \qquad \text{(VII.10)}$$

A good approximation to evaluate r can be obtained by Equation VII.11 [40]:

$$I_{(q)} \infty \exp\left(-\frac{R_o^{\,2}}{3} q^2 \right) \qquad \text{(VII.11)}$$

Figure VII.11 shows a typical Guinier plots, showing good straight lines, as expected from Equation VII.13. From the slope of the straight line, one can calculate R_o.

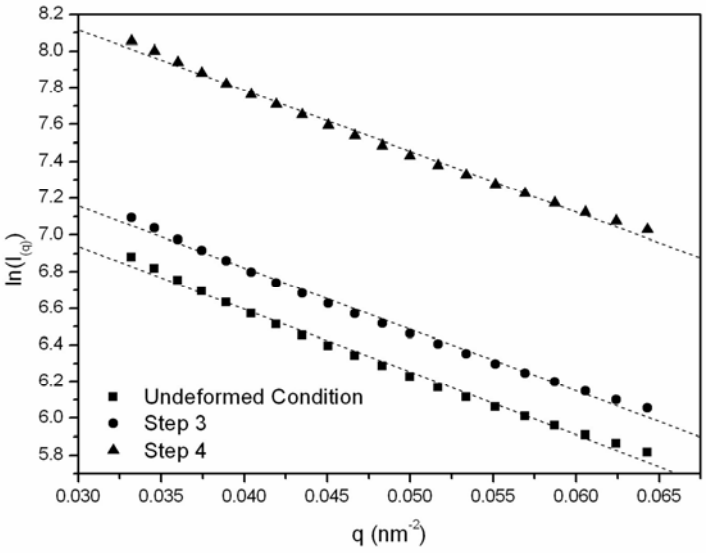

Figure VII.11 – SAXS experimental data and tangents of PU-I experimental curve.

The Q_{inv}, L_{domain}, $L_{Crystal}$ and r values for PU-I, PU-II and PU-III for permanent shape, Step3 and Step 4 are summarized in Table VII.6. Comparing the values of r for PU-I, it is possible to observe that the radius of particles tends slightly to decrease during the shape memory cycle.

Table VII.5 – SAXS experimental data: Qinv, LCrystal, Ldomain, and r.

		$r_{average}$	Q_{inv}	L (nm) Crystalline phase	L (nm) Soft domain
Permanent Shape	PU-I	13.1	8.7	–	–
	PU-II	–	82.8	16.8	13.2
	PU-III	–	334.8	14.0	10.5
Step 3	PU-I	13.0	9.8	–	–
	PU-II	–	–	–	–
	PU-III	–	–	–	–
Step 4	PU-I	12.9	23.6	–	–
	PU-II	–	115.5	14.5	12.6
	PU-III	–	876.0	14.6	13.1

E – Mechanical Properties

Figure VII.12 shows typical stress–strain curves for PU-I, PU-II and PU-III at room temperature and Table VII.6 summarizes the values of the mechanical properties, as well the values of the shape memory properties of them.

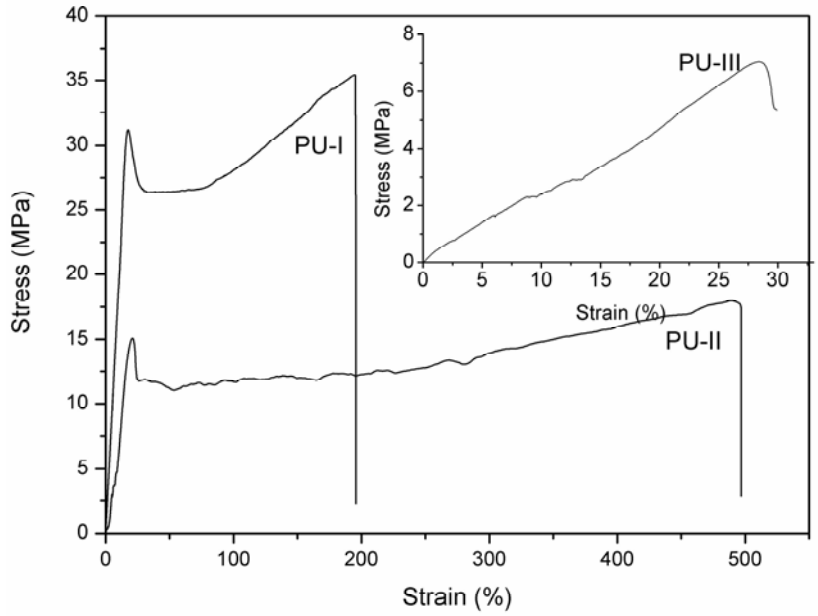

Figure VII.12 – Stress–strain curve of PU-I, PU-II and PU-III.

Table VII.6 – Mechanical and shape memory properties of PU-I, PU-II and PU-III.

PU	σ_m (MPa)	ε_m (%)	E (MPa)	R_f (%)	R_r (%)
I	35	196	7	87	67
II	17	497	3	86	41
III	7	30	2	98	95

PU-I and PU-II showed mechanical behavior typical of ductile polymers with the presence of a clear yielding point. PU-III, however, showed characteristic behavior of brittle polymer: no plastic deformation after de elastic strain.

It is clear that an increase in $W(HS)$ produced an increase in modulus and in stress at yield. These results show that the mechanical properties of PUs are highly dependent on the hard segment content, which agree well with previous reports [24,25,26,41]. Hard segments can bind themselves via hydrogen bonds which results in an enhancement in the stiffness and strength of PUs.

The reversible phase was designed to actuate during the softening of soft domains or the melting of crystallites. However, R_r of PUs is also highly dependent on the hard segment content. Strong interactions among hard segments provide enough energy to restore the polymer back to the original shape. As reported before [43], no clear relationship between $W(HS)$ and R_r were observed for PUs copolymers. In fact, in order to achieve best SM properties, the polymer must have an optimal degree of fixed phase and reversible phase.

In PU-I, the presence of a high degree of H-bonding between hard segments compensates partially its low index of crystallinity to yield materials with R_r close to 67%. This result suggests that hydrogen bonding is an important feature of shape memory polyurethanes for both fixing and restoring shapes.

Even lower values of R_r were displayed by PU-II that have both low values of hydrogen bonding and crystallinity. The presence of PCL530 within soft segments containing also PCL10000 restricts both crystallization of soft segments and also disrupts the structure to reduce hydrogen bonding. These two factors are responsible for reducing the shape memory capacity of this sample (PU-II). On the other hand, a very high value for R_r was displayed by samples containing only PCL10000 as soft segments (PU-III), as a result of the combination of both high degrees of hydrogen bonding and crystallinity.

VII.4 – Conclusions

Shape memory poly(ester-urethane) with varying hard-segment content and degree of phase separation were synthesized. Hard segment content controls thermal, mechanical and morphological properties. SAXS results showed also that the capability to recover shape is related to ability of specific macromolecular architectures to have their nanostructure rebuilt after the shape memory cycle. Shape memory properties were driven by the disperse phase: deformed disperse phase stores the deformed shape and melting of disperse phase recovers the initial shape. For the obtained PUs, hydrogen bonding and the crystal packing influence the disperse phase and therefore, regulate the shape memory properties.

VII.5 – Acknowledgments

The authors acknowledge the financial support from the following institutions: National Council for Scientific and Technological Development (CNPq), a foundation linked to the Ministry of Science and Technology (MCT) of the Brazilian Government; the State of Minas Gerais Research Foundation (FAPEMIG); and the National Synchrotron Light Laboratory (LNLS-Brazil) for the use of the SAXS beamline facilities.

VII.6 – References

1 – Szycher M. Szycher's Handbook of Polyurethanes. London: CRC Press, 1999 (chapter 1.1–1.6).

2 – Oertel, Günter. Polyurethane Handbook. 2nd ed. New. York: Hanser Publisher, 1994 (11–45).

3 – Pan H, Chen D. Eur Polym J 2007;43:3766-72

4 – Chen G, Ma Y, Zheng X, et al. J Polym Sci B 2007;45(6):654–60.

5 – Lendlein A, Langer R. Science 2002;296(5573):1673–6.

6 – Wilson TS, Small W, Benett WJ, et al. Proc SPIE - Int Soc Opt Eng. 60070R-1-8, 2005.

7 – Miaudet P, Derre A, Maugey M, et al. Science 2007;318:1294–6.

8 – Gall K, Dunn ML, Liu YP, Stefanic G, Balzar. Appl Polym Sci 2004, 85(2):290–2.

9 – Gall K, Kreiner P, Turner D, Hulse M. J Micro Sys 2004, 13(3): 472-83

10 – Van Krevelen DW. Properties of polymers. Amsterdam: Elsevier Science, 3rd ed., p. 121, 1990.

11 – Oliveira W, Glasser WG. Macromolecules 1994;27:5–11.

12 – Bao H, Zhang Z, Ying S. Polymer 1996;37(13):2751–4.

13 – Seymour RW, Cooper RL. Macromolecules 1973;6:48–53.

14 – Gunes IS, Jana SC. J Nanosci Nanotechnol 2008;8(4):1616–37.

15 – Gorna K, Gogolewski S. Polym Degrad Stab 2002;75(1):113–22.

16 – Yeganeh H, Lakouraj MM, Jamshidi S. Eur Polym J 2005;41(10):2370–9.

17 – Jiang X, Li JH, Ding MM, et al. Eur Polym J 2007;43(5):1838–46.

18 – Ayres E, Oréfice RL, Yoshida, MI. Eur Polym J 2007;43(8):3510–21.

19 – Coates, J.P. Encyclopedia of Analytical Chemistry, Ed. R.A. Meyers, J. Wiley & Sons, Ltd., Chichester, UK, p. 10815–10837, 2000.

20 – Marcos-Fernández, A, Abraham GA, Valentín JL, San Román J. Polymer, 2006;47(3):785–98.

21 – Chattopadhyay DK, Sreedhar B, Raju KVSN. Polymer 2006;47(11): 3814–25.

22 –Cho JW, Lee SH. Eur Polym J 2004;40(7):1343–8.

23 – Huang SL, Lai JY. Eur Polym J 1997;33(10–12):1563–7.

24 – Liu Y, Pan C. Eur Polym J 1998;34(5-6):621–4.

25 – Nakamae K, Nishino T, Asaoka S, et al. Int J Adhes Adhes 1999;19(5):345–51.

26 – Pompe G, Pohlers A, Pötschke P, Pionteck J. Polymer 1998;39(21):5147–53.

27 – Lin JR, Chen LW. J Appl Polym Sci 1998;69(8):1563–74.

28 – Li YJ, Gao T, Liu J, et al. Macromolecules 1992;25(26):7365–72.

29 – Pretsch T, Jakob I, Werner M. Polym Degrad Stab 2009;94:61–73.

30 – Tien YI, Wei KH. Polymer 2001;42(7):3213–21.

31 – Jia QM, Zheng M, Zhu YC, et al. Eur Polym J 2007;43(1):35–42.

32 – Kim BK, Lee SY, Xu M. Polymer 1996;37(26):5781–93.

33 – Xu J, Shi W, Pang W. Polymer 2006;47(1):457–65.

34 – Charnetskaya AG, Polizos G, Shtompel VI, et al. Eur Polym J 2003;39(11):2167–74.

35 – Wang ZG, Hsiao BS, Fu BX, et al. Polymer 2000;41(5):1791–7.

36 – Wang SH, Zhang Y, Ren WT, et al. Polymer Testing 2005;24(6):766–74.

37 – Jiang ZY, Tang YJ, Men YF, et al. Macromolecules 2007;40(20):7263–9.

38 – Chang SL, Yu TL, Huang CC, Chen WC, Linliu K, Lin TL.. Polymer 1998;39(15):3479–89.

39 – Li YJ, Kang WX, Stoffer JO, et al. Macromolecules 1994;27(2):612–4.

40 – Tang YJ, Jiang ZY, Men YF, et al. Polymer 2007;48(17):5125–32.

41 – Lee BS, Chun BC, Chung YC, et al. Macromolecules 2001;34(18):6431–7.

42 – Yang JH, Chun BC, Chung YC, Cho JH. Polymer 2003;44(11):3251–8.

Chapter VIII (Capítulo VIII)

Study of the morphology exhibited by exfoliated polyurethane/montmorillonite nanocomposites during shape memory cycle

I. M. Pereira[1,2]; R. L. Oréfice[2*]

[1]Coordenação de Metalurgia – Centro Federal de Educação Tecnológica de Minas Gerais – CEFET/MG Campus VII – Timóteo-MG
[2]Departamento de Engenharia Metalúrgica e de Materiais – Universidade Federal de Minas Gerais – UFMG, Belo Horizonte-MG

Abstract:

In this work, exfoliated polyurethane/montmorillonite (MMT) nanocomposites were successfully produced by direct solution blend. The polymer and the exfoliated polymer-layered nanocomposites presented shape memory properties. The structure and thermal properties were investigated using: modulated differential scanning calorimetry (MDSC) and small angle X-ray scattering (SAXS). The morphological changes observed during a low and a high temperature shape-memory cycle were investigated. The filler incorporation disturbs the formation of hydrogen bonds between amine and carbonyl group, interfering with the mobility of polymeric chains and, consequently, with the metastable structure formed during deformation. The recovery of polymer and nanocomposites was observed to be triggered by the melting of the crystallites and by the strong interactions among hard domains.

Keywords: Shape memory, polyurethane, montmorillonite, SAXS, MDSC

VIII.1 – Introduction

Polyurethanes (PUs) are one of the most studied classes of special polymers that comprise a diverse family of polymers. A typical PU may contain, in addition to the urethane linkages, aliphatic and aromatic hydrocarbons, esters, ethers, amides, urea, and isocyanurates groups. They are usually obtained by reacting diisocyanates with diols in the presence of a catalyst. PUs are used in an array of commercial applications: flexible slabs, flexible molded foams, rigid foams, solid elastomers, etc [1]. PUs are famous to have distinct characteristics that can vary depending upon formulation and processing, such as (i) easy preparation method, (ii) high resistance to organic solvents and aqueous solutions, (iii) long-term stability against exposure to sunlight, (iv) consistent elastic properties, (v) biocompatibility, and (vi) biodegradability [2, 3].

The segmented PUs are typically linear even though, chemically-crosslinked PUs exist. In general, segmented PUs have soft and hard segments. The soft segments display high mobility, are usually presented in coiled conformation and are alternated with units of hard segments. The properties of this type of material will, therefore, be strongly associated with the hard and soft segments: content, interaction and degree of phase separation [4, 5]. Recently, montmorillonite / polyurethane nanocomposites have been studied in order to produce materials with improved properties that could extend the use of PU further [6]. To achieve high levels of properties in polymer nanocomposites, the dispersion and exfoliation of layered silicates within polymeric matrices are considered key steps. Since natural montmorillonite has poor affinity with hydrophobic polymers, cationic modified MMT has been widely used to improve interfacial interactions and exfoliation [6]. More recently, approaches have tailored PUs elastomers properties to yield shape memory properties. These are thermo-responsive materials that can store and recover large strains by application of a prescribed thermo-mechanical cycle [7].

In the present study, a shape memory poly(ester-urethane) was synthesized in an aqueous environment. The hard segment was formed by extending aliphatic isophorone diisocyanate with hydrazine. The soft segment was based in poly(caprolactone diol) of

low molecular weight. PUs were reinforced with Na+/MMT. DSC was used to study the morphology features. Additionally, SAXS measurements were carried out to investigate the structural changes during shape memory cycle.

VIII.2 – Materials and Methods

A – Polymer synthesis

Poly(caprolactone diol) (PCL – Mn = 2000 g mol^{-1}), isophorone diisocyanate (IPDI), 2,2-bis(hydroxymethyl), propionic acid (DMPA) and dibutyl tin dilaurate (DBDLT) were obtained from Aldrich (St. Louis, MO). Triethylamine (TEA, 98%) and hydrazine (HZ, 25%) were purchased from Vetec (RJ, Brazil). All these chemicals were employed throughout this work without any previous treatment. PUs were prepared by the prepolymer mixing method, according to a procedure described in previous work [8]. The weight fraction (%) of hard segment, $W(HS)$, is 38% (IPDI + HZ).

PU/MMT nanocomposites were prepared via solution blending. Initially, the MMT water dispersion was produced by mixing the clay (5 wt %) with deionised water for 24hs at 65ºC. The PU water dispersion was blended with the MMT water dispersion at room temperature under mechanical stirring for 15min. The samples with different MMT weight contents were numbered as PU-C, MMT-1, MMT-2, MMT-3, corresponding to MMT weight contents of 0%, 0.1%, 1.0%, and 3.6% respectively.

B – Modulated differential scanning calorimetry (MDSC)

MDSC measurements were performed using a TA Instruments 2920. The following protocol was applied to each sample: (1) heating from room temperature to 110°C at 15°C min^{-1}, (2) holding for 3.00min at 110°C, (3) cooling to –110°C at 3.00°C/min, modulating +/– 1.00°C every 60 seconds, (4) holding for 3.00min at –110°C and (5) heating again to 110°C with 3.00°C/min modulating +/– 1.00°C every 60 seconds. The melting temperature was taken as peak maxima, the glass transition temperature (T_g) was obtained by the analyzing software of the calorimeter.

C – Synchrotron small angle X-ray scattering (SAXS)

SAXS measurements of synchrotron small angle X-ray scattering were performed using the beam line of the National Synchrotron Light Laboratory (LNLS, Campinas, Brazil). After passing through a thin beryllium window, the beam is monochromatized ($\lambda = 1.488$Å) and horizontally focused by a cylindrically bent and asymmetrically cut silicon single crystal. The X-ray scattering intensity, $I_{(q)}$, was experimentally determined as a function of the scattering vector, q, whose modulus is given by Equation VIII.1:

$$q = \frac{4\pi}{\lambda}\sin\theta \qquad \text{(VIII.1)}$$

where λ is the X-ray wavelength and θ being half the scattering angle.

Each SAXS pattern corresponds to a data collection time of 900 s. From the experimental scattering intensity produced by all the studied samples, the parasitic scattering intensity produced by the collimating slits was subtracted. All SAXS patterns were corrected for the non-constant sensitivity of the position sensitive X-ray detector, for the time varying intensity of the direct synchrotron beam and for differences in sample thickness. Because of the normalization procedure, the SAXS intensity was determined for all samples in the same arbitrary units so that they can be directly compared. The sample-detector distance of 551.6 mm was used during the measurements.

D – Shape memory properties (SM)

SM experiments were done at T_{def} (deformation temperature) using a universal testing machine (DL3000, EMIC). The sample length between the clamps was 20mm. A shape recovery cycle consisted of the following steps: (1) Samples DIN60 were deformed to a defined strain at 10 mm/min crosshead speed. (2) While maintaining the strain at L_m, samples were cooled down. (3) Mechanical constraints on the polymers were removed. (4) The samples were subsequently heated to 80^{o}C in an oven, and stayed at this

temperature for 20 min to recover its original shape. This completes one thermo-mechanical cycle leaving a residual strain, Figure VIII.1. Test set-ups are described in Table VIII.1, where T_{def} = deformation temperature.

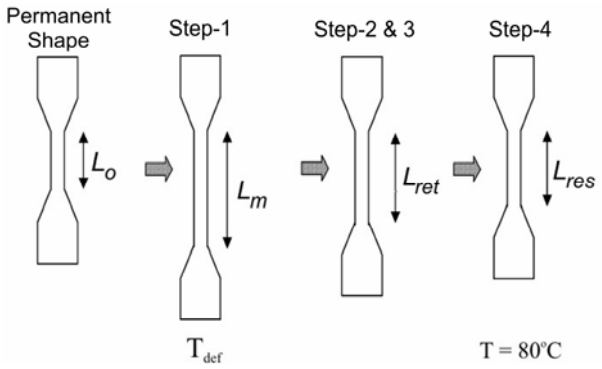

Figure VIII.1 – Shape memory cycle steps

Table VIII.1 – Test set-ups

	T_{def} (°C)	L_m (mm)
PU-C	28	120
MMT-1	28	100
MMT-2	80	32
MMT-3	80	32

The SM properties of the materials were described by the strain recovery ratio, R_R, and the strain fixity ratio, R_f. Both can be determined according to Equation VIII.2 and Equation VIII.3:

$$R_r(\%) = \frac{L_m - L_{Res}}{L_m - L_o} \times 100 \qquad \text{(VIII. 2)}$$

$$R_f(\%) = \frac{L_{Ret} - L_o}{L_m - L_o} \times 100 \qquad \text{(VIII. 3)}$$

where: L_o is the original length, L_m is the deformed length, L_{ret} is retained length and L_{res} is the length after the recover.

VIII.3 – Results and discussion

Segmented polyurethanes generally display several thermal transitions, corresponding to the microstructure of the soft and hard blocks. The soft segments undergo a low temperature glass transition, and, if semicrystalline, a melting transition. The hard segments may display a glass transition and/or multiple melting transitions [9]. The thermal behavior of the obtained PUs is shown in Figure VIII.2. Thermal properties are summarized in Table VIII.2.

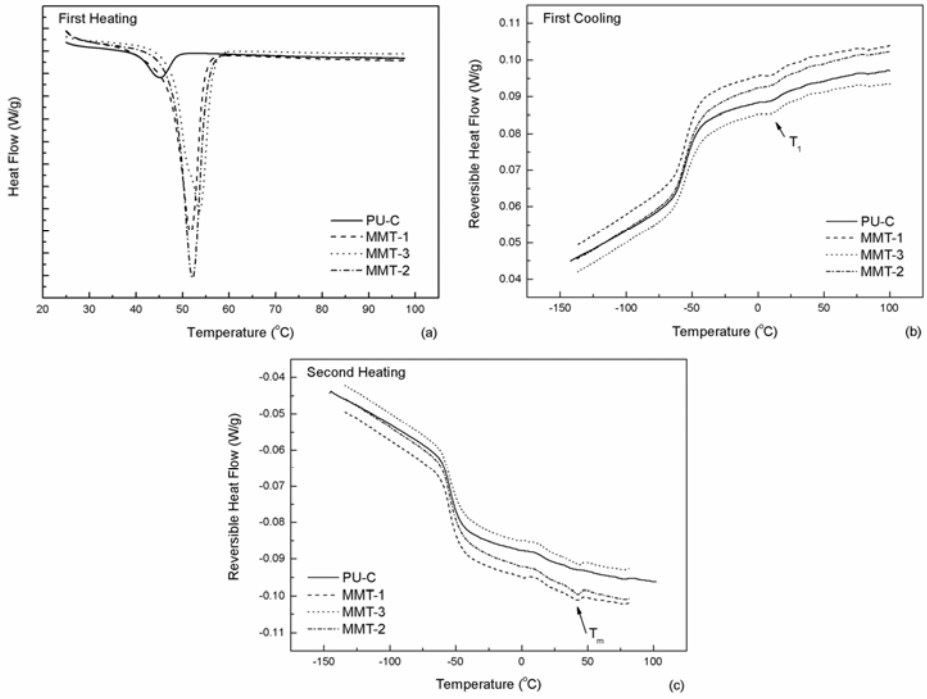

Figure VIII.2 – DSC curves of the obtained PUs: (a) first heating (b) first cooling and (c) second heating.

Table VIII.2 – DSC results of obtained poly(ester urethane).

	T_g (°C)	T_{onset} (°C)	T_{end} (°C)	Zone width	T_1 (°C)	T_m (°C)
PU-C	–54.06	–72.29	–38.49	33.80	16.42	–
MMT-1	–55.27	–67.60	–37.44	30.16	16.38	43.90
MMT-2	–54.29	–69.20	–37.32	31.88	17.49	44.80
MMT-3	–54.50	–66.22	–35.58	30.64	17.00	44.86

According to Seymour and Cooper [10], the endotherm region observed in the DSC may all be ascribed to a morphological effect, and it is a function of hard segment length. Clusters of shorter hard segments give rise to lower temperature endotherm [10,11]. In DSC analysis, the width of transition zone provides a qualitative measure of phase homogeneity, and the variation in the magnitude of T_g can indicate the degree of microphase separation [11]. Nevertheless, the presence of nanoparticles must also be considered in the evaluation of the soft segment homogeneity. It is normally assumed that the incorporation of interacting filler will lead to an increase in the T_g. However, the change of T_g depends on the enthalpic and entropic interactions on the mobility of the soft segment of PU [12]. It appears that the incorporation of the Na+/MMT particles led to an decrease in the T_g, suggesting that the mobility of the amorphous chains were enhanced by the presence of filler. Previous work [13] suggested that the mobility of polymeric chains is altered by increasing amount of intercalation agent because nanoparticles derived from clay can restrict the formation of hydrogen bonds between amine and carbonyl groups. The DSC results may also imply that clay interfered with crystalline formation of soft segment, indicating that the particles can act as nucleating agents for PCL segments within PU which resulted in more perfect crystals with higher meting temperature (T_m).

Figure VIII.3 illustrates SAXS patterns of the obtained PUs during different stages of shape-memory cycle: permanent shape, Step-3 and Step-4. SAXS measures the scattering intensity as a function of the incident X-ray beam. At the initial stage, as expected from the randomly distributed particles embedded in an amorphous matrix, a circular scattering pattern with a homogeneous intensity distribution along the circle was obtained, indicating that the films are isotropic. At Figure VIII.3 during Step-3 of PU-C and MMT-1, it is observed two maxima occurring along the stretching direction on both sides of the beam. The maxima are due to the scattering from the oriented structure formed during deformation process [14], together with crystallization. During Step-4 of the shape memory cycle the PUs patterns recovered the original non-oriented structure.

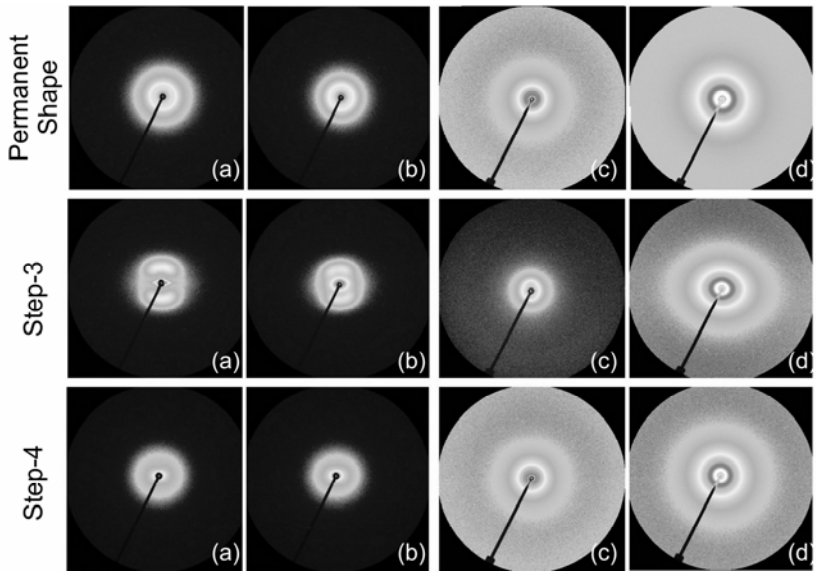

Figure VIII.3 – SAXS pattern during different stages of shape-memory cycle of: (a) PU-C, (b) MMT-1, (c) MMT-2 and (d) MMT-3.

To estimate the overall degree of phase separation, it was employed the Lorentz correction, the invariant quantity, Q_{inv}, which is obtained by integrating $I_{(q)}q^2$ over the range of scattering angles, Equation VIII.4 [15-17].

$$Q_{inv} = \int_0^{\infty} I_{(q)} q^2 dq \qquad \text{(VIII. 4)}$$

Figure VIII.4 illustrates Lorentz corrected SAXS data of the obtained PU during different stages of shape-memory thermomechanical cycle. The scattering peak observed in Figure VIII.4(a) arises due to local heterogeneities in the electron density of the materials and it is usually interpreted as a consequence of the presence of distinct microphases with different electronic densities. Scattering data show that the presence of clay nanoparticles disturbed the phase separation of the system. At low filler content, the scattering peak due to the PU phase separation became narrowed, attesting the gradual increase of the hard–soft segment degree of mixing. At MMT-3 composition, no scattering peak can be observed, demonstrating that a high degree of phase mixture was obtained. SAXS data suggests that a high degree of exfoliation can be achieved. For a exfoliated polymer-layered nanocomposites the number of polymer chains between the layers is almost continuously variable, and the layers stand >10 nm apart [18,19]. It is

also possible to observe that scattering intensity increased due to the presence of clay particles. Having clay particles with higher electronic density than PU matrix, the scattered radiation achieves higher levels when nanoparticles were incorporated into PU.

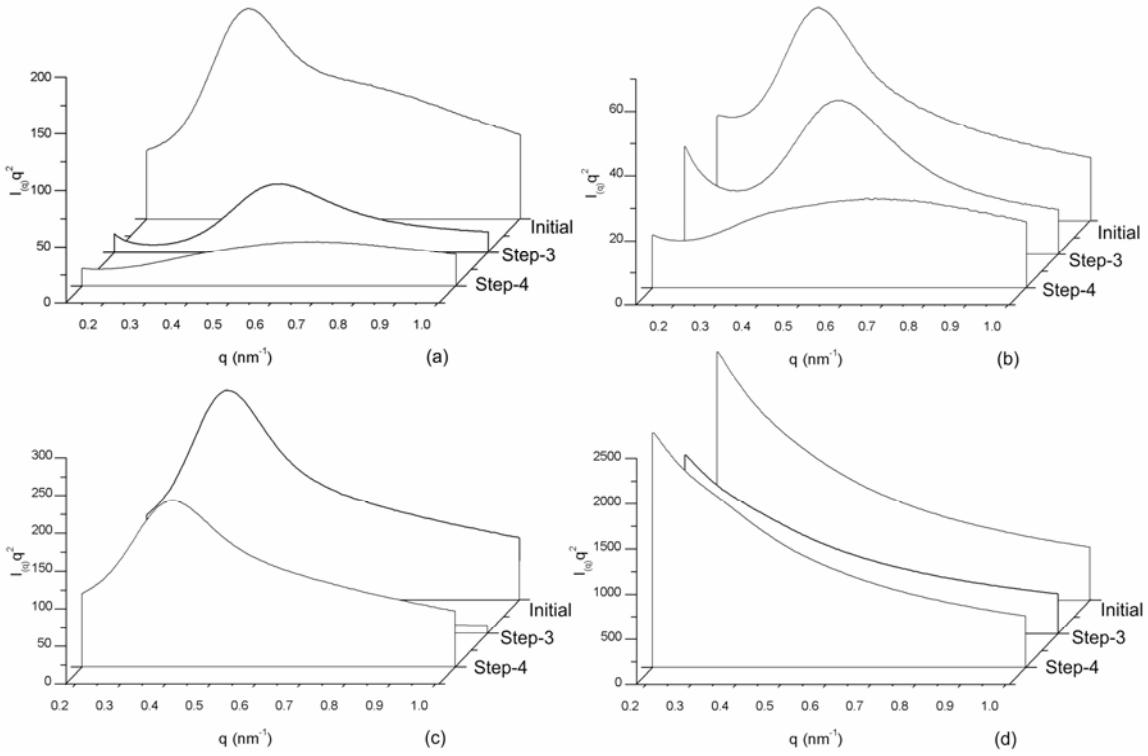

Figure VIII.4 – SAXS curves of obtained PUs: (a) PU-C, (b) MMT-1, (c) MMT-2 and (d) MMT-3

The obtained PUs are a three-phase structure including: amorphous matrix, hard domains and crystals. The nanoparticles introduction adds a fourth phase in the system. The contribution of each phase to the Lorentz corrected SAXS patterns were separated by a deconvolution procedure. Figure VIII.5 illustrates the deconvoluted SAXS of PU-C, MMT-1 and MMT-2. DSC results showed no major differences between the structures of the polymer and the nanocomposites. SAXS profiles of polymer and nanocomposites are also similar, suggesting that the original relative scattering position of amorphous matrix, hard domains and crystals were preserved for the nanocomposites. SAXS experiments of MMT-2 and MMT-3 were performed before

equipment upgrades and the measured scale is smaller than PU-C or MMT-1, what would explain the smaller MMT contribution at Figure VIII.5(c).

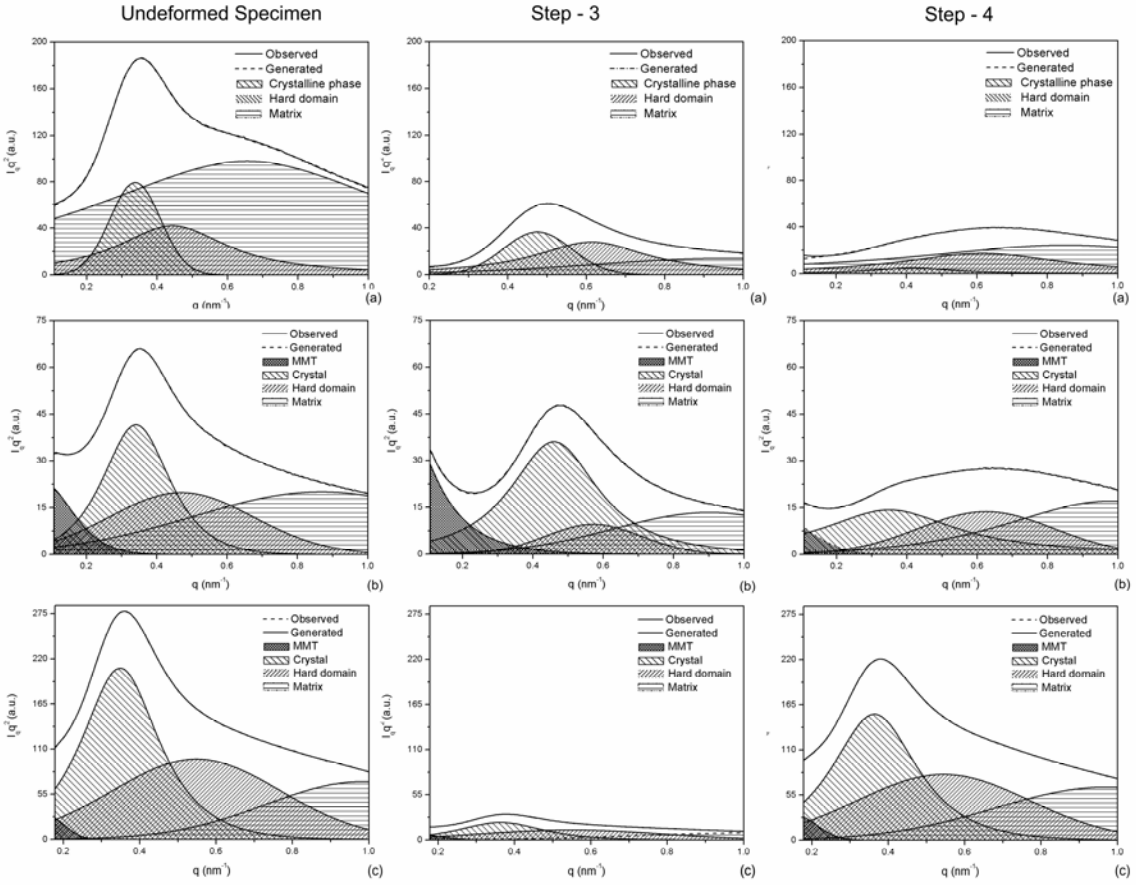

Figure VIII.5 – Deconvoluted Lorentz SAXS pattern of permanent shape , Step-3, and Step-4: (a) PU-C, (b) MMT-1, and (c) MMT-2.

Q_{inv} of each phase was obtained as fraction of the total area. The morphology of the polymer was investigated through the inter-domain repeat distance, L_{domain}, and/or lamellar crystalline repeat distance, $L_{Crystal}$. L is estimated from the $q_{\max}$ corresponding to the maximum of $I_{(q)}q^2$ versus q curves using Bragg's equation, Equation VIII.5 [15-17]. Table VIII.3 summarizes the results.

$$L = \frac{2\pi}{q_{\max}} \qquad \text{(VIII. 5)}$$

Table VIII.3 – Deconvoluted SAXS results.

		Initial		Step-3		Step-4	
		Q_{inv}(%)	L(nm)	Q_{inv}(%)	L(nm)	Q_{inv}(%)	L(nm)
PU-C	crystals	13.53	18.6	30.52	13.2	6.27	15.1
	domains	17.50	14.2	43.82	10.2	35.58	10.2
	matrix	68.96	–	25.65	–	58.15	–
MMT-1	MMT	5.371	89.21	14.752	829.52	2.975	2279.70
	crystals	30.98	18.43	49.47	13.66	32.56	17.95
	domains	29.15	13.38	12.67	10.99	31.35	10.06
	matrix	34.50	–	23.11	–	33.11	–
MMT-2	MMT	0.801	39.23	1.949	52.59	1.316	41.47
	crystals	41.43	18.01	36.73	17.32	38.36	17.27
	domains	39.18	11.46	41.35	11.47	37.36	11.54
	matrix	18.59	–	19.97	–	22.96	–

		Initial	Step-3	Step-4
Disperse phase	PU-C	31.04	74.35	41.85
	MMT-1	65.50	76.89	66.89
	MMT-2	81.41	80.03	77.04
$\frac{\text{Matrix}}{\text{Disperse phase}}$	PU-C	2.22	0.35	1.39
	MMT-1	0.53	0.30	0.50
	MMT-2	0.23	0.25	0.30

The deformation induces crystallization of PU-C and MMT-1. However, due to the high temperature deformation, after Step-3, crystallization is not observed for MMT-2. MMT-3 high degree of phase mixture and high temperature deformation hinders the formation of new crystals. MMT-1 is efficient to recover the original ratio between matrix and disperse phase after Step-4. However, PU-C promotes higher levels of recover after Step-3.

Table VIII.4 summarizes the values for the mechanical and SM properties. The efficiency of a shape memory polymer is controlled by the polymer's chemical structure, molecular weight, degree of cross-linking, and fraction of amorphous and crystalline domains [20].

Table VIII.4 – Shape memory properties of PU-C, MMT-1, MMT-2 and MMT-3

	PU-C	MMT-1	MMT-2	MMT-3
R_f (%)	31.0	39.5	85.5	60.5
R_R (%)	98.2	90.8	72.7	77.9

Although only three points are obtained, Figure VIII.6 suggests that the disperse phase formed during deformation controls R_f(%) and R_R(%). The metastable structure obtained during deformation was employed to maintain the deformed shape in a stable manner thus the disperse phase controls R_f(%). The reversible phase was designed to actuate during the softening of soft domains or the melting of crystallites formed during deformation. However, shape recovery of obtained PUs is also highly dependent on the hydrogen-bonding. After the melting transition, strong interactions among hard segments provide enough energy to restore the polymer back to the original shape. Previous work [13] (Chapter IV) suggested that the hydrogen bonds is restricted by the clay surfaces. Clay nanoparticles may improve R_f(%) because it increase the disperse phase obtained during deformation. However, the metastable phase formed has weaker interactions and reduced ability to recover its original position, therefore, lower R_R(%).

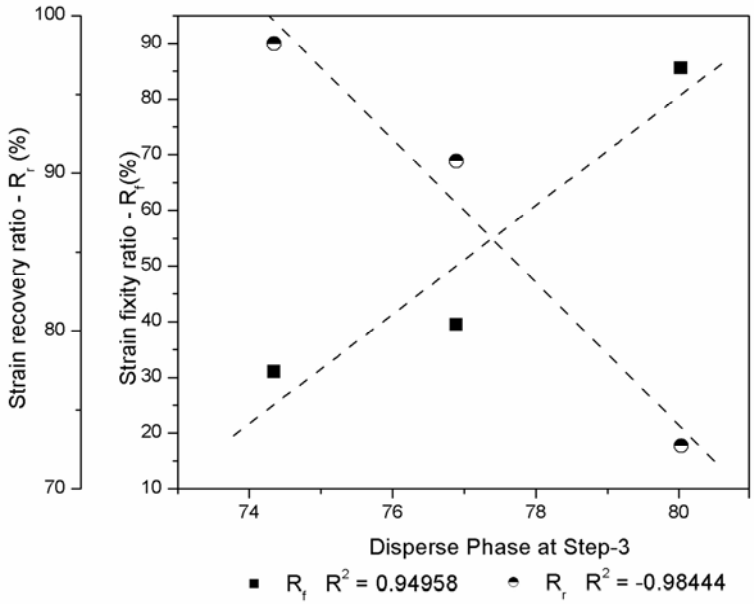

Figure VIII.6 – Step-3 disperse phase influence on shape memory properties

VIII.4 – Conclusions

Exfoliated waterborne PUs nanocomposites were successfully produced by direct solution blend. MMT content modified the matrix morphology shifting the shape memory properties. Data suggests that the incorporation of filler up to 3.6wt% MMT resulted in highly well dispersed and delaminated clay platelets that contributed to an enhancement in the degree of phase mixture of the system. Temporary shape was stored by the metastable structure formed during deformation. Shape recovery was reduced by the presence of nanoparticles.

VIII.5 – Acknowledgments

The authors acknowledge the financial support from the following institutions: National Council for Scientific and Technological Development (CNPq), a foundation linked to the Ministry of Science and Technology (MCT) of the Brazilian Government; the State of Minas Gerais Research Foundation (FAPEMIG); and the National Synchrotron Light Laboratory (LNLS-Brazil) for the use of the SAXS beamline facilities.

VIII.6 – References

1 – Szycher, M. Introduction. Szycher's Handbook of Polyurethanes. London: CRC Press, 1999. p. 1.1-1.6.

2 – Yang JH, Chun BC, Chung YC, Cho JH. Polymer 2003;44(11):3251–8.

3 – Hong JH, Jeon HJ, Yoo JH, et al. Polym Degrad Stab 2007;92(7):1186–92.

4 – Pan H, Chen D. Eur Polym J 2007;43:3766–72

5 – Chen G, Ma Y, Zheng X, et al. J Polym Sci B 2007;45(6):654–60.

6 – Jeong EH, Yang J, Lee HS, Seo WS, Baik DH, Kim J, You JH. Appl Polym Sci 2000;107:803-9.

7 – Lendlein A, Langer R. Science 2002;296(5573):1673–6.

8 – Pereira IM, Patrício PSO, Oréfice RL in: 9º Congresso Brasileiro de Polímeros, Campina Grande, 2007, Vol. 1, 46.

9 – Korley LTJ, Pate BD, Thomas EL, Hammond PT. Polymer 2006;47:3073-82

10 – Seymour RW, Cooper RL. Macromolecules 1973;6:48–53.

11 – Bao H, Zhang Z, Ying S. Polymer 1996;37(13):2751–4.

12 – Kim BH, Choi HJ, Park HS, Jeong YD, Jeong HD, Lee JO, Jo NJ. Compos Interfaces 2006, 13, 285.

13 – Pereira IM, Carvalho S, Pereira MM, Leite MF, Oréfice RL J Appl Polym Sci 2009; Published Online: Jun 2 2009 DOI: 10.1002/app.30404.

14 – Jiang ZY, Tang YJ, Men YF, et al. Macromolecules 2007;40(20):7263–9.

15 – Wang SH, Zhang Y, Ren WT, et al. Polymer Testing 2005;24(6):766–74.

16 – Li YJ, Kang WX, Stoffer JO, et al. Macromolecules 1994;27(2):612–4.

17 – Chang SL, Yu TL, Huang CC, et al. Polymer 1998;39(15):3479–89.

18– Tien YI, Wei KH. Polymer 2001;42:3213.

19 – Wang, JC, Chen YH, Wang JL. J Appl Polym Sci 2006;99:3578.

20 – Miaudet P, Derre A, Maugey M, et al. Science 2007;318:1294–6.

Table VIII.1 – Test set-ups 132
Table VIII.2 – DSC results of obtained poly(ester urethane). 133
Table VIII.3 – Deconvoluted SAXS results. 138
Table VIII.4 – Shape memory properties of PU-C, MMT-1, MMT-2 and MMT-3 139

Figure VIII.1 – Shape memory cycle steps..... 132
Figure VIII.2 – DSC curves of the obtained PUs: (a) first heating (b) first cooling and (c) second heating. 133
Figure VIII.3 – SAXS pattern during different stages of shape-memory cycle of: (a) PU-C, (b) MMT-1, (c) MMT-2 and (d) MMT-3..... 135
Figure VIII.4 – SAXS curves of obtained PUs: (a) PU-C, (b) MMT-1, (c) MMT-2 and (d) MMT-3..... 136
Figure VIII.5 – Deconvoluted Lorentz SAXS pattern of permanent shape , Step-3, and Step-4: (a) PU-C, (b) MMT-1, and (c) MMT-2..... 137
Figure VIII.6 – Step-3 disperse phase influence on shape memory properties 139

VIII – Study of the morphology exhibited by exfoliated polyurethane / montmorillonite nanocomposites during shape memory cycle 129
VIII.1 – Introduction..... 129
VIII.2 – Materials and Methods..... 130
A – Polymer synthesis 130
B – Modulated differential scanning calorimetry (MDSC)..... 130
C – Synchrotron small angle X-ray scattering (SAXS)..... 131
D – Shape memory properties (SM)..... 131
VIII.3 – Results and discussion 133
VIII.4 – Conclusions..... 140
VIII.5 – Acknowledgments 140
VIII.6 – References..... 140

Chapter IX (Capítulo IX)
Shape-memory anchoring system for bladder sensors

I. M. Pereira[a,b,c]; F. Axisa[c]; R. L. Oréfice[b]; J. Vanfleteren[c]; H. P. Neves[d]

[a]Federal Center of Technological Education of Minas Gerais, Timoteo, Brazil
[b]Federal University of Minas Gerais, Department of Metallurgical and Materials Engineering, Belo Horizonte, Brazil
[c]IMEC-INTEC/TFC, Technology Park, Building 914-AB-9052 Zwijnaarde, Belgium
[d]IMEC, Kapeldreef 75, B-3001 Leuven, Belgium

Abstract:

In the present work, we propose the use of shape-memory polymer as anchoring system for the bladder sensor. The anchoring system was designed from a biomedical biodegradable waterborne poly(ester-urethane) produced in an aqueous environment by employing isophorone diisocyanate/hydrazine (hard segment) and poly(caprolactone diol)/2,2-bis (hydroxymethyl) propionic acid (soft segment) as the main reagents. The tensile strength and the elongation-at-break deterioration upon degradation in synthetic urine were investigated. The shape recovery in body was simulated and measured in synthetic urine. Results indicated that the shape recovery can occur at body temperature and sensor expulsing by the body together with the urine may occur by the combined effect of urine hydrolytic attack and compression exerted by the bladder walls.

Keywords: Shape-memory, bladder sensor, biodegradable waterborne

IX.1 – Introduction

The clinical utility of monitoring physical and chemical parameters in the body has motivated great effort to developed sensor for biomedical use. Moreover, nowadays, a convergence of factors is resulting in the rapid development of the field, for instance: (i) advances in silicon microprocessor technology, (ii) advances in biomaterial, and (iii) advent of minimally invasive surgery [1]. Benefiting from these a new generation of electronic devices fabricated on lightweight, bendable miniaturized substrates are widely believed to have great potential for applications in developing new in vivo tools for continuous monitoring indicators of health [1]. These devices can be inserted in the body through natural body openings or small artificial incisions and should be functional and stable during the length of time for which monitoring is required. The noninvasive sensors have a huge potential for disease prevention in medicine and for diagnosis [2] and are being recently investigated to be implemented as a pressure sensor in bladders.

Sensing pressure in bladders is an important topic among many uro-researches. Bladder diseases can be prevented or predicted by observing the abnormal syndromes of the bladder urine pressure variations. Therefore, periodic evaluation of these patients to discover their urodynamic situations and to help these uro-ataxic to urinate normally has been recognized as one of the most important research topics in clinical medical investigations [3]. Furthermore, sensor miniaturization has enabled the pressure sensor implantation through catheters into the bladder with minimal pain and stress for the patient. However, as the sensor become smaller more difficult become to maintain the sensor implanted and to control its tendency to be expelled together with the urine.

In the present work, we propose the use of shape-memory polymer as anchoring system for the bladder sensor. Shape memory polymers (SMP) are thermo-responsive functional material which posses the ability to memorize a permanent shape that can substantially differ from their initial temporary shape [5,6]. Designed from a biomedical biodegradable waterborne poly(ester-urethane) (PU), the device could be introduced into the bladder in a compressed temporary shape through a minimally invasive surgery.

Once implanted into the bladder, at body temperature, the polymer expands to its permanent shape. The expanded larger volume restrains the sensors expulsion and stabilizes the sensor, anchoring it in the urinary bladder. Moreover, being biocompatible, minimal foreign body reaction is expected and being designed to undergo hydrolytic degradation, the sensor would be eliminated by the body after an appropriate time elapse which would eliminate the necessity of a second surgical procedure.

IX.2 – Materials and Methods

A – Sensor Design

Sensors may be built stretchable over a polyimide (PI) film and encapsulated in silicone. Besides being biocompatible, the silicone encapsulation protects the sensor against the urine chemical attack. The encapsulated sensor (pill) is then inserted in the body. The pill shape and small size facilitate the implantation; however, it may also ease the pill ejection by the body. In the present work, the electronic system was simulated by a PI film containing cooper patterning. Figure IX.1 shows the simulated sensor production scheme.

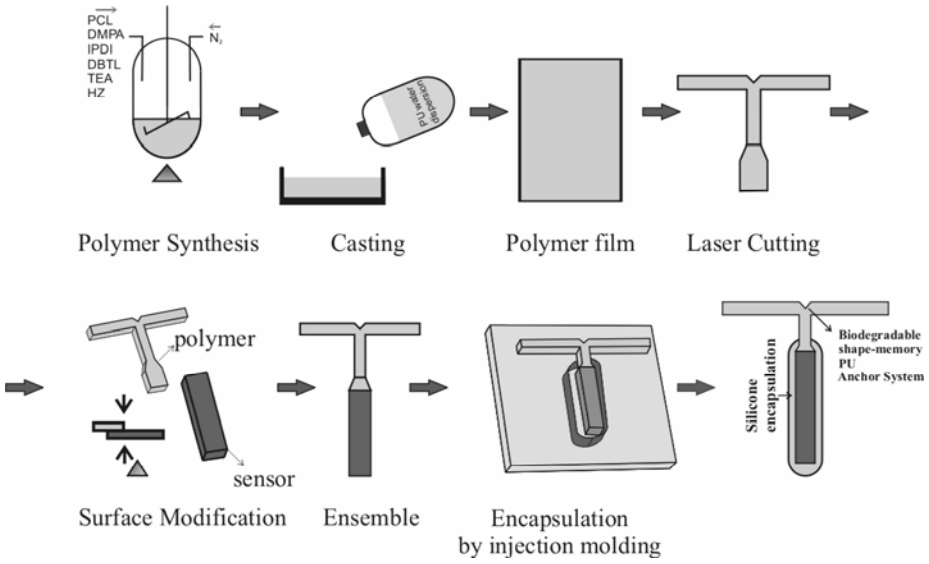

Figure IX.1 – Sensor production scheme

Initially the waterborne PU was produced, and casted in molds. The obtained PU film is cut in the appropriated shape. To guarantee a strong interface between PU and PI films, the PU area that interfaces the PI film was subjected to surface modification and attached to the PI film, i.e., the area was wiped with acetone and attached to the PI film by pressure and temperature, 80^{o}C. Finally, the adherence between the ensemble and the silicone is enhanced by adherence promoter. Afterwards, the system was encapsulated in silicone by injection molding.

B – Polymer synthesis

Poly(caprolactone diol) (PCL1250 – M_n = 1250 g mol^{-1} and PCL2000 – M_n = 2000 g mol^{-1}), isophorone diisocyanate (IPDI), 2,2-bis(hydroxymethyl) propionic acid (DMPA) and dibutyl tin dilaurate (DBDLT) were obtained from Aldrich. Triethylamine (TEA, 98%) and hydrazine (HZ, 25%) were purchased from Vetec. All these chemicals were employed throughout this work without any previous treatment.

PUs were synthesized by the conventional prepolymer method, using a 250 mL three neck glass flask equipped with a heating mantel, a mechanical stirrer, a thermometer under nitrogen atmosphere. In the first step, prepolymer was obtained by reacting PCL1250 (23.7 wt %), PCL2000 (37.9 wt %), DMPA (3.8 wt %) and IPDI (29.6 wt %) at 2 NCO/OH ratio for about 3.5h. During this time, DBDLT was added twice. The reaction was carried out at 70–75ºC. After cooling down to 40ºC, the carboxylic acid groups were neutralized by the addition of TEA (2.9 wt %). The mixture was then gentle stirred for 40 min. The dispersion in water and PU chain extension were achieved by adding HZ (2.1 wt %) and deionized water to the neutralized prepolymer under high-speed stirring. To ensure that the reaction was completed, the mixture was stirred for 60 min. This chemical procedure was well succeeded in producing PUs water dispersions with solid content about 30%. The weight fraction (%) of hard segment, $W(HS)$, is 32.6% (IPDI + HZ).

To produce a film from the waterborne polymeric dispersions, the water dispersion was casted in an open mold and allowed to dry. The films were then annealed at 80^{o}C for 72 h.

C – Laser machine

Figure IX.2 shows the anchor system draft; the shape is obtained by laser cutting. A custom-built laser set-up, integrating a CO_2 laser (GSIL Impact SSM 2150) was used to cut the PU films. The laser operated with pulse energy of 17.8 J/cm^2, pulse repetition rate of 100 Hz and spot size of 5.4 x10^{-4} cm^2. The sample was mounted on the fixed working table and the machining process was completed by the movement of the projection lens at 1 mm/s. The velocity and the laser displacement were controlled by computer program.

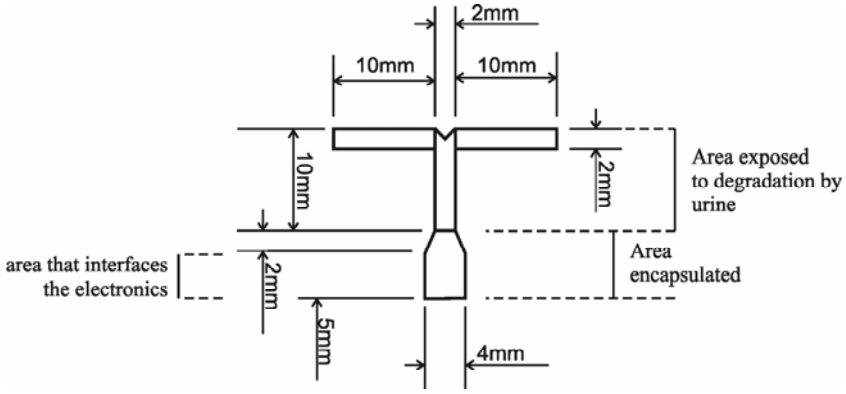

Figure IX.2 – Anchor system draft (thickness = 0.4mm)

D – Infrared spectroscopy

Infrared spectra were collected in a Fourier transform infrared spectrophotometer (FTIR; Perkin–Elmer, model Spectrum 1000). Measurements were carried out using the attenuated total reflectance (ATR) technique. Each spectrum was a result of 64 scans with a resolution of 4 cm^{-1}.

E – Mechanical Tests

The tensile strength (σ_m) and elongation at break (ε_m) of PU samples, Figure IX.3(a) were measured using a universal testing machine (INSTRON 5543) at 10 mm/min crosshead speed. The sample length between the clamps was 30 mm. The tests were performed at room temperature. The average of three samples was obtained.

To evaluate the adhesion of the PU and PI film, 180^o peel tests were performed. Peel specimens consisted of strips with dimension of 10 mm X 5 mm X 0.4 mm that were bonded over 5 mm. The bonded specimens were placed in an INSTRON 5543 tensile testing machine with the PU portion in the upper clamp and PI film in the lower one. An angle of 180^o for peeling was achieved with the specimen in the position described at Figure IX.3(b). The PU film was then peeled from the PI one by the separation of the two clamps with a crosshead speed of 2 mm/min. The bond strength was obtained by Equation IX.1:

$$Bond\ Strength = \frac{F}{A} \tag{IX.1}$$

were F is the maximum force applied and A is the cross-sectional area of the e bonded specimen. The average of three tests was obtained.

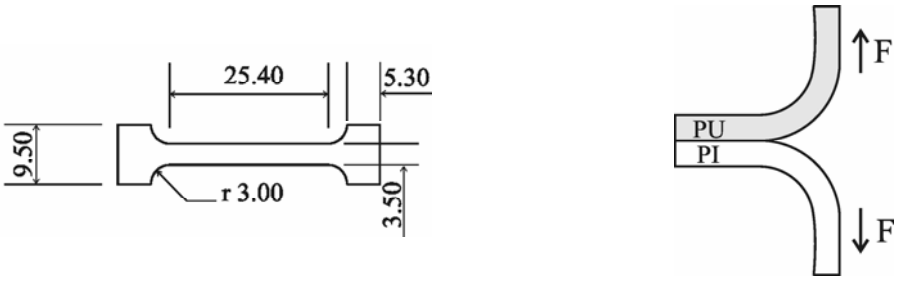

(a) (b)

Figure IX.3 – (a) Tensile specimen (sample thickness 0.4 mm) and (b) Peel specimen

To estimate the adhesion of the ensemble on silicone, two pills were submitted to tension test. The pills were placed in an INSTRON 5543 tensile testing machine with the PU portion in the upper clamp and silicone in the lower one. The clamps were pulled apart with a crosshead speed of 0.5 mm/min. The average of three tests was obtained.

F – Shape memory properties (SM)

Shape memory experiments were done using an INSTRON 5543 tensile testing machine. Six strips with dimension of 28 mm X 3.5 mm X 0.4 mm were tested. The

sample length between the clamps was 20 mm the crosshead speed was at 10 mm/min. The shape recovery cycle consisted of the following steps: (1) Samples were deformed to 55 mm at room temperature. (2) The samples were removed from the clamps and immediately stored in a refrigerated at –20°C. (3) The frozen sample was divided in two pieces. (4) The divided samples were subsequently immersed in different medium at 37°C for 15 min to recover its original shape. The first sample was immersed in artificial urine (SURINE®), and the second one in demonized – DI water. Figure IX.4 illustrates a SM thermomechanical cycle test.

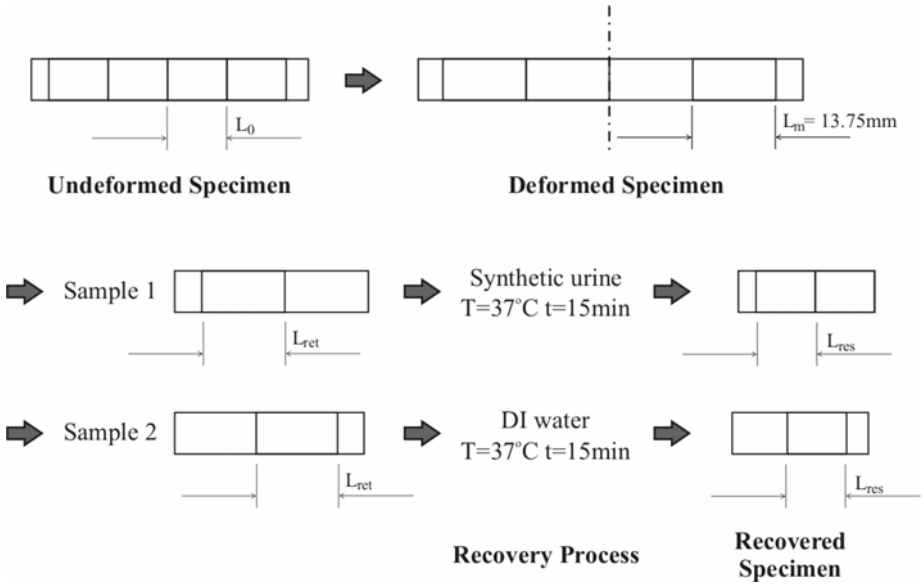

Figure IX.4 – Shape memory thermomechanical cycle

The SM properties of the materials were described by the strain recovery ratio, R_R, and the strain fixity ratio, R_f. Both can be determined according to Equation IX.2 and Equation IX.3:

$$R_r(\%) = \frac{L_m - L_{Res}}{L_m - L_o} \times 100 \quad \text{(IX.2)}$$

$$R_f(\%) = \frac{L_{Ret} - L_o}{L_m - L_o} \times 100 \quad \text{(IX.3)}$$

where: L_o is the original length, L_m is the deformed length, L_{ret} is retained length and L_{res} is the length after the recover.

G – Shape Recovery Body Simulation

To simulate the shape recovery of implanted pills, two pills were subjected to a shape-memory thermomechanical cycle. Initially, the arms were stretched, folded and stored at –20°C. The recovery was simulated at 37°C, immersing the deformed pills in artificial urine (SURINE®). Figure IX.5 illustrated the shape memory cycle.

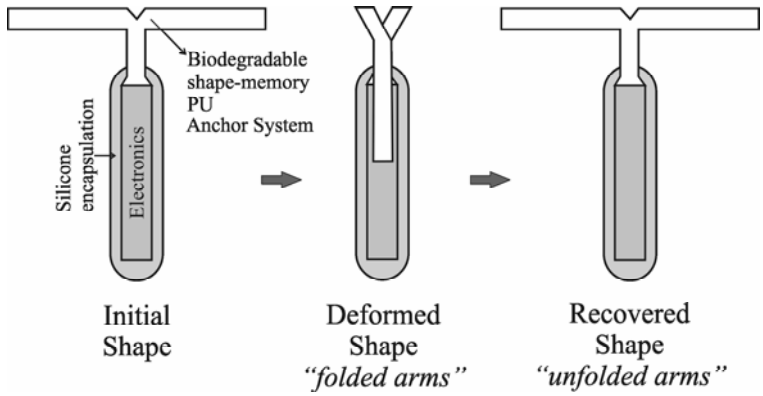

Figure IX.5 – Shape memory recovery in vivo simulation.

H – Hydrolytic degradation tests

The hydrolytic degradation was investigated by immersing specimens, Figure IX.3(a) in synthetic urine (SURINE®) at 37°C. The samples were removed from the media at: 1 day, 7 days, 16 days and 25 days. The mechanical properties of the wet samples, σ_m and ε_m, were measured using a universal testing machine (INSTRON 5543). Before the experiments, the specimens were gentled wiped the sample length between the clamps were 30 mm and the crosshead speed was 10 mm/min. Tests were performed at room temperature. The average of two samples was obtained. σ_m and ε_m were calculated as fraction of the not degraded sample, Equation IX.4.

$$\Delta P_t(\%) = \left(\frac{P_t - P_o}{P_o} \times 100 \right) \tag{IX.4}$$

where P represent the measured mechanical property σ_m or ε_m and the index o and and t are, respectively, the initial value and the property measured at time t.

After the mechanical tests, the specimens were dried to a constant weight at 37°C for 1 week and weighed using an analytical balance to determine the weight loss. The weight loss of the PU films after degradation was evaluated as the residual weight (%), which was defined by the Equation IX.5.

$$Residual\ \ Weight\,(\%) = 100 - \left(\frac{w_0 - w_t}{w_0} \times 100 \right) \qquad \text{(IX.5)}$$

where w_o and w_t were the initial weight and the weight at time t, respectively.

IX.3 – Results and Discussion

The characteristic absorption bands of poly(ester-urethanes) are assigned in Figure IX.6. The primary amine stretching modes appear at 3600 – 3150 cm^{-1}. The carbonyl group stretching vibrations, C=O, appear at 1760 – 1600 cm^{-1}. The secondary amide absorption, >N–H, appears at 1640 – 1540 cm^{-1}. The band at 1150 cm^{-1} is assigned to the stretching of the –C–O–C– group [7, 8, 9, 10].

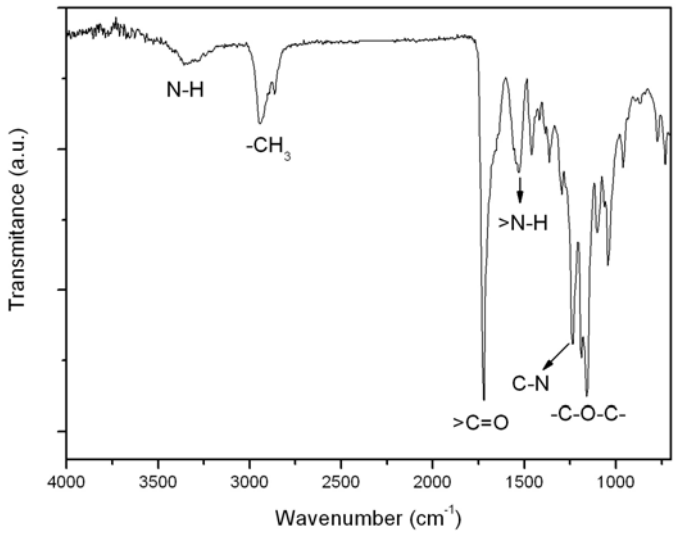

Figure IX.6 – FTIR spectra of obtained PU

Figure IX.7 shows pictures of: (a) PU film, (b) ensemble, (c) pill after silicone encapsulation by injection molding and (d) simulated sensor. To produce a film from

waterborne polymeric dispersions, the water dispersion is casted in an open mold and allowed to dry. After the application on a mold, the water evaporates quickly from the system. The polymer particles moves and stabilize the molecule. Eventually, hydrogen bonding is formed between the molecules. As the dispersion water content is high, frequently shrinkage defects, i.e. depression in surface or internal void, emerge during the film formation. As the problem occurs in the region that dries last, the mold was designed with thickness variation so the region of interest dries first, Figure IX.7(a), without any shrinkage defect. The thicker region of the mold contains more dispersion volume thereby; it needs longer time to dry; this region also works as a reservoir supplying the surrounding regions with liquid.

The molding defects during the silicone encapsulation were avoided through controlling the mold surface roughness. It was also necessary to design a mold with two cavities; one was used to inject the silicone into the mold and the other one was used to release the air from the mold and the bobbles trapped into the injected silicone, Figure IX.7(c). After encapsulation, excess molding material may penetrate into mold gaps. These flash are removed to assure the final surface quality of the pills, Figure IX.7(d).

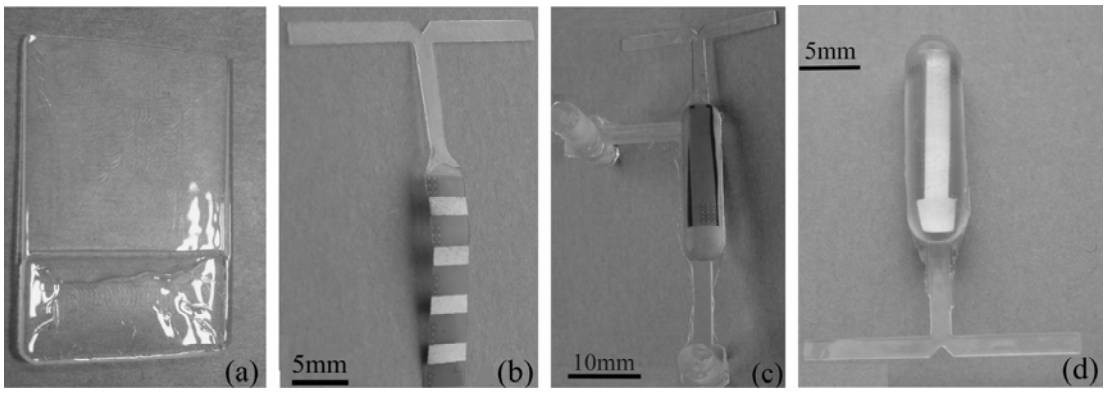

Figure IX.7 – Pictures from the sensor manufacturing process: (a) PU film, (b) ensemble, (c) the pill after encapsulation by injection molding and (d) the simulated sensor.

The typical mechanical properties of the films are illustrated in Figure IX.8. PU are characterized by high ductility and good mechanical properties σ_m = 19.0 ± 1.9 MPa and ε_m = 691 ± 9.6 %. High adherence forces were observed between PU and PI film.

The bond strength observed between the two films was 26.1 ± 5.3 KPa. The tear of PI film was observed as fracture mode for some specimens what might indicate that higher average bond strength could be observed were the PI film thicker. Although adherence forces between PU and silicone are reported poor, the pill tension tests showed good maximum load 7.6 ± 2.7 N; however, the test may have measured the adherence between the PI and silicone rather the adherence between the PU and silicone.

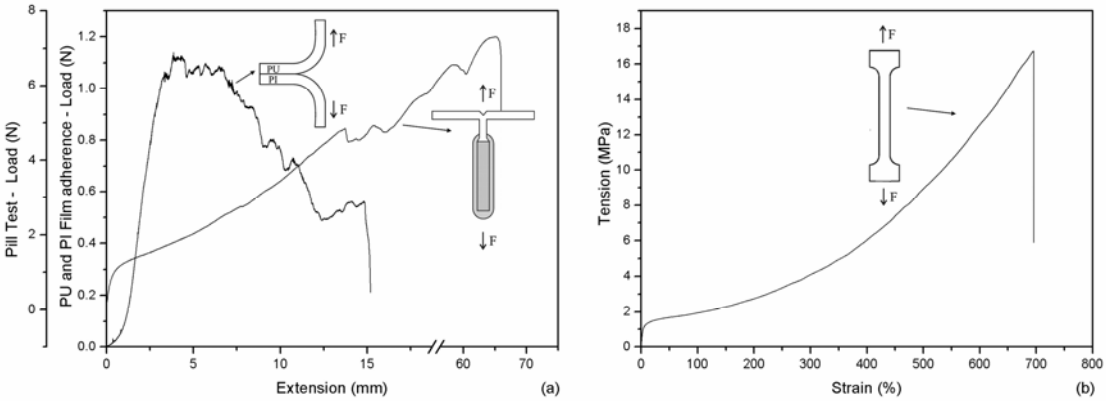

Figure IX.8 – Mechanical test and peel test of obtained specimens.

The R_R in synthetic urine and DI water are slight different, respectively 92.7 ± 1.6% and 95.2 ± 2.3%. The difference may be caused by the ions or by the SURINE® pH which may hinder the polymer chain movement, restricting the shape recover. During the shape memory experiments, upon removing the clamps at Step-2 a significant recover of strain occurs and thus low values of R_f are observed, 68.3 ± 12.0%. According to Ping et al [6], when the deformation temperature is too low (30°C below the melting temperature of the soft segment), the shape recovery starts at a lower temperature and takes place over a wide temperature range. In the present study, this feature guarantees the recover at low temperature as the body temperature. However, higher R_f could be obtained if the metastable structure, developed during the strain were frozen before the mechanical clamps were removed.

Figure IX.9 shows the pictures of the shape recovery body simulation. Figure IX.9(a) shows the pill before deformation, Figure IX.9(b) shows the stretched arms and Figure

IX.9(c) shows the folded in the refrigerator. The restored shape is observed in Figure IX.9(d). As recover starts at low temperature, it is important handle with appropriated tools because the hand temperature may initiate the recover process.

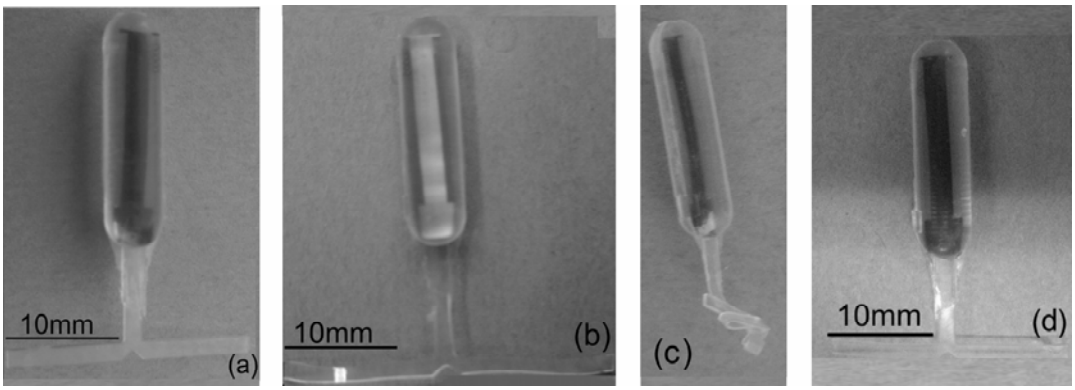

Figure IX.9 – Shape recovery body simulation pictures.

Previous works, chapter III, showed hydrolytic degradation process is characterized by the hydrolytic attack on the soft segment ester increasing the crystallinity of the soft segments. The chemicrystallization process [11] is accompanied by the progressive reduction of the fraction of carbonyl group hydrogen-bonded.

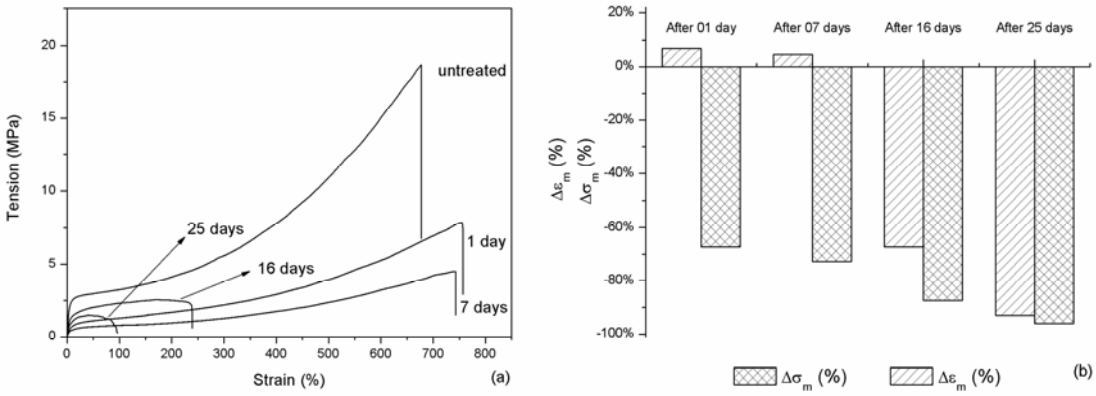

Figure IX.10 – (a) Stress-strain curve of untreated specimen and degraded samples; (b) mechanical properties comparasion.

The tensile properties of plastics, above all the tensile strength and elongation-at-break, are sensitive to material degradation [11]. Stress-strain curves of untreated specimen and hydrolytic degraded ones are given in Figure IX.10(a). The mechanical property,

σ_m and ε_m, of degraded samples were compared to the mechanical properties of untreated specimens. The results are summarized in Figure IX.10(b).

The hydrolytic attack is associated in first place with the reduction in tensile strength and later with a strong reduction in elongation-at-break until a total embrittlement of the specimens occurs. Mechanical test indicate that the sensor expulsion by the body may occur due to the erosion of highly degraded material. The combined effect of hydrolytic attack by the urine and the compression cycles exerted by the bladder walls can promote the anchoring system disintegration. The pieces together with the sensor will be expelled by the body after together with the urine. As observed in Figure IX.11, the weight loss after 25 days of degradation process is small, thus the combined effects are more important than weight loss alone.

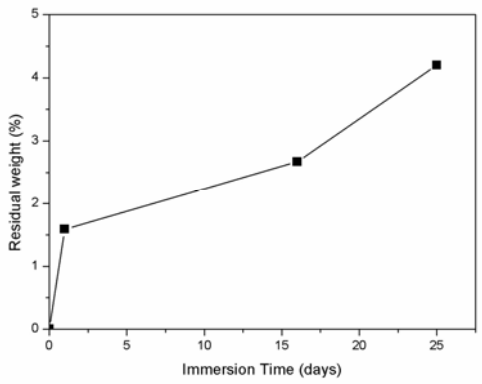

Figure IX.11 – Mass changes of polyurethanes upon degradation.

After 25days, embrittlement does not allow the determination of the material's mechanical properties. Complete degradation is observed after 48 hs of hydrolytic attack in synthetic urine at 80^{o}C.

IX.4 – Conclusion

Biodegradable shape memory polymer is efficient to create an anchoring system for miniaturized bladder sensor. The sensor can be implanted during a minimal invasive surgery and, after an appropriated time elapse, the urine hydrolytic attack and the bladder wall compression cycles can promote the system disintegration the pieces and

sensor would be eliminated together with the urine without a second surgical procedure. Shape recovery in synthetic urine medium was observed at body temperature.

IX.5 – Acknowledgements

The authors acknowledge the financial support from the following institutions: National Council for Scientific and Technological Development (CNPq) and the State of Minas Gerais Research Foundation (FAPEMIG).

IX.6 – References

1 – Ratner BD, Hoffmann AS, Schoen FJ, Lemons JE. Biomaterials science: an introduction to biomaterials in medicine, 2nd ed. Elsevier; 2004.

2 – Axisa F., Schmitt PM, Gehin C, et al. IEEE Transactions, vol. 9, no. 3, 2005.

3 – Wang CC, Huang CC, Liou JS, et al. IEEE 2007.

4 – Lendlein A, Kelch S. Angew. Chem. Int. Ed. 2002, 41:2034.

5 – Lendlein A, Langer R. Science 2002;296(5573):1673.

6 – Ping P, Wang W, Chen X , and Xiabin Jing et al. Biomacromolecules, 2005,6:587.

7 – Chattopadhyay, D. K.; Sreedhar, B.; Raju, K. V. S. N. Polymer 2006,47:3814.

8 – Bao, H.; Zhang, Z.; Ying, S. Polymer 1996,37:2751.

9 – Ayres, E., Oréfice, R. L., Yoshida, M. I. Eur Polym J 2007,43:3510.

10 – Gorna, K.; Gogolewski, S. Polym Degrad Stab 2002,75:113.

11 – Pretsch T, Jakob I, Müller W. Polym Degrad Stab 2009,94:61.

X – Conclusões Finais

Durante o presente trabalho, em um ambiente aquoso, foram produzidas poliuretanas baseadas em policaprolactona diol e isoforona diisocianato. Ademais, foram obtidos nanocompósitos poliuretana/montmorilonita com diferentes concentrações de argila. As poliuretanas e os nanocompósitos obtidos são hidrolisáveis e apresentam o efeito memória de forma. A taxa de hidrólise pode ser acelerada quando condições alcalinas são utilizadas; e manipulada pela concentração de segmento macio e/ou pela concentração de nanopartículas.

As poliuretanas segmentadas obtidas são basicamente copolímeros em bloco que apresentam segmentos macios e rígidos. Os segmentos são termodinamicamente incompatíveis e parcialmente miscíveis. Devido à incompatibilidade das fases uma estrutura de três fases é gerada: uma fase dispersa formada por cristalitos e domínios rígidos embutidos em uma matriz amorfa. A mistura de fases e as interações de hidrogênio foram controladas pela concentração de segmento rígido, pela massa molar do segmento macio e pela concentração de nanopartículas. Consequentemente, a morfologia da matriz e da fase dispersa foi governada por esses fatores.

As propriedades de memória de forma foram atribuídas à movimentação das cadeias do segmento macio e dirigidas pela fase dispersa. A re-organização da fase dispersa durante a deformação imobiliza a forma temporária. A fusão da fase dispersa da espécie deformada recupera a forma inicial. As interações de hidrogênio e a mistura de fases influenciam a fase dispersa e, portanto, regulam as propriedades de memória de forma. Como a concentração de nanopartículas modificada a morfologia da fase dispersa, as propriedades de memória de forma são alteradas pela presença da argila.

Experimentos “in situ” mostraram que os cristais da fase macia fundem durante a fase de recuperação da forma original, enriquecendo a matriz com segmentos macios. Como conseqüência, a incompatibilidade no bulk aumenta gerando um novo ponto de equilíbrio termodinâmico que define uma nova nanoestrutura. Por isso, a capacidade de recuperar a forma original está relacionada com a facilidade da arquitetura

macromolecular ter sua nanomorfologia reconstruída após ciclo de memória de forma. Assim, o alto grau de miscibilidade das fases produz resultados de memória de forma inferiores porque a mistura de fases impede a movimentação da cadeia polimérica e restringem a reconstrução da nanomorfologia.

Segundo testes “in vitro”, as poliuretanas e os nanocompósitos obtidos podem ser considerados biomateriais adequados para participar nos procedimentos relacionados com a engenharia de tecidos.

Livros Grátis

(http://www.livrosgratis.com.br)

Milhares de Livros para Download:

Baixar livros de Administração
Baixar livros de Agronomia
Baixar livros de Arquitetura
Baixar livros de Artes
Baixar livros de Astronomia
Baixar livros de Biologia Geral
Baixar livros de Ciência da Computação
Baixar livros de Ciência da Informação
Baixar livros de Ciência Política
Baixar livros de Ciências da Saúde
Baixar livros de Comunicação
Baixar livros do Conselho Nacional de Educação - CNE
Baixar livros de Defesa civil
Baixar livros de Direito
Baixar livros de Direitos humanos
Baixar livros de Economia
Baixar livros de Economia Doméstica
Baixar livros de Educação
Baixar livros de Educação - Trânsito
Baixar livros de Educação Física
Baixar livros de Engenharia Aeroespacial
Baixar livros de Farmácia
Baixar livros de Filosofia
Baixar livros de Física
Baixar livros de Geociências
Baixar livros de Geografia
Baixar livros de História
Baixar livros de Línguas

Baixar livros de Literatura
Baixar livros de Literatura de Cordel
Baixar livros de Literatura Infantil
Baixar livros de Matemática
Baixar livros de Medicina
Baixar livros de Medicina Veterinária
Baixar livros de Meio Ambiente
Baixar livros de Meteorologia
Baixar Monografias e TCC
Baixar livros Multidisciplinar
Baixar livros de Música
Baixar livros de Psicologia
Baixar livros de Química
Baixar livros de Saúde Coletiva
Baixar livros de Serviço Social
Baixar livros de Sociologia
Baixar livros de Teologia
Baixar livros de Trabalho
Baixar livros de Turismo